The Impact of Extra Mixing in Low-Mass Stars on Explaining the Isotopic Compositions of Presolar Grains

by

Maeve Cockshutt B.ASc., Queen's University, 2022

A Thesis Submitted in Partial Fulfillment of the
Requirements for the Degree of

MASTER OF SCIENCE

in the Department of Physics and Astronomy

We acknowledge and respect the Lək̓ʷəŋən (Songhees and Xʷsepsəm/Esquimalt) Peoples on whose territory the university stands, and the Lək̓ʷəŋən and W̱SÁNEĆ Peoples whose historical relationships with the land continue to this day.

The Impact of Extra Mixing in Low-Mass Stars on Explaining the Isotopic Compositions of Presolar Grains

by

Maeve Cockshutt B.ASc., Queen's University, 2022

Supervisory Committee

Dr. I. Dillmann, Co-supervisor (Department of Physics and Astronomy/TRIUMF)

Dr. F. Herwig, Co-supervisor (Department of Physics and Astronomy)

Abstract

Presolar oxide grains preserve isotopic signatures of stellar nucleosynthesis in oxygen-rich stellar environments, providing stringent constraints on mixing and burning processes in evolved stars. Among these, Group 2 oxygen-rich grains exhibit enhanced $^{17}O/^{16}O$ ratios and severe ^{18}O depletion, signatures widely attributed to slow extra mixing between the convective envelope and the hydrogen-burning shell, known as cool bottom processing (CBP). The physical origin and self-limiting nature of CBP have remained poorly constrained.

This work presents a self-consistent stellar evolution model of CBP operating in low-mass asymptotic giant branch (AGB) stars, implemented directly within the stellar structure. The model reproduces the full range of oxygen isotopic ratios observed in Group 2 presolar grains and is consistent with spectroscopic measurements of AGB stars of similar mass.

By evolving CBP concurrently with the stellar structure, this approach captures the development of a stabilizing mean molecular weight gradient. CBP is inherently self-limiting: an increase in the mean molecular weight gradient as small as $\Delta\mu \approx \mu_{\rm CE} \times 10^{-5}$ is sufficient to completely suppress further circulation, supporting the interpretation of CBP as a slow, low-energy circulation confined to the radiative zone. Modest variations in the depth and efficiency of mixing reproduce the observed spread in isotopic ratios, highlighting both the robustness and degeneracy of CBP within this stabilizing framework.

A complementary nuclear-physics sensitivity study identified the $^{17}O(p,\alpha)^{14}N$ reaction as the dominant source of uncertainty in predicted oxygen isotopic ratios, with smaller but measurable contributions from $^{18}O(p,\alpha)^{15}N$ and $^{16}O(p,\gamma)^{17}F$. For the $^{17}O(p,\alpha)^{14}N$ reaction, simulations that best reproduce Group 2 presolar grain compositions preferentially favor either the JINA Reaclib rate, the indirect measurement of Sergi et al. (2020), or the lower bound from Rapagnani et al. (2025), while adoption of higher rates systematically degrades agreement with the grain data.

Comparisons with 3D hydrodynamics simulations suggest that wave-driven mixing enhanced by rapid rotation may plausibly approach the efficiency required by CBP, supporting it as a viable underlying mechanism for the parameterized extra mixing.

Contents

List of Tables

List of Figures

ACKNOWLEDGEMENTS

I would like to thank Dr. Falk Herwig and Dr. Iris Dillmann for their wisdom, patience, and kindness. Falk, you have taught me to dream of the stars and to always ask new questions. You have shown me how to investigate every path with curiosity and rigor. Iris, you have revealed the nucleus to me and helped me turn ideas into concrete results. You have taught me how to communicate my findings with clarity.

I am also deeply grateful to Dr. Pavel Denissenkov, who taught me the programming skills I needed for this work. Your patience and generosity with your time are truly appreciated.

To my parents: you have shown me such incredible love and support. You reminded me I am mighty when I was low and have always been there for me. Thank you for all you have given me.

Finally, to Mallory, Ben, Claire, Josh, and Adrienne: I could not have imagined forming such strong friendships in only two years. You have celebrated with me and encouraged me. I am so grateful for the community we have built together.

DEDICATION

For my parents: who's love has always been boundless. I am truly fortunate.

Chapter 1

Introduction

1.1 Problem Statement

Presolar grains are microscopic mineral condensates that formed in the outflows of stars prior to the formation of the Solar System and were later incorporated into primitive meteorites. Because they preserve isotopic compositions that reflect the nucleosynthetic environments of their parent stars, presolar grains provide a direct record of stellar evolution and nuclear processing. Among these, oxygen-rich presolar grains are of particular interest, as their oxygen isotopic ratios offer strong constraints on mixing and burning processes in red giant branch and asymptotic giant branch stars.

A subset of these grains, Group 2 oxides, exhibit elevated $^{17}O/^{16}O$ ratios and severely depleted $^{18}O/^{16}O$ ratios. Their oxygen isotopic compositions point to low-mass red giant and asymptotic giant branch stars as possible stellar sources. However, these compositions cannot be reproduced by standard stellar evolution models that include only canonical convective mixing. Instead, they imply additional transport of envelope material into regions near the hydrogen-burning shell, where proton-capture reactions partially process the material before it is returned to the stellar surface.

One additional transport mechanism is cool bottom processing: a slow, non-convective circulation that connects the convective envelope with hotter layers just above the hydrogen-burning shell. Cool bottom processing (CBP) can account for the selective destruction of ^{18}O through the $^{18}O(p,\alpha)^{15}N$ reaction, while enhancing ^{17}O via CNO-cycle processing. Despite its success in reproducing observed isotopic patterns, the physical origin, depth, and efficiency of CBP remain poorly understood, and it is not yet clear what mechanism drives this mixing.

The central problem addressed in this thesis is whether secular CBP operating in low-

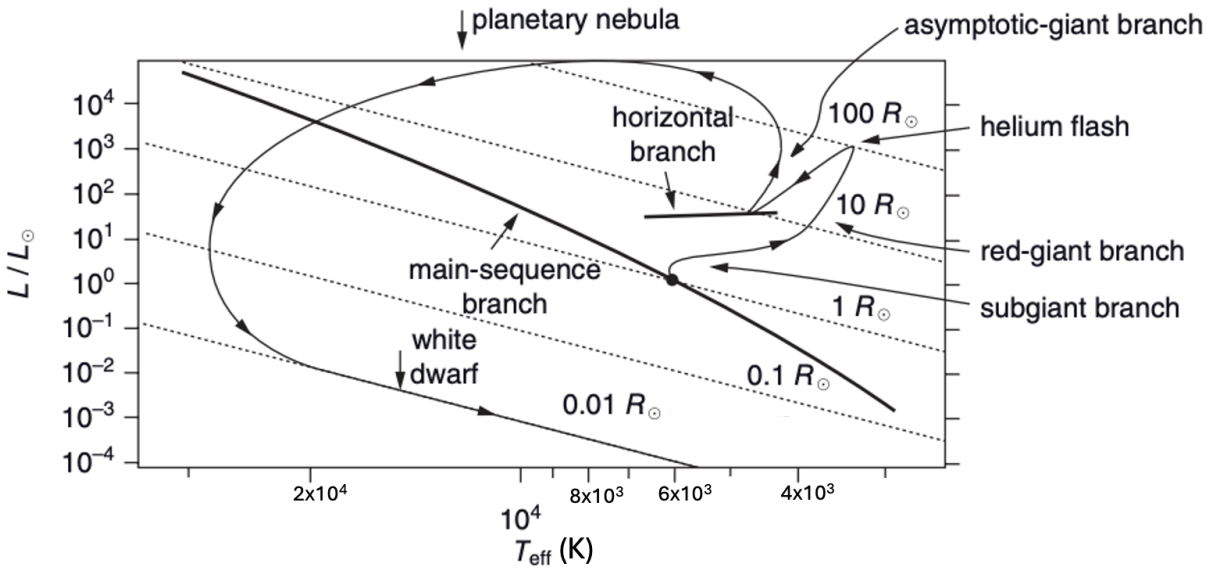

Figure 1.1: A Hertzsprung-Russell diagram of a one solar mass star with evolutionary stages labeled (LeBlanc, 2010).

mass AGB stars can quantitatively reproduce the oxygen isotopic compositions observed in Group 2 presolar grains, and what physical constraints such grains place on the nature of the mixing process. In particular, this work examines how the depth and efficiency of CBP, the stabilizing influence of the mean molecular-weight gradient, and uncertainties in key proton-capture reaction rates collectively shape the predicted isotopic signatures. By confronting stellar models with presolar grain data, this study seeks to clarify both the astrophysical conditions under which CBP operates and the extent to which presolar grains can be used as diagnostics of extra mixing in evolved stars.

1.2 Stellar Evolution

The following section will outline the evolution of a star and is based on Kippenhahn et al. (2012). Figure 1.1 illustrates the evolution of a 1 $M_\odot$ star in a Hertzsprung-Russell diagram (HRD) (LeBlanc, 2010).

1.2.1 Pre-Main Sequence Evolution

Stars begin their lives as condensations (prestellar cores) within cold, dense regions of molecular clouds. Gravitational instability within these clouds leads to the formation of a proto-

stellar core, which contracts and heats due to the release of gravitational potential energy. During this contraction, the object moves along the Hayashi track, characterized by a nearly constant effective temperature and decreasing luminosity.

Initially fully convective, the protostar transports energy primarily through bulk motion of material, allowing efficient mixing throughout its interior. As the internal temperature rises and the opacity decreases, radiation becomes the dominant mode of energy transport in the central regions, leading to the formation of a radiative core where energy is carried outward by photon diffusion rather than by convective motion. This transition marks the onset of a stratified structure in which mixing is confined to the outer convective envelope. Contraction continues until the central temperature becomes sufficient ($T_c \gtrsim 10^7\,\mathrm{K}$) to initiate sustained hydrogen fusion via the proton-proton (pp) chain. At this point, the star reaches hydrostatic and thermal equilibrium and has arrived on the *zero-age main sequence* (ZAMS).

The time required to reach the ZAMS depends strongly on stellar mass. Low-mass stars ($M \lesssim 2\mathrm{M}_\odot$) may take tens of millions of years, whereas higher-mass stars evolve more rapidly due to higher core pressures and temperatures during collapse. The metallicity of the star also subtly affects the pre-main sequence duration by influencing the opacity and the efficiency of energy transport. Opacity measures the resistance of stellar material to the flow of radiation, determining how efficiently energy moves outward through the star.

Though the pre-main sequence phase is short relative to the duration of the main sequence, it sets the initial internal structure and composition profiles of the star that impact subsequent evolution, including convective boundary locations and the onset of core hydrogen burning.

1.2.2 Main Sequence Evolution and Hydrogen Burning

Hydrostatic hydrogen burning marks the beginning of the main sequence (MS) phase in stellar evolution, when the core temperature and density become sufficient to initiate sustained thermonuclear fusion. The dominant mechanism by which hydrogen is converted into helium depends primarily on the stellar mass and chemical composition (metallicity). In low-mass stars such as the Sun, hydrogen fusion proceeds primarily via the proton-proton (pp) chain, while in more massive and metal-rich stars, the carbon-nitrogen-oxygen (CNO) cycle dominates energy generation.

Ignition Conditions

Hydrogen burning begins when the core temperature exceeds approximately 4 million K (MK), enabling the Coulomb barrier between protons to be overcome via quantum tunneling (Bethe, 1939). For a typical pre-main-sequence star, this ignition occurs once sufficient gravitational contraction raises the central temperature and density, halting the contraction via thermal pressure from nuclear energy generation.

Proton-Proton Chain

The pp chain dominates in stars with masses below about 1.3 $M_\odot$, where the core temperatures remain below 15 MK. It consists of a sequence of thermonuclear reactions in which hydrogen nuclei (protons) fuse to form helium. Through a series of intermediate steps, four protons are ultimately converted into an alpha particle (^{4}He), releasing positrons, neutrinos, and photons. The energy arises from the small difference in mass between the initial protons and the final products and is released as kinetic energy and radiation according to $E = \Delta m c^2$.

The net Q-value for the conversion

$$4p \rightarrow {}^4\mathrm{He} + 2e^+ + 2\nu_e \tag{1.1}$$

is $Q \simeq 26.73\,\mathrm{MeV}$, of which a fraction $\approx 2\%$, 4%, and 29% for the pp-I, pp-II, and pp-III branches respectively, is carried away by neutrinos. Consequently, the energy actually deposited in the star is $\approx 26.2\,\mathrm{MeV}$ for the pp-I branch, $\approx 25.7\,\mathrm{MeV}$ for pp-II, and $\approx 19\,\mathrm{MeV}$ for the pp-III branch (the lower value reflecting the very energetic ^{8}B neutrinos) (Kippenhahn et al., 2012). The main branch of this network, the pp-I chain, proceeds as:

$$\begin{aligned} p + p &\rightarrow d + e^+ + \nu_e \\ d + p &\rightarrow {}^3\mathrm{He} + \gamma \\ {}^3\mathrm{He} + {}^3\mathrm{He} &\rightarrow {}^4\mathrm{He} + 2p \end{aligned} \tag{1.2}$$

The rate-limiting step is the initial $p + p$ fusion via the weak interaction, which is responsible for the long main sequence lifetimes of low-mass stars. The pp chain's relatively weak temperature dependence ($\epsilon_{\mathrm{pp}} \propto T^4$) compared to the steep scaling of the CNO cycle ($\epsilon_{\mathrm{CNO}} \propto T^{16\text{–}20}$) enables stable energy production over long timescales.

Beyond the **pp-I chain**, two additional branches operate at higher core temperatures ($T \gtrsim 15$ MK). In the **pp-II chain**, a ^{3}He nucleus fuses with an existing ^{4}He to form ^{7}Be,

which subsequently captures an electron to produce ^{7}Li and a neutrino; the ^{7}Li then captures a proton to produce ^{8}Be and yield two ^{4}He nuclei. In the **pp-III chain**, ^{7}Be captures a proton to form ^{8}B, which undergoes β^{+} decay to ^{8}Be. The resulting ^{8}Be promptly disintegrates into two ^{4}He nuclei. This branch also produces high-energy neutrinos (up to $\sim$15 MeV) since it produces ^{8}B. Although the pp-III chain contributes only a small fraction of the Sun's total energy output, it plays a crucial role in the observable solar neutrino spectrum. The relative importance of these branches is strongly temperature-dependent, with the pp-I chain dominating at lower core temperatures, while the pp-II and especially the pp-III chains become increasingly favored as the temperature rises due to their higher Coulomb barriers and steeper temperature sensitivities.

CNO Cycle

In more massive stars ($M \gtrsim 1.3$ M$_{\odot}$), the core temperatures exceed 15 MK, activating the CNO cycle, in which pre-existing carbon, nitrogen, and oxygen nuclei act as catalysts for hydrogen fusion. The dominant CNO-I cycle proceeds as follows:

$$\begin{aligned} {}^{12}\mathrm{C} + p &\rightarrow {}^{13}\mathrm{N} + \gamma \\ {}^{13}\mathrm{N} &\rightarrow {}^{13}\mathrm{C} + e^{+} + \nu_e \\ {}^{13}\mathrm{C} + p &\rightarrow {}^{14}\mathrm{N} + \gamma \\ {}^{14}\mathrm{N} + p &\rightarrow {}^{15}\mathrm{O} + \gamma \\ {}^{15}\mathrm{O} &\rightarrow {}^{15}\mathrm{N} + e^{+} + \nu_e \\ {}^{15}\mathrm{N} + p &\rightarrow {}^{12}\mathrm{C} + {}^{4}\mathrm{He} \end{aligned} \tag{1.3}$$

The net result is again the fusion of four protons into one helium nucleus,

$$4p \rightarrow {}^{4}\mathrm{He}^{2+} + 2e^{+} + 2\nu_e + 26.73 \text{ MeV}, \tag{1.4}$$

releasing 26.73 MeV of energy per cycle—equal to the proton–proton chain. However, a larger fraction of this energy is carried away by neutrinos, and the rate of energy production depends far more steeply on temperature ($\epsilon_{\mathrm{CNO}} \propto T^{17}$), making the CNO cycle the dominant hydrogen-burning process in hotter, more massive stars and strongly centralized burning in massive stars.

At higher temperatures ($T \gtrsim$ 25–30 MK), additional branches of the CNO cycle become active, collectively referred to as CNO-II, CNO-III, and CNO-IV. These involve reactions on ^{17}O, ^{18}O, and ^{19}F nuclei, linking the CNO network to the Ne–Na and Mg–Al cycles.

While these secondary branches contribute little to overall energy generation, they play a key role in setting the isotopic abundances of oxygen, nitrogen, and fluorine in stellar interiors and ejecta, and are therefore essential to studies of nucleosynthesis and presolar grain compositions.

Dependence on Mass and Metallicity

The division between energy production in the pp chains and CNO cycle is not strictly fixed by mass but is sensitive to metallicity. Higher metallicity enhances the initial abundance of CNO nuclei, promoting the CNO cycle at slightly lower stellar masses. Conversely, in metal-poor environments, stars may remain pp-dominated even above $1.3\mathrm{M}_{\odot}$. The MS lifetime scales roughly with mass as $t_{\mathrm{MS}} \propto M/L$, and since luminosity ($L \propto M^{3-4}$) for MS stars, heavier stars evolve much more rapidly.

Structural Evolution During the Main Sequence

Low-mass stars with $M < 1.5$ $\mathrm{M}_{\odot}$ develop radiative cores and convective envelopes during hydrogen burning, whereas higher-mass stars possess convective cores due to the steep temperature dependence of the CNO cycle. These structural differences influence how chemical species are mixed and preserved during the main sequence phase.

1.2.3 Red Giant Branch Evolution

After a low- to intermediate-mass star ($M \lesssim 8$ $\mathrm{M}_{\odot}$) exhausts hydrogen in its core, it leaves the MS and begins ascending the red giant branch (RGB). This phase is marked by profound changes in the internal structure and surface properties of the star, primarily due to hydrogen shell burning surrounding an inert helium core (Figure 1.2). As the core contracts and heats, the surrounding hydrogen shell ignites, driving the expansion of the outer envelope and increasing the stellar luminosity.

Onset of First Dredge-Up

Once hydrogen is exhausted in the core, the outer convective envelope deepens towards the center of the star as it ascends the RGB. Ascent along the RGB is illustrated by an increase in luminosity and a decrease in surface temperature in Figure 1.1. This first "dredge-up" mixes material from the partially H-burned layers into the envelope, altering surface abundances. Key signatures include decreases in surface $^{12}\mathrm{C}/^{13}\mathrm{C}$ ratio and increases in $^{14}\mathrm{N}$ abundance

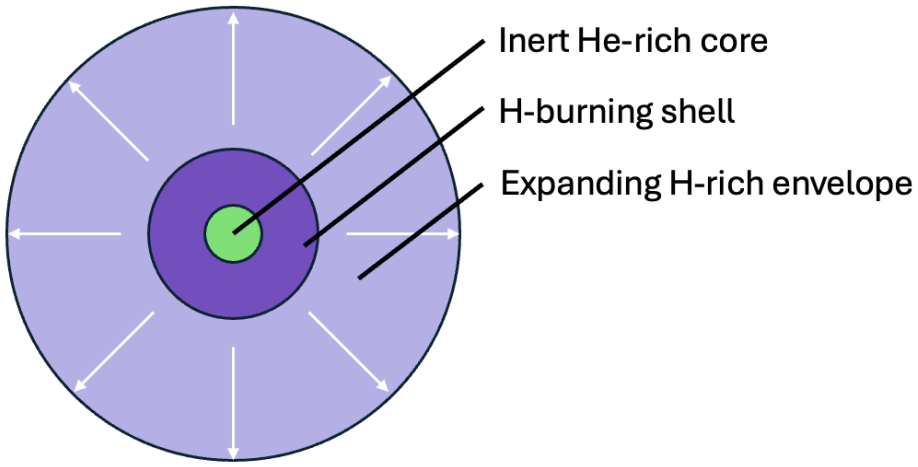

Figure 1.2: A sketch of a low-mass star that has finished core H-burning and is burning H in a shell surrounding the core. This star would be found on the RGB in Figure 1.1.

due to CN-cycle processing, meaning partial or complete CNO burning. These changes are crucial observational constraints on internal mixing processes.

Core Contraction and Hydrogen Shell Burning

Once the central hydrogen is depleted, the core is composed predominantly of helium and becomes electron-degenerate in stars with masses $\lesssim 2.2$ $M_\odot$. The loss of pressure support from fusion causes the core to contract and heat up, while hydrogen fusion continues in a thin shell surrounding the core. The energy generated by this shell burning leads to a dramatic expansion of the outer layers, causing the radius of the star to increase by up to two orders of magnitude.

As the hydrogen-burning shell moves outward in mass coordinate but inward in radius, the luminosity increases significantly — by up to a factor of ~ 100 — and the star cools at the surface due to expansion. This results in a movement on the HRD toward lower effective temperatures and higher luminosities, characteristic of Red Giants as illustrated in Figure 1.1.

RGB Bump and Mean Molecular Weight Discontinuity

As the hydrogen-burning shell advances outward in mass coordinate , it eventually encounters a sharp change in the mean molecular weight (μ). This discontinuity marks the deepest

penetration of the convective envelope during the first dredge-up, separating material that was mixed during dredge-up from the unprocessed layers below. The *mean molecular weight*, μ, is the average mass per free particle (ions, atoms, and electrons) in a gas, expressed in units of the atomic mass. It quantifies how many particles are available per unit mass to contribute to the gas pressure. In a fully ionized mixture of elements with mass fractions X_i, atomic numbers Z_i, and mass numbers A_i, the mean molecular weight(μ) is given by:

$$\mu = \frac{1}{\sum X_i \frac{1+Z_i}{A_i}}. \tag{1.5}$$

Regions with higher μ correspond to fewer particles per unit mass and therefore lower gas pressure at a given temperature. Gradients in μ can stabilize a star against convection: when a fluid element is displaced outward, toward regions of lower pressure and temperature, it enters a layer of higher μ and becomes denser than its surroundings, causing it to sink back to its original position. This encounter produces a temporary drop in luminosity, known as the *RGB bump*, observed in both star clusters and individual field stars.

This μ barrier plays a crucial role in inhibiting extra mixing processes in standard stellar models. However, observational evidence for changes in surface abundances after the RGB bump — such as further decreases in $^{12}C/^{13}C$ and lithium — suggest that some non-standard mixing operates beyond this point (Charbonnel and Zahn, 2007).

1.2.4 Core Helium Burning and the Horizontal Branch

Following the tip of the RGB, identified on the HRD as the most luminous and coldest point of the RGB (see Figure 1.1), low- and intermediate-mass stars ignite helium in their cores. The nature of this ignition depends critically on the degeneracy of the core at the onset of helium burning. In stars with masses $\lesssim 2.0$ $M_\odot$ (with the exact value dependent on metallicity), the helium core is electron-degenerate during the ascent of the RGB. Helium ignition then occurs explosively via the *helium flash*—a thermonuclear runaway driven by the degeneracy pressure which decouples pressure from temperature. Although the total energy released is substantial ($\sim 10^{10}$ $L_\odot$), it is absorbed by the surrounding layers and does not appear at the surface. As the core expands and degeneracy is lifted, the star settles into a new equilibrium configuration with stable core helium burning.

For stars with $\gtrsim 2.0$ $M_\odot$, the core is non-degenerate at the onset of helium burning, and ignition proceeds quiescently. Regardless of ignition details, stars in this phase move from the RGB to a location on the HRD known as the *Horizontal Branch* (for low-metallicity

stars). During this stable phase, helium burning in the core proceeds primarily through the triple-α reaction, which occurs in two steps via an unstable intermediate:

$$\begin{aligned} {}^4\mathrm{He} + {}^4\mathrm{He} &\rightleftharpoons {}^8\mathrm{Be}, \qquad (\text{unbound by } \approx 92 \text{ keV}) \\ {}^8\mathrm{Be} + {}^4\mathrm{He} &\rightarrow {}^{12}\mathrm{C}^*(7.65 \text{ MeV}) \rightarrow {}^{12}\mathrm{C} + \gamma \end{aligned} \tag{1.6}$$

Here ^{8}Be is extremely short-lived (lifetime $\tau \sim 10^{-16}$s), so only a tiny, steady-state population exists at helium-burning temperatures and densities. The second step proceeds through the *Hoyle state* in ^{12}C at 7.65 MeV, whose radiative decay to the ground state provides the net energy release of the triple-α process (overall $Q \simeq 7.27$ MeV) (Hoyle, 1954).

^{12}C can capture an additional α particles to form ^{16}O:

$$^{12}\mathrm{C} + \alpha \rightarrow {}^{16}\mathrm{O} + \gamma. \tag{1.7}$$

The relative rates of the reactions in equations 1.6 and 1.7 determine the carbon-to-oxygen ratio in the resulting CO core, a quantity with important consequences for later stellar evolution and white dwarf structure.

Surrounding the convective core where helium is burning, a hydrogen-burning shell remains active, contributing to core growth. The envelope is typically stable and radiative during this phase, though low levels of mass loss may continue via radiation-driven winds.

Core helium burning lasts for $\sim$ 100 million years for a 1 $M_\odot$ star (significantly shorter than the MS lifetime). Once central helium is exhausted, the star begins its evolution along the Asymptotic Giant Branch (AGB) in the HRD.

1.2.5 Thermally Pulsing Asymptotic Giant Branch (TP-AGB)

The AGB represents a late evolutionary phase for low- and intermediate-mass stars ($\sim$0.8–8 $M_\odot$), occurring after the exhaustion of core He-burning. Stars on the AGB exhibit a double-shell burning structure, characterized by alternating hydrogen and helium shell burning around an inert, degenerate carbon-oxygen (CO) core. The AGB phase is typically divided into two sub-phases: the early-AGB phase (E-AGB), dominated by quiescent helium shell burning, and the thermally pulsing AGB phase (TP-AGB), where episodic helium shell flashes dramatically alter the stellar structure and surface composition.

AGB Onset and Evolutionary Conditions

A star enters the AGB phase once core helium burning ceases and a CO core forms. Stars that develop a CO core without reaching conditions necessary for further core burning (e.g., carbon ignition) proceed to the AGB phase. This typically includes stars with initial masses $M \lesssim 8\ \mathrm{M}_\odot$, although the precise threshold depends on composition and mixing treatments (Kippenhahn et al., 2012). Stars with $M > 8\ \mathrm{M}_\odot$ ignite carbon in the core and evolve along a separate path, eventually producing oxygen-neon white dwarfs or core-collapse supernovae.

In contrast, lower-mass stars ($M \lesssim 0.5\ \mathrm{M}_\odot$) can never achieve He-burning (LeBlanc, 2010). Instead, they will evolve to form helium white dwarfs without experiencing the AGB phase.

Internal Structure and Shell Burning Dynamics

During the AGB phase, the star consists of:

- An inert, degenerate CO core (no active fusion).
- A thin He-burning shell, where triple-α reactions generate carbon.
- A H-burning shell, which produces helium that is periodically burned by the He-burning shell.
- An extended convective envelope.

These burning shells are thermally and spatially decoupled, and their interaction governs the evolution of the stellar structure. The hydrogen shell burns quiescently and contributes to a gradual buildup of helium ash atop the CO core. Once a critical mass of helium is reached, the helium shell ignites in a thermally unstable fashion, producing a *thermal pulse* or helium shell flash.

Thermal Pulses and Convective Envelope Response

Thermal pulses occur on timescales of 10^4–10^5 years, depending on stellar mass and metallicity. Each pulse initiates with a brief (∼few hundred years) but intense burst of energy ($L_{\mathrm{He}} \sim 10^6\, L_\odot$) from the helium shell, leading to expansion of the intershell region and temporary quenching of hydrogen burning.

During the interpulse periods, hydrogen shell burning steadily deposits helium onto the core. When the helium shell becomes sufficiently compressed, it ignites in a thin, degenerate

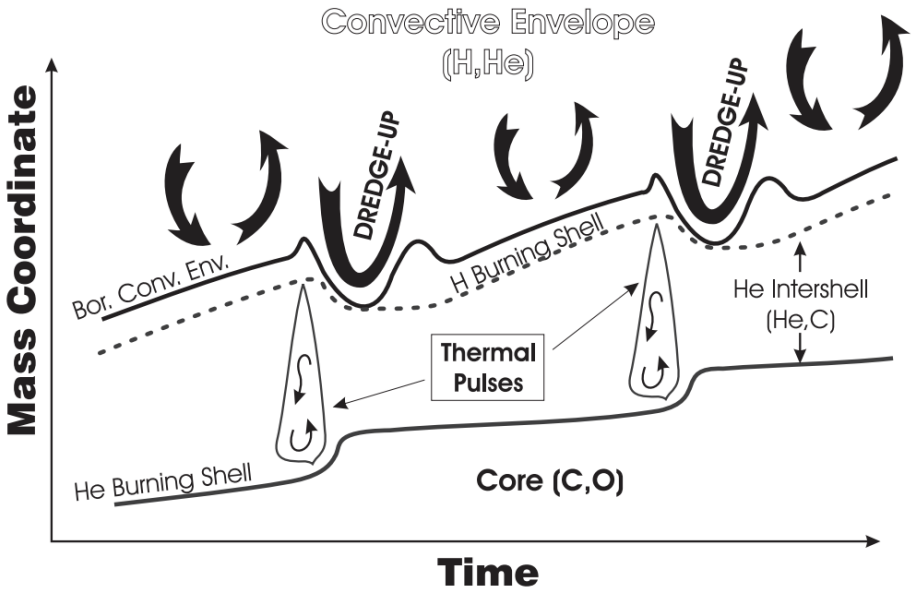

Figure 1.3: Schematic of the radial structure of the burning shells during the TP-AGB phase, illustrating TDU transports material between the convective envelope and the H-burning shell. Note that the durations of the thermal pulses and subsequent TDU episodes are not to scale relative to the interpulse periods (Straniero et al., 2006).

layer, producing a thermal pulse. The pulse drives convection in the intershell region (between the hydrogen- and helium-burning shells), temporarily extinguishing hydrogen burning. In more massive or evolved stars ($\sim$1.3–8 $M_{\odot}$), the expansion caused by the pulse may allow the convective envelope to deepen and penetrate into the intershell region — an event known as the *third dredge-up* (TDU). This process mixes the products of helium burning to the surface. Figure 1.3 illustrates the process of TDU. TDU is not guaranteed to occur after every pulse. It typically requires a sufficiently massive core and envelope, and may be delayed until multiple pulses have occurred. Some low-mass stars may never experience an efficient TDU without additional mixing mechanisms (e.g., convective overshoot). After the intershell cools and contracts, hydrogen burning reignites and the cycle continues.

Each thermal pulse is associated with characteristic structural variations:

- Contraction of the hydrogen shell and envelope before the pulse.
- Expansion of the envelope and suppression of H burning during the pulse.
- Re-establishment of quiescent hydrogen burning post-pulse.

These cycles also drive time-dependent changes in the radii of the core, burning shells, and

convective envelope, with pulse-driven convection temporarily reaching the helium intershell. The radial structure contracts and expands by several tenths of a solar radius in response to these pulses.

1.2.6 Heavy-Element Nucleosynthesis in AGB Stars

The following section will outline nucleosynthesis beyond beyond iron via neutron capture processes and is based on Herwig (2013). During the TP-AGB phase, the conditions established by recurrent thermal pulses and subsequent dredge-up episodes enable the synthesis of elements heavier than iron via the slow neutron-capture process (*s*-process) (Burbidge et al., 1957). This nucleosynthesis occurs primarily within the helium intershell—the region between the H- and He-burning shells—where neutron sources are activated during and between thermal pulses.

Two key neutron-producing reactions operate in this environment. The dominant source in low-mass AGB stars ($M \lesssim 3$ M$_\odot$) is the ^{13}C(α,n)^{16}O reaction, which occurs radiatively during the interpulse period at temperatures near 0.09 GK. The required ^{13}C forms in a narrow region (the ^{13}C *pocket*) at the top of the intershell, where protons from the envelope partially mix into ^{12}C-rich material after a third dredge-up event. The ^{22}Ne(α,n)^{25}Mg reaction is also activated at higher temperatures ($T \gtrsim 0.3$ GK) during the convective phase of a thermal pulse, providing short but intense bursts of neutrons (Herwig, 2000).

The neutrons released in these reactions are captured by Fe-peak seed nuclei to form heavier isotopes up to ^{209}Bi through successive (n, γ) captures and β^- decays. The resulting *s*-process elements—such as Sr, Ba, and Pb—are mixed into the convective envelope during subsequent third dredge-up episodes, enriching the stellar surface and ultimately the stellar wind with heavy elements. This enrichment is responsible for the observed *s*-process signatures in AGB and post-AGB stars, planetary nebulae, and carbon-rich presolar grains.

The *s*-process represents one of three primary neutron-capture nucleosynthesis pathways. The rapid neutron-capture process (*r*-process) occurs in environments with extremely high neutron fluxes, such as neutron star mergers and certain core-collapse supernovae, where nuclei capture neutrons faster than they can β-decay (Burbidge et al., 1957). The intermediate (*i*-) process, which operates at neutron densities between those of the *s*- and *r*-processes ($n_n \sim 10^{13}$–$10^{15}\,\mathrm{cm}^{-3}$), may occur during proton-ingestion events in early AGB stars or rapidly accreting white dwarfs Cowan and Rose (1977)(Denissenkov et al., 2017).

The efficiency and resulting abundance pattern of the *s*-process depend sensitively on stellar mass, metallicity, and mixing processes at the He-intershell boundary, particularly

the extent of proton penetration that determines the ^{13}C pocket size (Herwig, 2000). The heavy-element yields from AGB stars contribute significantly to the chemical evolution of the Galaxy, providing one of the dominant sources of elements beyond iron in the solar neighborhood.

1.2.7 Mass Loss and Termination of AGB Evolution

Mass loss plays a central role during the TP-AGB phase, gradually removing the stellar envelope and ultimately terminating the AGB phase evolution. While mass loss begins during the early AGB, it becomes significantly more intense during the TP-AGB phase due to increased luminosity, low surface gravity, and large-amplitude pulsations. The ignition of thermal pulses further enhances envelope expansion. In stars that undergo TDU, the surface enrichment in carbon increases atmospheric opacity, which lowers the effective temperature and causes the outer layers to expand and cool. These cooler, denser conditions allow molecules to form and subsequently condense into dust grains. This dust, especially in carbon-rich stars, enables efficient radiation-driven winds, leading to mass loss rates exceeding 10^{-5} $M_\odot$ yr^{-1}. However, substantial mass loss can also occur in stars that do not experience strong TDU, especially near the end of the TP-AGB, as pulsations and dust-driven outflows become more effective. The progressive loss of envelope mass eventually leads to the cessation of thermal pulses and the transition to the post-AGB phase.

Eventually, the envelope mass becomes too small to support continued thermal pulsing and dredge-up. The star exits the AGB phase and begins evolving toward the white dwarf cooling track, typically as a central star of a planetary nebula.

Mass loss also determines whether the star will become carbon-rich (C/O$>$ 1) by enriching the envelope with dredged-up carbon. For some metallicities and mixing efficiencies, carbon enrichment is avoided entirely, resulting in oxygen-rich dust production, which is crucial for the formation of Group 2 presolar grains (see Section 1.3.3.

1.2.8 Post–TP-AGB Evolution

Following the TP-AGB phase, a star undergoes substantial structural and mass-loss–driven changes as it evolves toward its final state as a white dwarf. Once the envelope mass is largely expelled through intense stellar winds, hydrogen- and helium-shell burning cease to be sustained, and the convective envelope recedes. The star leaves the AGB track, moving rapidly leftward across the HRD, getting hotter at nearly constant luminosity.

This brief transitional stage is known as the post-AGB or pre–planetary nebula phase. During this period, the stellar core—now largely composed of carbon and oxygen—contracts and heats, while the ejected envelope expands and becomes ionized by ultraviolet radiation from the increasingly hot central star, forming a planetary nebula. The duration of this phase depends strongly on the remaining envelope mass and the core mass, typically lasting between 10^3 and 10^4 years for low-mass stars.

Eventually, nuclear burning ceases entirely, and the central star cools and dims as a white dwarf (moves down and to the right in Figure 1.1). The final white dwarf mass reflects the core mass reached at the end of the TP-AGB, linking the AGB phase to the observed initial–final mass relation. The expelled envelope enriches the interstellar medium with products of nucleosynthesis, particularly carbon, nitrogen, and *s*-process elements, continuing the chemical evolution of the Galaxy.

1.3 Presolar Grains

For this section descriptions from Zinner (2014) are used.

1.3.1 Types and Origins of Presolar Grains

Presolar grains are submicron- to micron-sized mineral fragments that condensed in the outflows of evolved stars or in the ejecta of stellar explosions prior to the formation of the solar system. These grains survived destructions in the interstellar medium (ISM), became incorporated into the solar nebula, and locked into primitive meteorite parent bodies. Their isotopic compositions record nucleosynthetic processes from their parent stars, including AGB, novae and supernovae stars (Nittler and Ciesla, 2016; Liu, 2024).

Presolar grains are identified in primitive meteorites and interplanetary dust particles (IDPs) by their extreme isotopic anomalies relative to solar system materials. These anomalies can only be explained by nucleosynthesis in single stellar sources followed by minimal chemical processing. Based on mineralogy and isotopic signatures, presolar grains are classified into several types:

- **Silicon Carbide (SiC):** Among the most thoroughly studied grains, SiC is primarily associated with low-mass AGB stars. Mainstream, Type Y, and Type Z SiC grains exhibit $^{12}C/^{13}C$ ratios of $\sim$ 20–100 and $^{14}N/^{15}N$ ratios of $\sim$ 200–10^4, as well as *s*-process isotopic enrichments in elements such as Sr, Ba, and Mo, consistent with formation in TP-AGB stars.

- **Oxides and Silicates (e.g., Al_2O_3, $MgAl_2O_4$, $MgSiO_3$):** These oxygen-rich grains form in the outflows of oxygen-rich stars. Based on their $^{17}O/^{16}O$ and $^{18}O/^{16}O$ ratios, oxide and silicate grains are divided into Groups 1–4 (see Section 1.3.3).

- **Graphite:** Presolar graphite grains are thought to originate from a variety of stellar sources, including supernovae and, in some cases, low-metallicity AGB stars. Many graphite grains exhibit isotopic signatures characteristic of explosive nucleosynthesis, such as large excesses in ^{28}Si and the presence of short-lived radionuclides including ^{44}Ti (inferred from excess ^{44}Ca), indicating a supernova origin.

- **Nanodiamonds:** Nanodiamonds are the most abundant type of carbonaceous grains found in meteorites; however, their nanometer-scale size precludes isotopic analysis of individual grains. Bulk measurements show isotopic compositions that are close to solar for major elements, complicating definitive source attribution. Nevertheless, noble gas anomalies (e.g., Xe-HL) observed in nanodiamond separates point to a supernova contribution. Due to their near-solar bulk compositions and potential for secondary processing, the extent to which nanodiamonds represent a truly presolar grain population remains an open question.

- **Silicon Nitride and Other Rare Phases:** Less common phases such as Si_3N_4 have been linked to supernovae. Their identification is difficult due to their scarcity and small sizes (Liu, 2024).

The formation of presolar grains occurs in the extended, cooling outflows of evolved stars or in rapidly expanding supernova ejecta. Dust nucleation models indicate that grains condense once the temperature drops below 2000 K, depending on composition and gas density (Lodders and Amari, 2005). The local chemical environment—particularly the C/O ratio—plays a dominant role in determining which species condense. CO is an exceptionally stable molecule, it forms efficiently and binds nearly all of the less abundant of carbon or oxygen in the stellar outflow. As a result, only the more abundant element remains available for dust formation: carbon-rich stars ($C/O > 1$) favor the formation of SiC and graphite, while oxygen-rich stars ($C/O < 1$) primarily form silicates and oxides.

The diversity of presolar grain types thus reflects both the physical conditions of their formation sites and the nucleosynthetic history of their stellar sources, making them direct probes of stellar evolution and nucleosynthesis processes that are otherwise inaccessible.

1.3.2 Identification and Isotopic Measurement of Presolar Grains

Presolar grains are identified based on their extreme isotopic compositions, which are inconsistent with solar system materials and indicative of nucleosynthesis in specific stellar environments prior to the formation of the Solar System. These grains are found embedded in primitive meteorites, especially in the matrix of carbonaceous chondrites, and can be separated through chemical and physical techniques that exploit their unique chemical resilience and grain size distributions (Amari et al., 1995).

Isotopic compositions of presolar grains are often measured using secondary ion mass spectrometry (SIMS). SIMS allows for in situ measurement of isotopic ratios in individual grains on the order of hundreds nanometers (Zinner, 2014). Commonly measured isotopes include ^{12,13}C, ^{14,15}N, ^{16,17,18}O, ^{24,25,26}Mg, ^{26}Al (via excess ^{26}Mg), ^{27}Al, ^{40,42,43,44}Ca, and ^{46,47,48,49,50}Ti, depending on the grain type.

Grains are grouped into populations (e.g., Group 1, Group 2, etc.) based on their isotopic signatures (see Section 1.3.3), which are compared to predictions from stellar models. This grouping supports inferences about their stellar origin, such as AGB stars, supernovae, or classical novae. The wealth of isotopic data extracted from individual grains makes them a powerful probe of nucleosynthesis and stellar evolution beyond what is accessible through spectroscopy alone.

1.3.3 Oxygen-Rich Presolar Grains

Oxygen-rich presolar grains are a class of circumstellar condensates that form in the oxygen-dominated outflows of evolved stars, where the ratio of oxygen to carbon exceeds unity (O/C $>$ 1). In these environments, nearly all carbon is locked up in CO molecules, preventing the formation of carbon-rich solids and favoring the condensation of silicate and oxide minerals, the opposite is true in carbon-rich outflows. The most common types of oxygen-rich grains include silicates (both crystalline and amorphous), corrundum (Al_2O_3), and spinel ($MgAl_2O_4$).

These grains can be distinguished from one another based on their mineralogy, isotopic composition, and inferred stellar origin. Oxygen isotopic ratios (^{17}O/^{16}O and ^{18}O/^{16}O) are particularly useful for identifying the stellar sources of these grains, as different evolutionary phases and initial stellar masses imprint characteristic signatures in stellar interiors (Nittler, 1997; Nittler et al., 2008).

Based on their oxygen isotopic composition, oxide and silicate grains are commonly divided into four major groups (as illustrated in Figure 1.4):

- **Group 1**: Enriched in ^{17}O and slightly depleted in ^{18}O relative to solar. These grains are thought to originate from first dredge-up processes in low- to intermediate-mass Red Giant and AGB stars. During core hydrogen burning, the CNO cycle enhances ^{17}O while leaving ^{18}O largely unaffected. The deepening of the convective envelope during first dredge-up mixes this ^{17}O-enriched material to the surface (Nittler, 1997; Nittler et al., 2008).

- **Group 2**: Similar ^{17}O enhancements to Group 1, but with extreme depletions in ^{18}O ($^{18}\mathrm{O}/^{16}\mathrm{O} < 10^{-4}$). These compositions are indicative of additional processing beyond a standard first dredge-up, such as cool bottom processing or other forms of extra mixing (Nittler, 1997; Nittler et al., 2008).

- **Group 3**: Depleted in both ^{17}O and ^{18}O, suggesting origins in low-mass low-metallicity stars or supernovae (Nittler et al., 2008).

- **Group 4**: Enriched in both ^{17}O and ^{18}O. These grains are rare and may have originated from supernovae or high metallicity stars (Nittler et al., 2008).

The oxygen isotopic ratios are often plotted with ratios of three isotopes to visualize these groupings and compare with nucleosynthetic models. Group 2 grains, in particular, provide strong constraints on models of extra mixing in RGB and AGB stars, since their extreme ^{18}O depletion is not explained by standard stellar evolution alone. Figure 1.4 shows the oxygen abundances of the four groups of oxide grains (Liu et al., 2022).

1.4 One-Dimensional Stellar Simulations

1.4.1 From Three-Dimensional to One-Dimensional Stellar Models

Stellar interiors are intrinsically three-dimensional (3D), time-dependent, and governed by turbulent hydrodynamics, rotation, magnetic fields, and radiative transfer (Meakin and Arnett, 2007; Cristini et al., 2017). However, most stellar evolution models—including those used in nucleosynthesis studies—employ one-dimensional (1D) approximations. These models are built under the assumption of spherical symmetry, wherein all physical quantities vary only with the radial coordinate and time (Arnett et al., 2015).

The primary advantage of 1D models is computational efficiency. By reducing the dimensionality, simulations can span entire stellar lifetimes (from pre-MS to white dwarf or supernova stages) at reasonable spatial and temporal resolution (Arnett et al., 2015). These

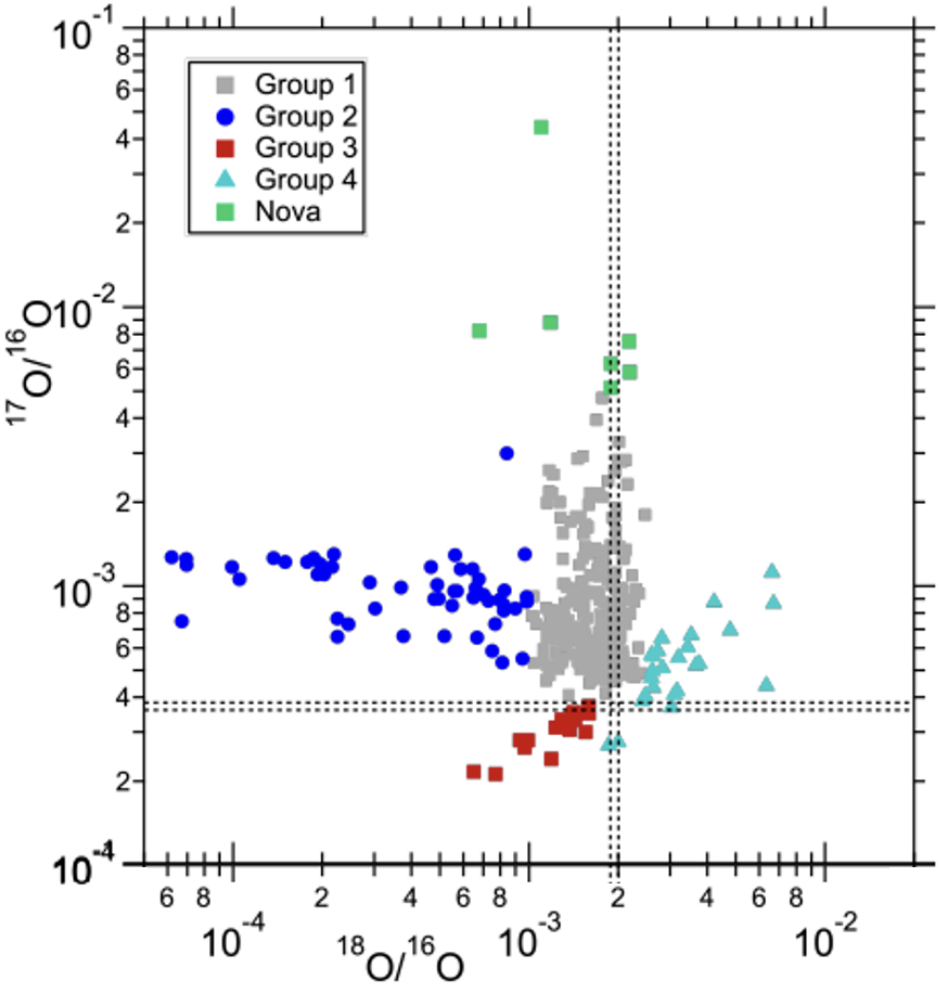

Figure 1.4: The four groups of oxide grains and grains from novaeplotted in three-isotope space (Liu, 2024).

models conserve fundamental physical quantities, such as mass, energy, and angular momentum (when included), and self-consistently solve the coupled equations of stellar structure: hydrostatic equilibrium, mass conservation, energy conservation, and energy transport (Cristini et al., 2017).

Dimensional reduction comes at the cost of significant physical detail. Multidimensional phenomena such as convection, rotation, magnetic fields, and wave transport are treated through simplified prescriptions or mixing-length theory (MLT) and calibrated against observations or simulations. Convection, for instance, is modeled as a diffusive or advective process in 1D, lacking the asymmetries, time variability, and nonlocality present in 3D (Arnett et al., 2015; Meakin and Arnett, 2007).

In particular, the 1D approximation loses:

- The detailed structure and turbulence of convective flows (e.g., plumes, overshooting, entrainment) (Meakin and Arnett, 2007; Cristini et al., 2017).
- Anisotropic processes like rotationally induced mixing, internal gravity waves, and magnetic field dynamics.
- Realistic boundary layer behavior between convective and radiative zones (Arnett et al., 2015).

Despite these limitations, 1D models remain the standard for long-term stellar evolution and nucleosynthesis studies. Increasingly, insights from high-resolution 3D hydrodynamical simulations are used to inform or constrain 1D prescriptions, such as time-dependent convection, overshooting, and entrainment efficiencies (Arnett et al., 2015; Meakin and Arnett, 2007; Cristini et al., 2017).

1.4.2 The One-Dimensional Stellar Structure Equations

1D stellar models assume spherical symmetry, reducing the complex, 3D hydrodynamic problem to a set of coupled ordinary differential equations (ODEs) that describe how physical quantities vary with enclosed mass. These equations are solved alongside appropriate boundary conditions and a nuclear reaction network to model a star's structural and compositional evolution over time. The four canonical equations governing 1D stellar structure are:

Mass Conservation

$$\frac{dr}{dm} = \frac{1}{4\pi r^2 \rho} \tag{1.8}$$

This equation defines the radial coordinate r as a function of the enclosed mass m. It ensures that mass is distributed consistently with the local density ρ.

Hydrostatic Equilibrium

$$\frac{dP}{dm} = -\frac{Gm}{4\pi r^4} \tag{1.9}$$

This equation ensures a balance between gravitational compression and the opposing pressure gradient force. It assumes the star is in quasi-static equilibrium, i.e., that dynamical timescales are much shorter than evolutionary timescales.

Energy Conservation

$$\frac{dL}{dm} = \varepsilon_{\rm nuc} - \varepsilon_\nu + \varepsilon_g \tag{1.10}$$

Here, L is the luminosity (energy output rate) at mass coordinate m, and $\varepsilon_{\rm nuc}$ is the specific energy generation rate from nuclear reactions. The term ε_ν accounts for energy lost via neutrinos, while ε_g represents energy release from gravitational contraction when positive and energy absorption from gravitational expansion when negative.

Energy Transport

$$\frac{dT}{dm} = -\frac{GmT}{4\pi r^4 P}\nabla \tag{1.11}$$

This equation describes the temperature gradient required to transport energy outward. The temperature gradient $\nabla = d\ln T/d\ln P$ depends on the dominant energy transport mechanism:

- In radiative regions: $\nabla = \nabla_{\rm rad}$, calculated from radiative diffusion.
- In convective regions: $\nabla = \nabla_{\rm conv}$, typically estimated using MLT.

Boundary Conditions and Equation of State

To solve these equations, boundary conditions are specified at the center (e.g., $r = 0$, $L = 0$) and the surface (e.g., $P \approx 0$, T set by photospheric models). An equation of state (EOS) provides thermodynamic quantities (e.g., $P(\rho, T, \mu)$), and opacity tables are used to determine radiative transport efficiency.

Together, these equations define the evolving structure of the star. Their time dependence is introduced through changes in composition and structure due to nuclear burning, mixing,

and mass loss. (Kippenhahn et al., 2012) While simplified, this framework captures the essential behavior of stars throughout most of their lives and forms the basis of modern stellar evolution codes like MESA (Paxton et al., 2010, 2013).

1.4.3 Modules for Experiments in Stellar Astrophysics (MESA)

MESA (Modules for Experiments in Stellar Astrophysics) is a one-dimensional stellar evolution code designed to model the internal structure and composition of stars over time (Paxton et al., 2010, 2013). It solves the standard stellar structure equations with time-dependent mixing and nuclear burning, allowing for simulations from pre-MS through late stages such as the thermally pulsing AGB phase.

The code includes a wide range of physical processes relevant to stellar evolution, including convection (treated with MLT), convective overshooting, rotational mixing, mass loss, and diffusion. Nuclear burning is handled through user-selectable reaction networks, ranging from simplified energy generation chains to larger networks suitable for isotopic abundance studies. MESA also supports adaptive spatial and temporal resolution, enabling accurate treatment of thin burning shells and sharp composition gradients.

MESA is widely used in stellar astrophysics because of its flexibility, reproducibility, and extensive documentation. The output can be post-processed using extended reaction networks to study nucleosynthesis in detail.

1.4.4 The NuGrid Stellar Yields and Data Sets

The NuGrid collaboration provides a suite of stellar evolution and post-processing nucleosynthesis models that supply isotopic yields for a wide range of stellar masses and metallicities (Pignatari et al., 2016; Ritter et al., 2018). These models are particularly useful for studies of AGB and massive stars, where detailed reaction networks are required to capture the production of key isotopes of interest such as ^{16}O, ^{17}O, ^{18}O, ^{26}Al, and ^{27}Al.

NuGrid simulations combine stellar structure calculations from codes such as MESA with the multi-zone post-processing code mppnp, which follows hundreds to thousands of isotopes and their reactions through time. Post-processing allows for the efficient treatment of stellar structure in 1D models while retaining a full nuclear network in post-processing, ensuring accurate predictions of isotopic abundances for comparison with presolar grain data and spectroscopic observations.

The publicly available NuGrid data sets include stellar evolution tracks and nucleosynthesis yields for low- and intermediate-mass AGB stars, as well as massive stars that end their

lives as supernovae . These data sets provide surface abundances, interior profiles, and integrated stellar yields, making them a central resource for testing nucleosynthesis predictions and galactic chemical evolution models. In particular, the consistent treatment of stellar physics and nuclear networks across the grid enables systematic exploration of the impact of initial mass, metallicity, and mixing processes on isotopic outcomes and comparison with presolar grain data and stellar spectroscopic observations.

1.4.5 Mass Loss in 1D Stellar Models

Mass loss is a key ingredient in the evolution of low- and intermediate-mass stars, particularly in RGB and AGB stars, where it affects core growth, thermal pulse behavior, and the termination of stellar evolution (Vassiliadis and Wood, 1993) (Bloecker, 1995). In 1D stellar models, mass loss is not computed from first principles, but instead implemented through empirical or semi-empirical prescriptions based on observational trends (Schröder and Cuntz, 2007).

Reimers Mass Loss

A commonly used formula for RGB and early AGB evolution is the Reimers prescription (Reimers, 1977):

$$\dot{M}_{\text{Reimers}} = 4 \times 10^{-13}\, \eta_R \, \frac{L}{gR} \quad \left[\mathrm{M}_\odot\,\mathrm{yr}^{-1}\right] \tag{1.12}$$

where L, g, and R are the stellar luminosity, surface gravity, and radius in solar units respectively, and η_R is a scaling parameter. While simple, the Reimers formula captures the onset of wind-driven mass loss in red giants and has been widely adopted in stellar evolution modeling (Schröder and Cuntz, 2007).

Blöcker Mass Loss

To account for the more intense winds seen during the TP-AGB phase, the Blöcker prescription introduces a stronger dependence on luminosity (Bloecker, 1995):

$$\dot{M}_{\text{Blcker}} = 4.83 \times 10^{-9}\, \eta_B \left(\frac{L}{L_\odot}\right)^{2.7} \left(\frac{M}{\mathrm{M}_\odot}\right)^{-2.1} \quad \left[\mathrm{M}_\odot\,\mathrm{yr}^{-1}\right] \tag{1.13}$$

Here, η_B is a free parameter. The enhanced luminosity dependence enables the modeling of rapid envelope loss that eventually ends AGB evolution. The formula shown above omits explicit radial dependence and is used in `MESA`.

Other Prescriptions

Several alternative mass-loss prescriptions are also used in stellar evolution modeling. The Vassiliadis and Wood (1993) formula introduces a dependence on pulsation period and is calibrated to observations of Mira variable stars. Schröder and Cuntz (2007) presented a modified version of Reimers' law that includes chromospheric and temperature effects. Other empirical relations are derived from observations of stars with different properties.

Implementation in `MESA`

In `MESA`, mass-loss prescriptions are applied at the surface boundary and updated throughout the evolution. Users specify the choice of prescription and parameters. Transitions between different formulas are possible, allowing for models that, for example, use the Reimers formula during the RGB phase and switch to the Blöcker or Vassiliadis & Wood formula during the TP-AGB phase.

1.4.6 Convective Overshooting

In stellar interiors, convection is typically modeled using the MLT, which defines the convective boundary at the point where the Schwarzschild or Ledoux criterion predicts marginal stability against convection. The Schwarzschild criterion considers only the temperature gradient and identifies convection when the radiative gradient becomes steeper than the theoretical temperature gradient of an adiabatically displaced fluid element. The Ledoux criterion introduces the additional stabilizing effect of composition gradients, recognizing that a positive mean molecular weight gradient can suppress convective motion by reducing buoyancy (Ledoux, 1947). However, hydrodynamical simulations and observations indicate that convective motions do not abruptly stop at this boundary. Instead, convective elements overshoot into the formally stable radiative region due to their inertia, mixing material beyond the MLT-defined convective boundary. This process is known as *convective overshooting* Shaviv and Salpeter (1973).

Overshooting is an inherently multidimensional hydrodynamic phenomenon, but in one-dimensional (1D) stellar evolution models it must be included parametrically. Without overshooting, 1D models tend to underestimate the extent of mixing at convective boundaries, which can significantly impact stellar structure and nucleosynthesis. For example, overshooting at the convective core during the MS phase increases the core mass, extending the hydrogen-burning lifetime, while overshooting at shell boundaries during advanced

burning phases can alter dredge-up efficiency and intershell abundances (see e.g. Herwig (2000)).

Overshooting in the Adopted Model

In this work, overshooting is implemented in `MESA` using a diffusive prescription with exponential decay of convective velocities beyond the formal convective boundary. The strength of overshooting is controlled by two numbers, f and f_0, which set how far mixing extends beyond the convective boundary, measured relative to the local pressure scale height (Herwig, 2000; Paxton et al., 2010).

Following the configuration of NuGrid's dataset 2 models (Pignatari et al., 2016; Ritter et al., 2018), overshooting is applied consistently across non-burning and burning cores and shells with $f = f_0 = 0.014$ for all relevant boundaries. Additional scaling factors are introduced in certain regions to reproduce observed mixing patterns:

- **^{13}C pocket formation:** Overshoot mixing below non-burning shells is enhanced by a factor of 9, facilitating the partial mixing of protons into the helium intershell during the interpulse phase (Ritter et al., 2018).

- **He-shell flash convection:** Overshooting below the He-burning shell during thermal pulses is reduced by a factor of 0.5714 to match constraints from AGB nucleosynthesis studies.

- **He-shell flash convection:** Convective overshooting below the He-burning shell during thermal pulses is reduced by a factor of 0.5714 relative to the standard prescription in order to satisfy constraints from AGB nucleosynthesis. In particular, excessive overshoot enhances intershell mixing and overproduces ^{12}C and heavy s-process elements, leading to surface abundances inconsistent with observations of AGB stars and post-AGB objects. The adopted reduction brings the predicted intershell composition and dredge-up yields into better agreement with observational and meteoritic constraints .

Mass dependence is included through the parameters `mass_for_overshoot_full_on` and `mass_for_overshoot_full_off`, which apply full overshooting for stars above $1.8 M_\odot$ and no overshooting for stars below $1.1 M_\odot$, with a smooth transition between these limits. This prescription reflects empirical constraints from stellar clusters and eclipsing binaries across a range of stellar masses.

1.4.7 Cool Bottom Processing

Cool bottom processing (CBP) is a term used to describe slow, non-convective mixing between the convective envelope and the outer regions of the hydrogen-burning shell in evolved low-mass stars. This process is not predicted by standard stellar evolution models, which assume that chemical mixing outside formally convective regions is negligible. Instead, CBP is invoked to explain isotopic and elemental abundance patterns that cannot be reproduced by canonical FDU alone (Boothroyd and Sackmann, 1999; Nollett et al., 2003).

Location and Timing

CBP is thought to occur during the RGB phase after the hydrogen-burning shell has erased the molecular weight discontinuity left behind by the FDU (Boothroyd and Sackmann, 1999), and possibly also during the AGB phase between thermal pulses (Nollett et al., 2003). In both cases, the base of the convective envelope is located just above the hydrogen-burning shell, enabling slow circulation of envelope material down to regions hot enough for proton-capture reactions before returning it to the surface (Nollett et al., 2003). Unlike convection, which mixes material on timescales of days to months, CBP operates over much longer timescales, allowing nuclear processing to occur in the transported material (Palmerini et al., 2021).

Observational Evidence

Evidence for CBP comes primarily from observed surface abundances that deviate from predictions of standard stellar evolution models:

- **Carbon isotopes:** Post-FDU $^{12}C/^{13}C$ ratios in low-mass RGB stars are frequently observed in the range 10–15, well below the canonical value of ∼20–25 predicted by standard models. (Gilroy, 1989; Gilroy and Brown, 1991; Boothroyd and Sackmann, 1999).
- **Oxygen isotopes:** Depletions in ^{18}O and enhancements in ^{17}O in some giant stars suggest additional proton-capture processing after FDU (Harris and Lambert, 1984; Hinkle et al., 2016; Lebzelter et al., 2019; Palmerini et al., 2021).
- **Lithium:** Lithium abundances in giant stars can be explained by CBP, depending on the temperature and depth of mixing (Charbonnel and Balachandran, 2000; Kumar et al., 2020; Denissenkov et al., 2024).

- **Presolar grains:** Oxygen and aluminum isotopic ratios in certain presolar oxide and silicate grains require *incomplete* proton-capture processing, in which envelope material experiences brief exposure to H-burning temperatures ($T \sim 20$–$40\,\mathrm{MK}$) characteristic of CBP. In this regime, proton-capture reactions modify isotopic ratios without reaching nuclear equilibrium. (Nollett et al., 2003; Palmerini et al., 2021).

Proposed Mechanisms and Constraints

CBP is a phenomenological description, and several physical mechanisms have been proposed to drive it, including:

- *Thermohaline mixing* induced by a local mean molecular weight (μ) inversion created by the reaction

$$^3\mathrm{He} + {}^3\mathrm{He} \rightarrow\ 2p + {}^4\mathrm{He}. \tag{1.14}$$

  This reaction increases the number of particles per unit mass, thereby reducing the local μ below the value in the overlying layers. The resulting negative mean molecular weight gradient ($\nabla_\mu < 0$) produces a double-diffusive instability analogous to thermohaline convection in fluids with opposing temperature and compositional gradients. In stellar interiors, this instability drives slow, downward-moving "salt-finger"-like flows that transport material and heat, providing an efficient mechanism for extra mixing in low-mass red giants (Charbonnel and Zahn, 2007; Denissenkov et al., 2024).

- *Rotationally-induced mixing* occurs when differential rotation develops between the contracting stellar core and the more slowly rotating, expanding envelope. In the radiative zone separating these regions, this differential rotation gives rise to shear instabilities and large-scale meridional circulation. These processes redistribute angular momentum by smoothing radial gradients in the rotation rate, while simultaneously transporting chemical species. As angular momentum is redistributed, weak circulatory flows carry envelope material downward into hotter layers, where nuclear processing occurs, and return processed material to the surface. Rotation-driven mixing may therefore operate alongside other instabilities to sustain cool-bottom processing in low-mass red giants and AGB stars (Nollett et al., 2003; Denissenkov et al., 2024)

- *Magnetic buoyancy* can drive extra mixing if strong magnetic fields form near the base of the convective envelope or above the H-burning shell. Magnetized flux tubes created in these regions rise buoyantly through the radiative zone, carrying processed material upward toward the envelope. Their motion can also induce a slow return flow

of unprocessed material downward, producing a steady circulation that connects the envelope and burning layers. This process has been proposed as a possible mechanism for cool-bottom processing in low-mass red giants and AGB stars (Denissenkov et al., 2009; Palmerini et al., 2021).

- *Internal gravity waves* generated at convective–radiative boundaries can also induce slow mixing. These waves, excited by turbulent motions within the convective envelope, propagate into the underlying radiative zone where their dissipation deposits angular momentum and momentum flux. The resulting wave-driven circulation can modify the local rotation profile and drive weak, large-scale flows that transport material across composition gradients. Although less efficient than shear or thermohaline instabilities, gravity-wave–induced mixing may contribute to the continuous circulation required for CBP in evolved stars (Denissenkov et al., 2024).

Constraints on CBP are derived from matching observed isotopic ratios and abundance anomalies to models that adopt slow circulation. The key parameters include the maximum temperature reached by the circulating material and the mixing rate (Boothroyd and Sackmann, 1999; Nollett et al., 2003). Circulation down to $T \approx$ 30-50 MK is sufficient to modify $^{12}C/^{13}C$ and oxygen isotopes without significantly altering isotopic compositions of heavier elements. For AGB stars, slightly deeper mixing may be required to reproduce some isotopic patterns in presolar grains (Nollett et al., 2003).

1.4.8 Hot Bottom Burning

In more massive AGB stars ($M \gtrsim 4$–$5\,M_{\odot}$), proton-capture nucleosynthesis occurs directly at the base of the convective envelope through *hot bottom burning* (HBB), where temperatures exceed ∼60 MK and activate CNO-cycle reactions. Under these conditions, envelope material is processed convectively through the hydrogen-burning region, rapidly driving surface abundances toward nuclear equilibrium. Figure 1.5 schematically compares the depth and nature of mixing in HBB and CBP.

H-burning under HBB conditions leads to strong depletion of ^{18}O, enrichment of ^{17}O, and enhanced production of ^{26}Al through activation of the Mg–Al cycle. These isotopic signatures overlap with those observed in Group 2 presolar oxide and silicate grains, motivating HBB as a potential formation site for this grain population. Revisions to the $^{17}O(p,\alpha)^{14}N$ reaction rate from underground measurements have strengthened this connection by bringing HBB model predictions into closer agreement with the observed $^{17}O/^{16}O$ ratios of Group 2 grains

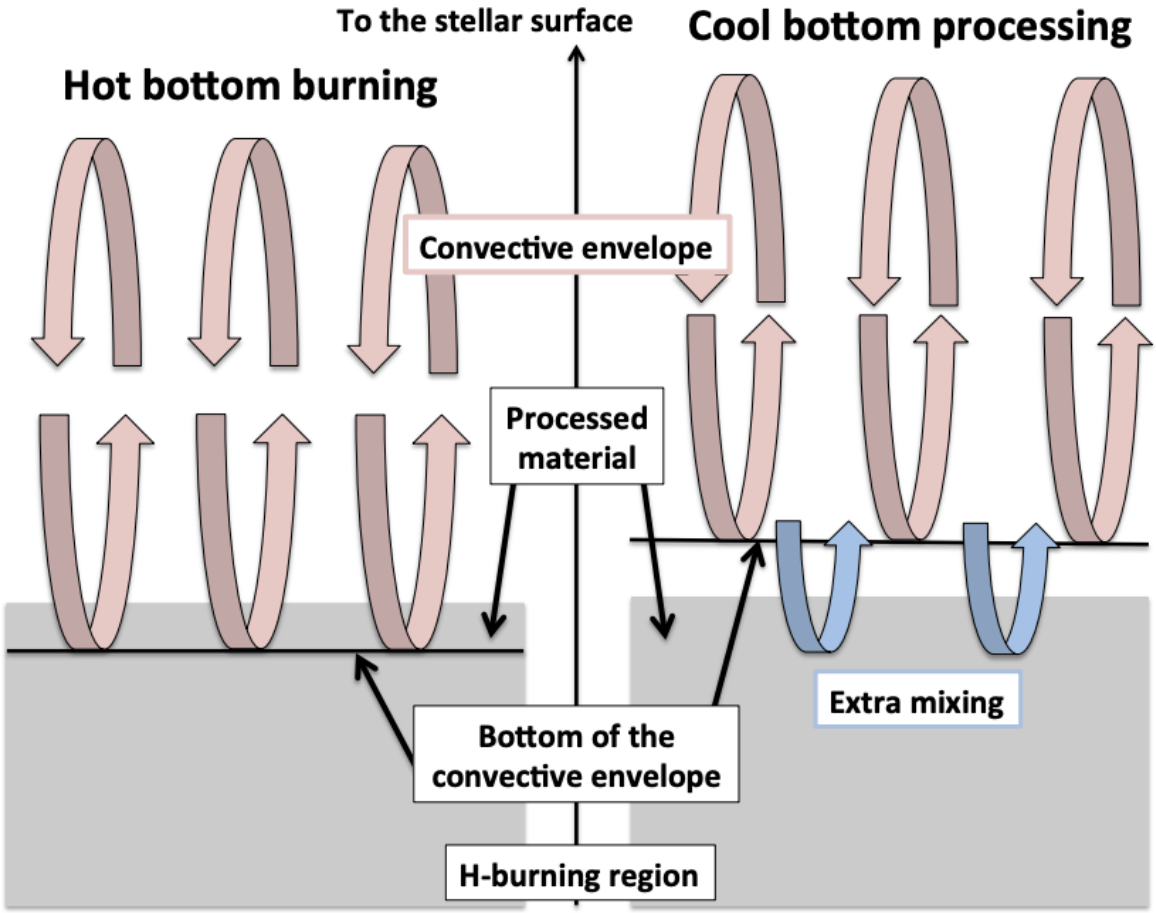

Figure 1.5: Schematic of the region near the base of the convective envelope in asymptotic giant branch stars undergoing HBB (left) and CBP (right). HBB mixes envelope material directly through H-burning regions via convection, whereas CBP relies on slower, non-convective transport to shallower burning layers (Lugaro et al., 2017).

(Bruno et al., 2016; Lugaro et al., 2017). However, as shown by Lugaro et al. (2017), HBB drives $^{18}O/^{16}O$ to values significantly lower than those measured in Group 2 grains, requiring dilution of HBB-processed material with a small fraction of near-solar composition material to recover the observed isotopic range.

HBB and CBP represent distinct physical regimes of hydrogen-burning nucleosynthesis, operating in different stellar mass ranges and with different implications for the origin of presolar grains.

1.5 Sites of Oxygen and Aluminum Isotope Production in Low-Mass Stars

1.5.1 Proton-Capture Processing of Oxygen Isotopes in Low-Mass AGB Stars

The following work focuses on the ability of CBP in low-mass AGB stars to reproduce the O isotopic ratios observed in Group 2 presolar oxide grains. Among the reactions influencing these ratios, Monte Carlo sensitivity studies in this work (see Section 4.5) identified three as the most important:

$$^{17}O(p,\alpha)^{14}N, \quad ^{18}O(p,\alpha)^{15}N, \quad \text{and} \quad ^{16}O(p,\gamma)^{17}F.$$

The first two reactions destroy ^{17}O and ^{18}O, respectively, while the third produces ^{17}O through the β^+ decay of ^{17}F.

These reactions occur in the H-burning shell, where proton-capture reactions dominate. This region lies within the radiative layer immediately below the convective envelope, where CBP can circulate material from the envelope down to the top of the burning shell. CBP only penetrates to the outer edge of the H-burning shell, where temperatures are approximately 30 MK. Burning at greater depths does not affect the surface composition or the isotopic signatures recorded in presolar grains, as these regions can not be accessed by CBP due to a stabilizing mean-molecular-weight gradient.

The material processed through CBP originates from the unburnt convective envelope. As this plasma is transported downward, it experiences partial reprocessing through the proton-capture reactions above, and is then returned to the envelope, leading to the characteristic ^{17}O enrichment and ^{18}O depletion observed in Group 2 grains.

1.5.2 ^{26}Al Creation

The ^{26}Al/^{27}Al ratio has been measured in several Group 2 oxide grains. Figures 1.6 and 1.7 show that the production of ^{26}Al during the AGB phase depends on the exchange of material between the H- and He-burning shells. In the He-burning shell, ^{12}C is generated through the triple-α reaction. Convection during a thermal pulse then mixes the ^{12}C into the H-burning shell, where it is converted into ^{14}N-rich ash via the CNO cycle. Subsequent thermal pulses carry the ^{14}N back into the He-burning shell, where it is transformed into ^{22}Ne through the chain $^{14}\mathrm{N}(\alpha,\gamma)^{18}\mathrm{F}(\beta^+)^{18}\mathrm{O}(\alpha,\gamma)^{22}\mathrm{Ne}$. In the same shell, the $^{22}\mathrm{Ne}(\alpha,n)^{25}\mathrm{Mg}$ reaction can proceed, and when the ^{25}Mg is later returned to the H-burning shell by thermal-pulse convection, it captures a proton to form ^{26}Al (Herwig, 2013). Under these H-burning conditions, production proceeds predominantly to the long-lived ground state ($T_{1/2} = 7.2 \times 10^5$ years), rather than the short-lived isomeric state ($T_{1/2} = 6.3$ s). The decay of $^{26}\mathrm{Al}^{\mathrm{g}}$ to ^{26}Mg produces the characteristic 1809 keV γ-ray line observed in the Galaxy, linking presolar grain measurements to ongoing nucleosynthesis in evolved stars (National Nuclear Data Center, 2023; Tuli, 1996).

1.6 Motivation

What physical mechanism drives the slow, non-convective mixing known as CBP in evolved, low-mass stars—and can this process account for the isotopic signatures preserved in presolar grains? This question lies at the intersection of stellar evolution and nucleosynthesis. CBP is hypothesized to connect the convective envelope of an AGB star with the outer regions of its hydrogen-burning shell, enabling partial nuclear processing of envelope material at temperatures around 30 MK. The physical origin, efficiency, and depth of this circulation remain uncertain.

Group 2 oxygen-rich grains act as probes with distinctive isotopic signatures: enhanced ^{17}O/^{16}O ratios relative to solar and ^{18}O/^{16}O ratios below 10^{-3}. These compositions cannot be reproduced by standard AGB stellar models that include only first dredge-up mixing. Instead, they imply additional transport of envelope material into regions near the hydrogen-burning shell, where proton-capture reactions can efficiently destroy ^{18}O via $^{18}\mathrm{O}(p,\alpha)^{15}\mathrm{N}$. Therefore, the isotopic record preserved in these grains offers a sensitive diagnostic of CBP in RGB and AGB stars and provides a test of stellar evolution models (Zinner, 2014).

The goal of this thesis is to determine whether secular CBP operating in low-mass AGB stars can reproduce the oxygen isotopic compositions observed in Group 2 grains and to

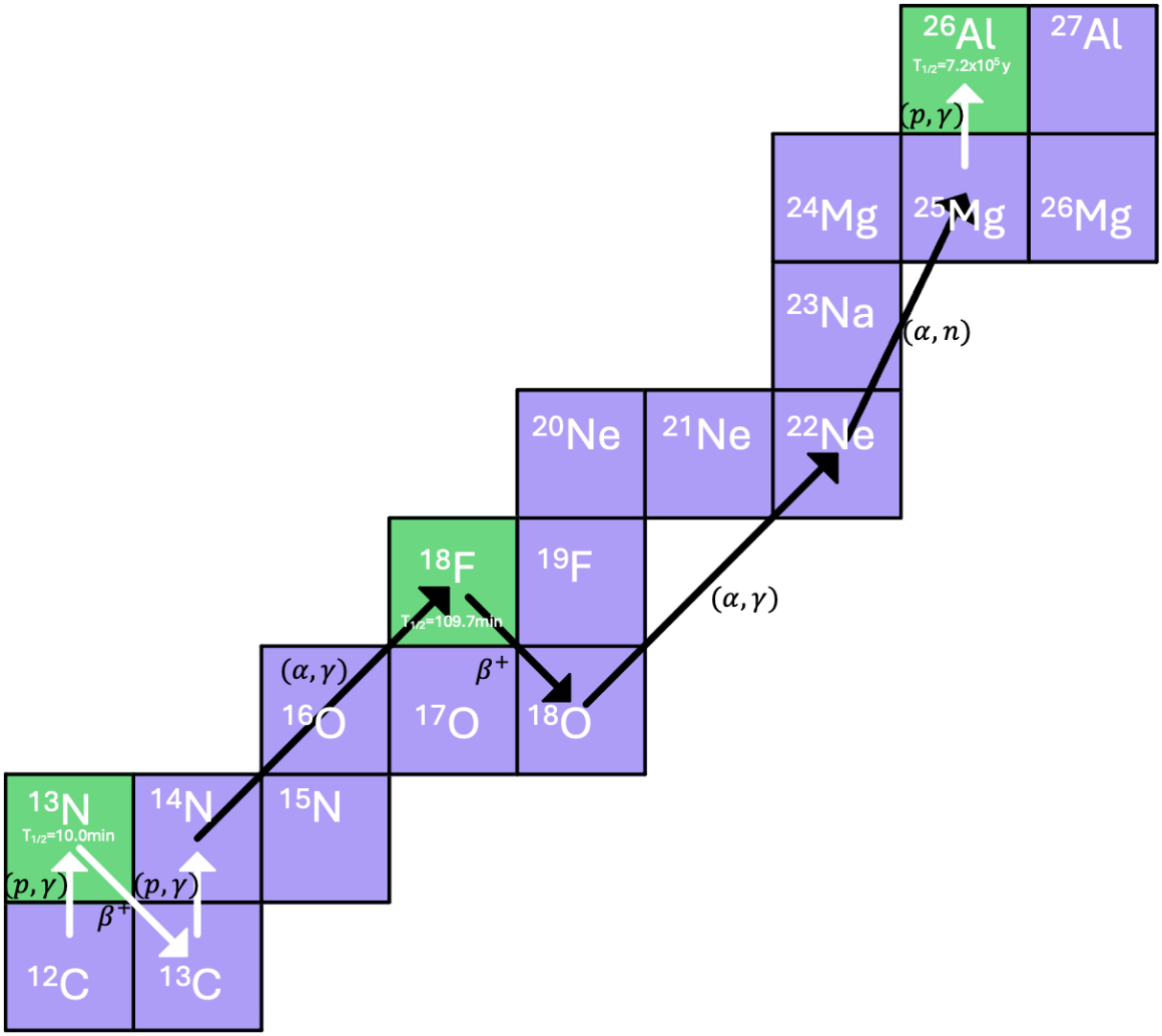

Figure 1.6: The chain of reactions which create ^{26}Al in the stellar model. Reactions which occur during hydrogen and helium burning are indicated by white and black arrows respectively (for details see text). Stable and unstable isotopes are shown in purple and green respectively. Half-lives were adopted from the NNDC NuDat 3 database and the ENSDF (National Nuclear Data Center, 2023; Tuli, 1996).

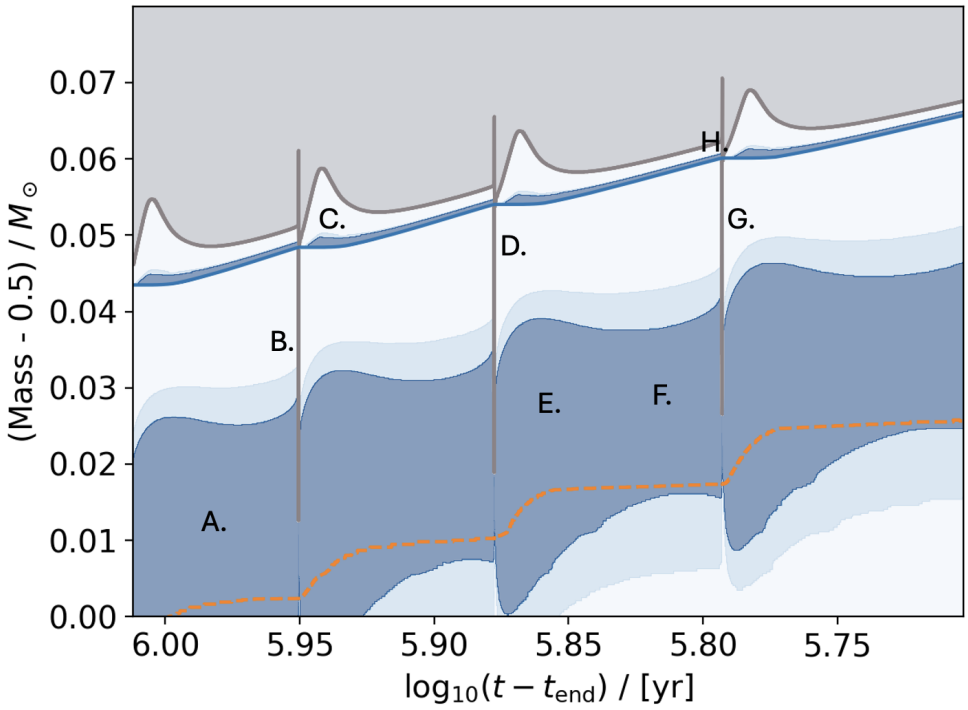

Figure 1.7: A Kippenhahn diagram of the TP-AGB with locations and stages of ^{26}Al creation labeled: A. The triple-α reaction creates ^{12}C. B. The contents of the He burning shell are mixed into the convective envelope. C. H burning turns ^{12}C into ^{14}N-rich ash. D. The ashes of H burning are mixed into the He burning shell. E. Two subsequent α captures on ^{14}N create ^{22}Ne. F. ^{22}Ne(α, n) generates ^{25}Mg. G. A thermal pulse introduces the ^{25}Mg to the H burning shell. H. ^{25}Mg captures a proton in the H burning shell to create ^{26}Al.

quantify how the depth and efficiency of mixing influence these isotopic trends. Particular emphasis is placed on the stabilizing role of the mean molecular-weight (μ) gradient, which may limit or suppress mixing, acting as a self-regulating mechanism within the stellar structure. This work also investigates how nuclear physics uncertainties—particularly in key proton-capture reaction rates—affect isotopic predictions and whether improved measurements at stellar energies could constrain the physical conditions under which CBP operates.

Chapter 2

Literature Review

2.1 Approaches to Simulating Isotopic Signatures of CBP

2.1.1 CBP Modeling and Comparison to Presolar Grain Data

Nollett et al. (2003) developed a parameterized model of CBP in low-mass AGB stars to account for the isotopic compositions of presolar oxides. We focus here on their treatment of Al and O isotopic ratios to explain Group 2 oxide data. In their framework, CBP is modeled as the slow circulation of material between the convective envelope and the radiative zone just above the hydrogen-burning shell. Material descends to a maximum temperature T_P, undergoes partial hydrogen burning, and is then transported back to the convective envelope.

The model is defined by two independent parameters: the maximum processing temperature T_P, which sets the depth of mixing and the degree of nuclear processing, and the mass circulation rate $\dot{M}$, which controls the efficiency of transport. Nuclear processing along the path is computed using a post-processing network that follows advective transport and reaction rates for key species such as ^{16}O, ^{17}O, ^{18}O, ^{26}Al, and ^{27}Al. A limitation of this approach is that CBP is imposed on a static stellar structure, neglecting feedback from CBP on stellar evolution and changes to the radiative zone over time. Because CBP is imposed in post-processing, the numerical model must assume that mixing does not alter the stellar structure. Nollett et al. (2003) adopted the conditions $\dot{M} < 10^{-4}$ $M_\odot yr^{-1}$ and $T_P < T_H$, where T_H is the temperature at the site of maximum energy generation within the H-burning shell, in order to maintain the stellar stratification. These limits, were intended only as preliminary estimates.

The results show that Group 2 oxide grains, with low $^{18}O/^{16}O$, elevated $^{17}O/^{16}O$, and enhanced $^{26}Al/^{27}Al$ ratios, can be reproduced by CBP in low-mass AGB stars when material is cycled to temperatures high enough to efficiently destroy ^{18}O but not so high as to drive ^{17}O fully to its equilibrium value. The production of ^{26}Al is found to be sensitive to T_P, with higher values increasing the $^{26}Al/^{27}Al$ ratio in the envelope. The oxygen isotopic ratios show the opposite behavior: once T_P exceeds a threshold for efficient processing, the final $^{18}O/^{16}O$ and $^{17}O/^{16}O$ values depend primarily on the mass circulation rate $\dot{M}$. Higher circulation rates drive stronger ^{18}O depletion and larger ^{17}O enhancements, while the precise value of T_P above the threshold has little additional effect.

Overall, the parameterized CBP framework provided a widely used tool for modeling extra mixing in evolved stars and demonstrated that, with suitable parameter choices, the isotopic signatures of Group 2 grains could be reproduced. However, the model introduced circulation in six discrete stages of TP-AGB evolution under fixed stellar structures, so feedback between CBP and stellar evolution, such as changes in luminosity, envelope mass, or dredge-up depth, was not captured. Effects of CBP during the RGB phase were also excluded from the model. Advances in stellar evolution codes, computing power, and nuclear reaction rate measurements over the past two decades now highlight the need for stellar models in which CBP is coupled to stellar structure and active across multiple evolutionary phases.

2.1.2 Magnetic Buoyancy Model of CBP and Comparison with Presolar Oxide Data

Palmerini et al. (2021) presented a parametrized model for CBP in low-mass AGB stars, with magnetic buoyancy as the driving mechanism for extra mixing between the convective envelope and the outer radiative layers above the hydrogen-burning shell. Stellar structures were computed with the `FUNS` code, while the `MAGIC` post-processing code to impose CBP. The `FUNS` code is a one-dimensional simulation of the evolution of low-mass AGB star (Straniero et al., 2006). `MAGIC` is a parameterized extra-mixing model applied to a fixed stellar structure, incorporating reaction rates updated beyond the NACRE compilation (Angulo et al., 1999; Palmerini et al., 2011). This treatment applies extra mixing to fixed stellar structures, without feedback on the star's thermal or structural evolution. Within this framework, magnetized structures ("magnetic bubbles") rise through the radiative zone, transporting material that has undergone partial hydrogen burning to the base of the convective envelope.

The upward velocity of these structures is described by a power-law dependence on radius:

$$v(r) = v(r_k) \left(\frac{r_k}{r}\right)^{k+1},$$

where r_k and $v(r_k)$ are the starting depth and velocity of mixing, respectively, and k is the power-law index related to the density stratification in the crossed region. The mixing rate is then estimated from the product of the envelope boundary velocity, the density of the radiative layer below the convective boundary, and two geometrical factors: the fractional surface coverage of magnetic bubbles (f_1) and their volumetric filling factor (f_2).

A simplifying assumption of this model is that the rising magnetic structures are thermally isolated: transported material is assumed to retain the temperature of its origin until it mixes into the envelope. In reality, conductive and radiative heat exchange would reduce buoyancy, slowing the ascent and lowering the effective circulation rate. By neglecting this exchange, the model likely overestimates mixing velocities and therefore the production of temperature-sensitive isotopes such as ^{26}Al (Denissenkov et al., 2009).

Palmerini et al. (2021) modeled 1.2 $M_\odot$ and 1.5 $M_\odot$ AGB stars with solar metallicity, using two sets of nuclear reaction rates that differ primarily in their adopted ^{17}O(p,α)^{14}N, ^{18}O(p,α)^{15}N, and ^{18}O(p,γ)^{19}F rates. Varying the parameter k adjusts the mixing depth, influencing the temperature experienced by the circulating material and thus the isotopic outcomes. Lower k values correspond to deeper mixing and higher temperatures, leading to more efficient ^{18}O destruction and greater ^{26}Al production, while the impact on the ^{17}O/^{16}O ratio is more complex due to its non-linear temperature dependence.

The models were compared with isotopic compositions measured in presolar oxide grains of groups 1 and 2. For the 1.2 $M_\odot$ model, magnetic mixing reproduced the majority of the oxygen isotopic ratios of Group 2 grains with small adjustments to k. However, the agreement with grains depended on the choice of ^{17}O(p,α)^{14}N, ^{18}O(p,α)^{15}N, and ^{18}O(p,γ)^{19}F reaction rates. The observed range of ^{26}Al/^{27}Al in Group 2 grains was reproduced by the 1.2 $M_\odot$ model for one set of reaction rates and the 1.5 $M_\odot$ for the other.

This work demonstrated that magnetic extra-mixing models, when tuned for depth and velocity, can reproduce key isotopic signatures in presolar oxide grains, and that the choice of nuclear reaction rates significantly impacts the range of grain compositions reproduced by the extra-mixing models (Palmerini et al., 2021).

2.1.3 Model of CBP Motivated by the Lithium-Rich RGB Tip Problem

The discovery of luminous RGB stars exhibiting anomalously high surface ^{7}Li abundances poses a long-standing problem for stellar evolution theory. Standard models predict that lithium should be severely depleted during the first dredge-up and further reduced by non-convective extra mixing during the RGB phase, making the occurrence of lithium-rich giants—especially near the RGB tip—unexpected. The RGB tip is the end of the RGB before core He-burning ignites, on HRD diagrams the RGB tip is the coolest and therefore rightmost point on the RGB. In Figure 1.1 the RGB tip is labeled as the helium flash. Observations indicating a luminosity-dependent increase in the fraction of lithium-rich giants suggest that an additional mixing process is activated or enhanced at higher luminosities (Denissenkov et al., 2024).

Denissenkov et al. (2024) proposed a physically motivated model for CBP to account for the lithium enrichment at the RGB tip. The model couples nuclear burning and non-convective mixing in a diffusive framework, with the mixing coefficient $D_{\rm mix}$ allowed to scale with stellar luminosity. This parameterization captures the empirical trend that extra mixing appears more efficient in more luminous RGB stars. The physical driver is proposed to be magneto-thermohaline instabilities, which could operate in the radiative region between the hydrogen-burning shell and the convective envelope, enabling material to cycle down to temperatures sufficient to produce ^{7}Li.

In Denissenkov et al. (2024), the depth of extra mixing was limited by the stabilizing effect of the mean molecular weight (μ) gradient left behind by the first dredge-up. Mixing was not allowed to penetrate into regions where μ increased beyond its convective envelope level, reflecting the physical inhibition of motion by buoyancy forces in compositionally stratified layers. This prescription ensures that, even in the presence of a luminosity-enhanced diffusion coefficient, mixing remains confined to regions accessible within the constraints imposed by the internal μ-profile.

The mixing coefficient is expressed as:

$$D_{\rm mix} \propto L^{\alpha}, \tag{2.1}$$

where L is the stellar luminosity and α is a free parameter tuned to reproduce the observed lithium abundances and their distribution with luminosity. Model calculations show that such luminosity-dependent CBP can reproduce both, the high lithium abundances and their

concentration near the RGB tip, while remaining consistent with constraints from other surface abundance ratios.

2.2 Spectroscopic Measurements of C and O Isotopic Ratios in Mira Variables

Mira variables are evolved, pulsating AGB stars with large-amplitude radial pulsations and long periods. Their extended, cool atmospheres produce strong molecular absorption features, making them well suited for high-resolution spectroscopic measurements of carbon and oxygen isotopic ratios.Our simulated surface isotopic abundances were compared to presolar grains and spectroscopic measurements by (Hinkle et al., 2016). They analyzed high-resolution Fourier Transform Spectra (FTS) from the Kitt Peak National Observatory 4-m Mayall telescope in Arizona, covering the near-infrared range from 1.5–2.5 μm. Within this band, they measured first- and second-overtone vibration–rotation transitions of carbon monoxide (CO), in which molecular bonds simultaneously stretch (vibrate) and rotate. These lines are sensitive to isotopic substitution in either carbon or oxygen and thus provide a precise probe of $^{12}C/^{13}C$, $^{16}O/^{17}O$, and $^{16}O/^{18}O$ ratios in stellar atmospheres.

Laboratory line lists were generated for expected isotopic variations within the CO molecule under local thermodynamic equilibrium conditions (2000–4000 K). Line positions were aligned using cross-correlation with strong $^{12}C^{16}O$ features. Only minimally blended lines were selected by comparing multiple stellar spectra, ensuring reliable isotopologue identification.

Isotopic ratios were derived using curve-of-growth (CoG) analysis, which describes how the equivalent width of a spectral line changes as the abundance of the absorbing species changes and as physical conditions in the stellar atmosphere vary over time. Weak lines increase roughly linearly with abundance, while stronger lines become saturated and grow more slowly. Equivalent widths of selected isotopic CO lines were measured and compared against those of the dominant $^{12}C^{16}O$ transitions. The excitation temperature was estimated from the rich set of $^{12}C^{16}O$ lines and applied consistently across isotopes at each observed epoch, assuming a common atmospheric structure. Isotopic ratios were then obtained from the relative horizontal shifts between the CoGs of different isotopes, which reflect differences in their abundances.

Scatter in equivalent widths, continuum placement, and line blending contributed to measurement uncertainties. The small number of usable $^{12}C^{18}O$ lines (sometimes only one

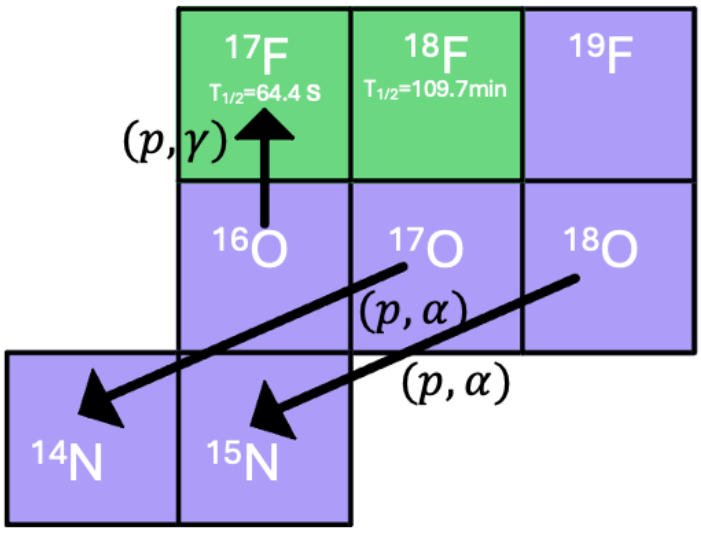

Figure 2.1: The three reactions with the greatest effect on the simulated surface oxygen isotopic ratios. Stable and unstable isotopes are shown in purple and green respectively. Half-lives were adopted from the NNDC NuDat 3 database and the ENSDF (National Nuclear Data Center, 2023; Tuli, 1996).

per star) made $^{16}O/^{18}O$ the least certain ratio, whereas $^{12}C/^{13}C$ and $^{16}O/^{17}O$ were better constrained. Variations with pulsation phase were tested using multiple epochs for several stars; results indicated only weak phase dependence for carbon ratios but larger scatter for oxygen ratios.

For most of the observed stars, $^{12}C/^{13}C$ ratios were found to be $\sim$ 10–20, consistent with low-mass ($< 2M_{\odot}$) progenitors that had experienced first dredge-up and possible RGB extra mixing. A wide spread in $^{16}O/^{17}O$ ratios (200–2700) was observed, in line with predictions for 1–2 $M_{\odot}$ AGB stars. $^{16}O/^{18}O$ ratios were systematically lower than those in Group 1 presolar oxide grains, likely reflecting galactic chemical evolution (progressive ISM enrichment in ^{18}O). A small subset of stars showed compositions resembling Group 2 grains, possibly indicating extra mixing (Hinkle et al., 2016).

2.3 Literature Review of Key Reactions

Figure 2.1 shows the three reactions with the greatest effect on the simulated surface oxygen isotopic ratios. The following section describes the previous measurements and calculations of the three reaction rates.

2.3.1 $^{17}\mathbf{O}(p,\alpha)^{14}\mathbf{N}$

The ^{17}O(p,α)^{14}N reaction is a key component of H-burning nucleosynthesis in stellar environments such as red giant, AGB, and massive stars. It governs the destruction of ^{17}O and competes with the ^{17}O(p,γ)^{18}F channel, influencing the abundance of the short-lived radionuclide ^{18}F ($T_{1/2} = 109.7$ min) which is of interest for γ-ray astronomy (National Nuclear Data Center, 2023; Tuli, 1996). Accurately determining its rate is critical for models of nucleosynthesis and isotopic ratio predictions in stellar atmospheres and presolar grains (Lugaro et al., 2017; Sergi et al., 2020; Rapagnani et al., 2025).

Trojan Horse Method

Direct measurements of the ^{17}O(p,α)^{14}N cross section at astrophysically relevant energies are hindered by the Coulomb barrier and electron screening, leading to large uncertainties, particularly for the 65 keV resonance that dominates the stellar rate at $T \approx 0.02$–0.07 GK.

To circumvent these limitations, the Trojan Horse Method (THM) was employed. This indirect technique reconstructs the low-energy binary reaction from a three-body reaction under quasi-free kinematics. Specifically, the reaction ^{2}H(^{17}O,α^{14}N)n was used, with the deuteron acting as a "Trojan horse" to deliver the proton to ^{17}O without Coulomb suppression or electron screening. The experiments were performed at Istituto Nazionale di Fisica Nucleare – Laboratori Nazionali del Sud (INFN-LNS) and cross-validated with experiments on neutron induced reactions at the Nuclear Structure Lab at Notre Dame (Sergi et al., 2020). Coincidence detection of α and ^{14}N particles was conducted using position-sensitive silicon detectors. Kinematic selections and comparison with theoretical neutron momentum distributions confirmed the dominance of the quasi-free mechanism.

Two resonances were identified in the THM data: the well-known 183 keV resonance and the low-energy 65 keV resonance of primary astrophysical importance. The resonance strength $\omega\gamma$ of the 65 keV state was determined by normalizing to the known 183 keV resonance. This approach cancels model dependencies by taking ratios of quantities calculated for nearby resonances, significantly reducing systematic uncertainties.

The resulting resonance strength was:

$$(\omega\gamma)_{65\,\mathrm{keV}} = (3.42 \pm 0.60) \times 10^{-9}\ \mathrm{eV},$$

which is in good agreement with earlier compilations (e.g., NACRE) (Angulo et al., 1999), though lower than the recent LUNA result of $(10.0 \pm 1.6) \times 10^{-9}$ eV (Sergi et al., 2015). LUNA

(Laboratory for Underground Nuclear Astrophysics) is a low-background accelerator facility located deep underground at the Gran Sasso National Laboratory in Italy. Its underground environment strongly suppresses cosmic-ray–induced backgrounds, enabling high-precision direct measurements of low-energy nuclear reaction cross sections at astrophysical energies (Gesuè et al., 2024).

Low interference between resonances was observed, therefore the accepted standard reaction rate from (Iliadis et al., 2010) was revised by updating the contribution from the 65 keV resonance. This revised rate shows an decrease of ∼30% in the temperature range relevant for hydrogen burning in RGB and AGB stars ($T = 0.02$–0.07 GK) compared to (Iliadis et al., 2010).

The application of THM to the ^{17}O(p,α)^{14}N reaction allows precise extraction of the 65 keV resonance strength at stellar energies, significantly reducing uncertainties associated with extrapolations and electron screening. These results offer an important benchmark for nucleosynthesis models. The observed discrepancies with direct measurements, such as those by LUNA, highlight the need for continued investigation into systematic effects and the interplay between direct and indirect techniques (Sergi et al., 2020).

R-Matrix and Monte Carlo Method

The recent high-precision study by the LUNA Collaboration (Rapagnani et al., 2025) employed a comprehensive R-matrix analysis coupled with a Monte Carlo treatment of experimental uncertainties to revise the stellar rate of the ^{17}O(p,α)^{14}N reaction. They incorporated all available experimental resonance data—particularly new direct measurements of the 64.5 keV resonance strength and branching ratios.

The R-matrix formalism provides a framework for describing nuclear reactions that proceed through resonant compound-nucleus states. In this approach, the configuration space is divided into an internal region, where nuclear interactions dominate and wavefunctions are expanded in terms of discrete resonance states, and an external region, governed solely by Coulomb forces. Boundary conditions at the channel radius connect the two regions, allowing observed cross sections to be expressed in terms of resonance parameters (level energies, partial widths, and channel radii). By fitting these parameters to experimental data, the R-matrix method yields a physically consistent description of multiple reaction channels sharing the same compound nucleus (Descouvemont and Baye, 2010).

At $T < 0.1$ GK, the temperature range relevant for hydrostatic hydrogen burning, the median ^{17}O(p,α)^{14}N rate is up to twice that of the JINA Reaclib evaluation, with 2σ uncer-

tainties spanning a factor of up to ∼3 (Cyburt et al., 2010; Rapagnani et al., 2025).

The incorporation of updated 64.5 keV resonance strengths measured by the LUNA Collaboration (Bruno et al., 2016; Gesuè et al., 2024) increases the ^{17}O destruction rate relative to older compilations, leading to systematically higher predicted ^{16}O/^{17}O ratios in standard stellar evolution models following the first dredge-up and during subsequent RGB and AGB evolution. The degree to which these enhanced ratios are reflected at the stellar surface depends on the presence and efficiency of extra mixing processes. The nuclear-physics uncertainty in predicted oxygen isotopic ratios was reduced to within roughly 10% under typical RGB and AGB conditions, strengthening the reliability of isotopic constraints on deep mixing processes in evolved stars. Continued direct measurements of low-energy resonances, combined with R-matrix analyses of CNO-cycle reactions, will further refine these rates and help disentangle the relative roles of nuclear physics and mixing in shaping observed isotopic signatures (Lugaro et al., 2017; Rapagnani et al., 2025).

2.3.2 $^{18}\mathbf{O}(p,\alpha)^{15}\mathbf{N}$

The ^{18}O$(p,\alpha)^{15}$N reaction plays a central role in the nucleosynthesis of oxygen isotopes in stellar hydrogen-burning environments. It is an important destruction pathway for ^{18}O, influencing the ^{18}O/^{16}O and ^{17}O/^{16}O ratios in evolved stars and presolar grains, and influencing the ^{15}N and ^{19}F abundances. Accurate knowledge of its rate is essential for modeling cool bottom processing and other extra mixing processes in AGB stars.

Previous compilations of the ^{18}O$(p,\alpha)^{15}$N rate have relied on experimental data that carried significant uncertainties, particularly in the low-energy range relevant to stellar interiors (T=0.01-1.00 GK). In this regime, the cross section is dominated by resonances with uncertain energies, widths and strengths.

Li et al. (2024) carried out a comprehensive multichannel R-matrix analysis that incorporated all available experimental data from previous studies, including the ^{18}O(p,α)^{15}N, ^{18}O(p,γ)^{19}F, and ^{15}N(α,α')^{15}N reactions. Datasets were drawn from (Mak et al., 1978; Lorenz-Wirzba et al., 1979; Christensen et al., 1990; Bruno et al., 2019; La Cognata et al., 2019), among others. This work represents the first global analysis to simultaneously constrain these coupled reaction channels, using elastic α–scattering data on ^{15}N as an additional probe of the resonance structure in ^{19}F (Li et al., 2024).

In the analysis of Li et al. (2024), the fitted resonance parameters were used to compute updated astrophysical S-factors and thermonuclear reaction rates for ^{18}O(p,α)^{15}N, with uncertainties estimated through a Monte Carlo propagation of the covariance matrix of the fit-

ted parameters. This global re-evaluation refines the key reaction rates relevant to hydrogen-burning nucleosynthesis in Red Giant and AGB stars without introducing new experimental data.

The updated rate has direct consequences for modeling ^{18}O destruction in extra-mixing scenarios, leading to more reliable predictions of oxygen isotope ratios in stellar ejecta and presolar grains (Li et al., 2024). The small uncertainty for $T < 0.1$ GK reported by Li et al. (2024) is in line with the uncertainty ranges found by Bruno et al. (2019) and Cognata et al. (2010).

2.3.3 $^{16}\mathbf{O}(p,\gamma)^{17}\mathbf{F}$

The ^{16}O(p,γ)^{17}F reaction is a key component of the CNO cycle in H-burning stellar environments. It produces ^{17}F, which subsequently β^+ decays to ^{17}O. The reaction rate influences isotopic abundances in low- and intermediate-mass stars, affects the predicted ^{16}O/^{17}O ratios observed in presolar grains and evolved stars, and plays a secondary role in neutrino production in solar models (Iliadis et al., 2022).

At astrophysical temperatures (e.g., $T = 0.01$–0.1 GK), the ^{16}O(p,γ)^{17}F reaction proceeds at center-of-mass energies well below 1 MeV. In this regime, the cross section is dominated by non-resonant direct capture into bound states of ^{17}F. The energy dependence of this process is characterized by the astrophysical S-factor, $S(E)$, which removes the Coulomb suppression from the cross section and enables extrapolation to stellar energies.

Accurate calculation of $S(E)$ in this low-energy region is essential for constraining models of oxygen isotopic evolution in stellar envelopes, since the ^{16}O(p,γ)^{17}F reaction competes with ^{17}O destruction channels to set the equilibrium ^{16}O/^{17}O ratio. However, direct measurements at these energies are technically challenging: the cross section falls to the order of 10^{-17} barns, demanding high beam currents, long integration times, and extremely low background levels (Kunz et al., 2002). Additionally, uncertainties in energy calibration, detector efficiencies, and target composition complicate the extraction of reliable S-factors.

Iliadis et al. (2022) performed a new evaluation of the ^{16}O(p,γ)^{17}F S-factor combining multiple high-resolution direct measurements. The dominant capture transitions are to the ground state ($5/2^+$) and first excited state ($1/2^+$) of ^{17}F. A schematic level scheme for ^{17}F is shown in Figure 2.2.

The total S-factor can be approximated as the sum of the contributions from these two branches:

$$S_{\rm tot}(E) = S_{\rm g.s.}(E) + S_{1/2^+}(E).$$

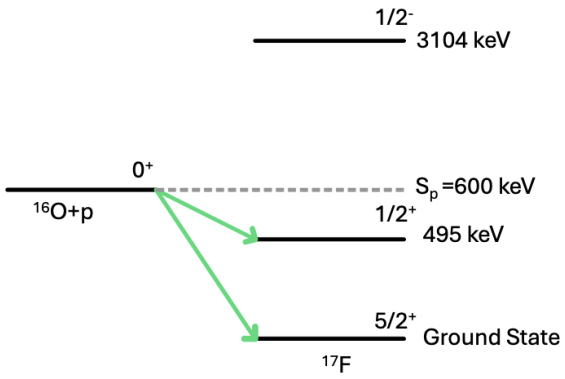

Figure 2.2: Level scheme of ^{17}F showing the ground state and first excited state primarily accessed by the ^{16}O(p,γ) reaction and the next lowest energy excited state (Tilley et al., 1993).

(Iliadis et al., 2022) reanalyzed existing experimental data for the ^{16}O(p,γ)^{17}F reaction using a Bayesian statistical framework. The Bayesian framework combines prior information about nuclear model parameters with experimental data to produce probability distributions that describe their most likely values and uncertainties. This approach treats statistical and systematic errors consistently and propagates them through to the final reaction rate. The data spans center of mass energies between approximately 200 keV and 2.5 MeV, covering the range most relevant for extrapolation into the range of astrophysical interest ($T < 0.1$ GK). They combined results from several previous measurements, accounting for both statistical and systematic uncertainties, to produce a consistent evaluation of the astrophysical S-factor.

A single-particle model was used to describe the capture process, in which the asymptotic normalization coefficients (ANCs) determine the absolute scale of the calculated S-factor at low energies. The ANC quantifies the amplitude of the tail of the nuclear overlap function in the asymptotic region, effectively describing how strongly the final bound state is populated in the external (non-resonant) capture process. This approach provides a unified treatment of experimental data and quantifies uncertainties in the extrapolation toward stellar energies.

At zero center-of-mass energy, corresponding to the extrapolated limit relevant for hydrogen burning in stellar interiors, the authors find:

$$S_{\rm tot}(0) = 0.0109(4)\,\text{MeV b},$$

representing the combined ground- and first-excited-state contributions. This extrapolated value defines the astrophysical S-factor at $E = 0$, where the influence of the Coulomb barrier has been removed and the cross section can be smoothly extended to stellar energies.

From the derived S-factor, a new thermonuclear reaction rate for ^{16}O(p,γ)^{17}F across the temperature range relevant to stellar hydrogen burning was computed. The resulting rate is tightly constrained, with a median uncertainty of about 3–4% over the range $T = 0.02$–0.2 GK—a substantial improvement over previous compilations such as NACRE and STARLIB (Angulo et al., 1999; Iliadis et al., 2010). At typical hydrogen-burning temperatures, the new rate agrees with earlier evaluations within their uncertainties but offers greater precision and a more robust quantification of confidence intervals, making it well suited for use in stellar evolution and nucleosynthesis models (Iliadis et al., 2022).

Chapter 3

Methods

3.1 Stellar Model

A stellar model for a 1.2 $M_\odot$ star with solar metallicity from Asplund et al. (2009) scaled to [Fe/H] = −0.3 was simulated with MESA revision 7624 (Paxton et al., 2010, 2013). The input physics follow the assumptions made in Denissenkov et al. (2017) and Denissenkov et al. (2024), in which the same MESA revision was used to model stars of the same mass and metallicity, with selected inputs varied to match prior simulations and observational constraints (VandenBerg et al., 2016). This work adopts the same treatment of MLT, EOS, and opacities as those earlier studies, ensuring consistency with previous stellar models.

The overshooting, stellar atmosphere, and mass-loss schemes replicate the assumptions of NuGrid Data Set 1, which provides a consistent benchmark of stellar evolution and nucleosynthesis models across a broad mass range (Pignatari et al., 2016). A simple photosphere stellar atmosphere was used, with the outer boundary placed at optical depth ~ 1 under hydrostatic equilibrium and a gray temperature–optical-depth relation, in which the opacity is assumed to be independent of wavelength. The Reimers and Blocker mass-loss schemes were used to simulate mass loss during the RGB and AGB phases, respectively. The mass loss efficiencies of $\eta_R = 0.5$ and $\eta_B = 0.01$ from NuGrid data set I were used (see Section 1.4.5)(Pignatari et al., 2016).

The nuclear reaction network used in the MESA calculations includes the pp chains (branches I–III), the CNO cycles (I–IV), helium and carbon burning, as well as the neon–sodium and magnesium–aluminum cycles (Denissenkov et al., 2017). Reaction rates were adopted from the JINA Reaclib database (Cyburt et al., 2010).

The combination of mixing and mass-loss prescriptions prevents the star from becoming

carbon-rich. Instead, mass loss, CBP, and envelope mixing result in the star entering the post-AGB phase with a nitrogen-rich surface, halting the formation of oxygen-rich presolar grains after most of the envelope mass has been lost.

3.2 Secular Diffusive Parameterized Model of CBP

CBP was added to the stellar model using a parameterized diffusion model extending below the convective envelope during the RGB and interpulse phases of the thermally pulsing AGB. The extent of mixing is constrained by the mean molecular weight (μ) gradient, which produces a stabilizing buoyancy (Archimedes) force. This force arises because denser, higher-μ material lies below lighter material, so any downward motion of fluid parcels is opposed by a restoring buoyant force. As a result, the extra mixing cannot penetrate into regions where the μ gradient is strong. This stabilizing role of the μ-gradient is formalized in the Ledoux criterion for convective stability in regions with heterogeneous chemical composition (see Section 1.4.6)(Kippenhahn et al., 2012). The mean molecular weight was calculated using all available isotopes in the reaction network at each time step changing the mixing depth as the star evolves.

A parameter, μ_{factor}, was introduced to control the extent of extra mixing relative to the mean molecular weight in the convective envelope, μ_{CE}. Mixing is allowed until the local mean molecular weight exceeds μ_{CE} by a factor of μ_{factor}. For convenience, this excess is expressed as

$$\delta\mu = (\mu_{\text{factor}} - 1) \times 10^5, \tag{3.1}$$

which scales relative to the increase above the envelope value. $\mu_{\text{factor}} > 1$ or $\delta\mu > 0$ corresponds to mixing that penetrates into regions where the mean molecular weight is greater than in the convective envelope.

The diffusion coefficient for extra mixing (D_{mix}) was set to a sub-unity fraction (η_D) of thermal diffusivity (K), preventing the mixing scheme from modifying the underlying stellar stratification (Denissenkov et al., 2024).

The depth and speed of the extra mixing were varied to match the isotopic ratios observed in grains. Figure 3.1 shows that an increase in mean molecular weight limits the depth of the extra mixing and the diffusion coefficient of the extra mixing following the thermal diffusivity as it extends beyond the convective envelope. The depth and efficiency of the extra mixing were varied to reproduce isotopic ratios observed in presolar grains.

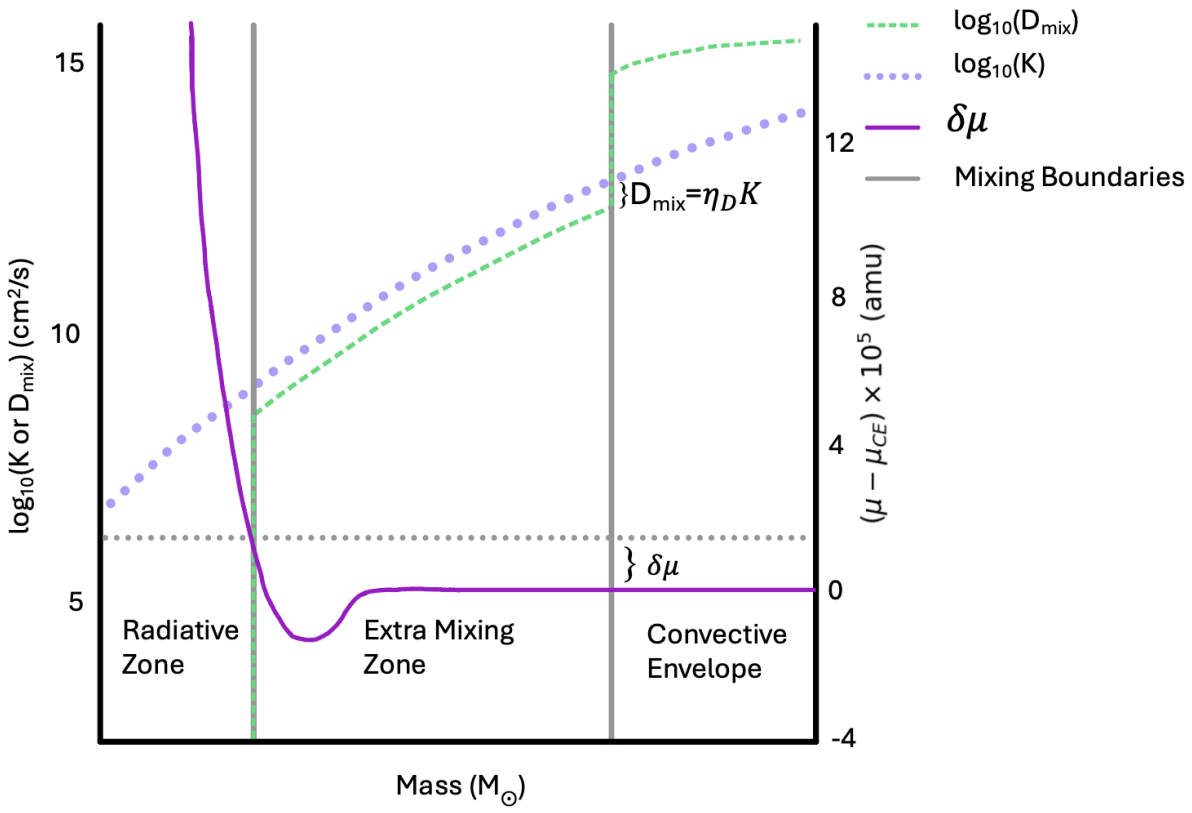

Figure 3.1: Schematic of the CBP parameterization, indicating the μ-gradient that halts mixing and the diffusion coefficient defined in proportion to the thermal diffusivity.

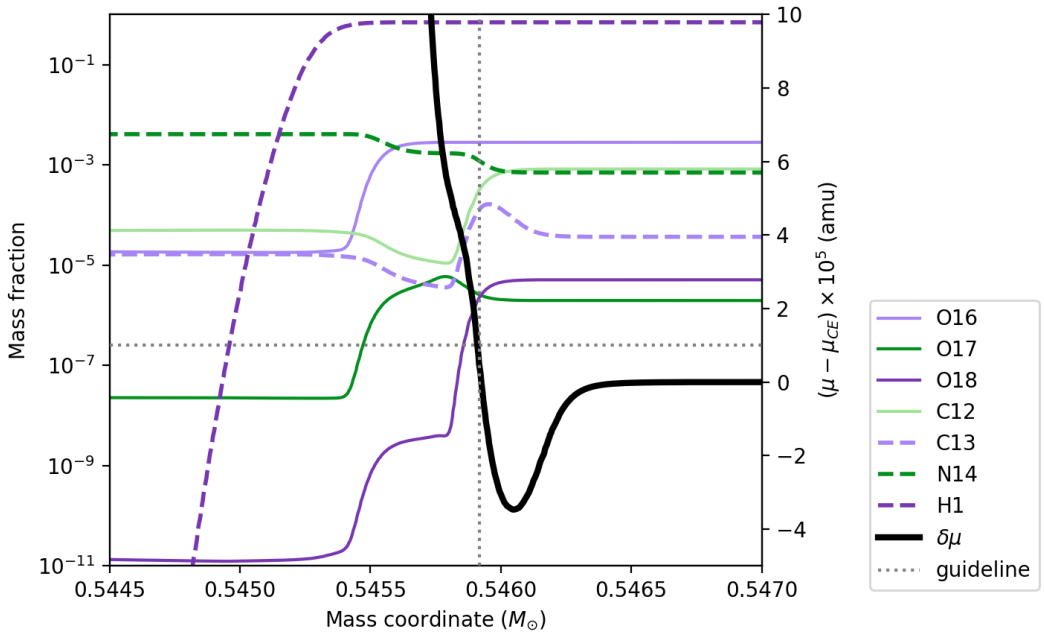

Figure 3.2: Abundance profiles from an early interpulse period of the stellar model without CBP, focusing on the region around the μ-gradient at the top of the hydrogen-burning shell. The secondary axis on the right shows the mean molecular weight gradient, with grey dotted guidelines showing a mixing depth of CBP and the corresponding $\delta\mu$

Extra mixing redistributes features in the radial isotopic profiles created by the hydrogen burning shell and thermal pulses, diffusing these composition changes throughout the convective envelope and ultimately to the stellar surface. Figure 3.2 shows that the mean molecular weight increases toward the stellar interior at the very top of the hydrogen burning shell. The increase in μ coincides with an increase in the abundance profile of ^{17}O, allowing CBP to enhance the surface ^{17}O/^{16}O ratio. At the same depth, the ^{18}O abundance decreases, allowing CBP to deplete the surface ^{18}O/^{16}O ratio. Introducing CBP that extends down to the increase in μ couples the outer convective envelope to the upper edge of the hydrogen-burning shell. This circulation mixes material that has undergone partial nuclear processing back to the surface, redistributing the isotopic gradients and altering the surface ^{17}O/^{16}O and ^{18}O/^{16}O ratios.

Extra mixing was included during the RGB phase, beginning at the discontinuity left by the retreating convective envelope after the FDU (Denissenkov et al., 2024), until the RGB tip, identified by the helium luminosity reaching 10^3 L$_\odot$. No extra mixing was applied between the first helium shell flash and the onset of thermal pulses during the AGB phase

because of the distance between the convective envelope and the hydrogen burning shell. Extra mixing was reintroduced during the first interpulse period of the TP-AGB phase as identified by model number. The luminosity and timing thresholds halt and restart mixing as illustrated in Figure 3.3. During the TP-AGB, mixing was excluded during the thermal pulses themselves, when the pulse-driven convective zone extends into the region of extra mixing and the hydrogen-burning shell is disrupted. Extra mixing was included only during the interpulse periods, and was switched off whenever the helium luminosity exceeded the hydrogen luminosity.

3.3 Nuclear Physics Impact Study

The effect of nuclear physics uncertainties on the stellar model was investigated with a one-zone Monte Carlo impact study at a fixed temperature and density, designed to approximate conditions during the RGB and AGB phases of the MESA model. Each one-zone model represents the deepest point reached by extra mixing, where the high temperatures steeply increase reaction rates, making this region the primary site of nucleosynthesis. The temperature and density were sampled just before entry into the radiative zone identified by a drop in the diffusion coefficient.

The evolution times of the one-zone simulations were varied to reproduce the oxygen isotopic ratios simulated with MESA during the late RGB phase and the TP-AGB phase. Initial compositions were taken from the convective envelope of the stellar model during the late RGB and early TP-AGB phases to simulate envelope material that is introduced to the top of the hydrogen burning shell by CBP.

The reaction network included 162 isotopes from neutrons and protons up to ^{61}Fe, and was validated against a larger network of 1105 isotopes extending to ^{210}Bi. Isotopes heavier than iron were excluded because the low neutron densities in these environments prevent significant s-, i-, or r-process nucleosynthesis. Only isotopes within a few steps of stability were included, consistent with hydrogen-burning conditions. Due to the proton-rich hydrogen burning environment, with low α and neutron densities only (p, γ), (p, α), and (p, n) reaction rates were varied. Reaction rates were varied by factors of 1.5, providing modest deviations from the expected values that maintain approximate linearity in the model response.

The reactions with the largest influence on the ^{17}O/^{16}O and ^{18}O/^{16}O ratios were identified using Pearson correlation coefficients. The effect of nuclear physics uncertainties on the ^{26}Al/^{27}Al ratio was not examined, since most ^{26}Al is produced before CBP is triggered, under conditions not reproduced by the one-zone model. The Pearson equation was calculated

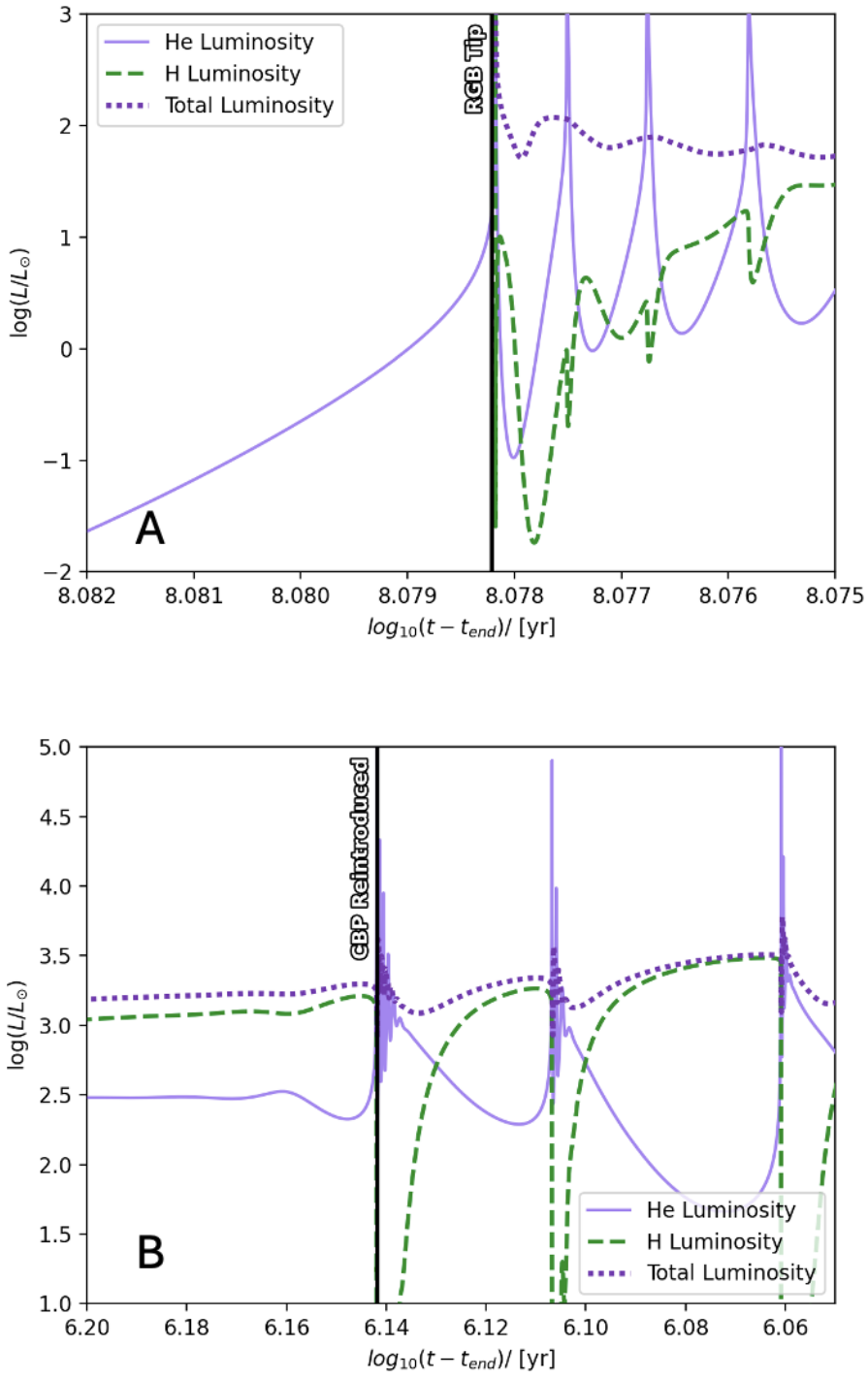

Figure 3.3: The simulated luminosity at the end of the RGB phase in panel A and beginning of the AGB phase in panel B with key stages indicated.

using:

$$r_p = \frac{\sum_{i=1}^{n} \left(f_i^{rr} - \bar{f}^{rr}\right)\left(O_i^{\text{ratio}} - \bar{O}^{\text{ratio}}\right)}{\sqrt{\sum_{i=1}^{n} \left(f_i^{rr} - \bar{f}^{rr}\right)^2}\sqrt{\sum_{i=1}^{n} \left(O_i^{\text{ratio}} - \bar{O}^{\text{ratio}}\right)^2}}, \tag{3.2}$$

where r_p is the Pearson coefficient, O^{ratio} is the oxygen isotopic ratio of interest, $\bar{O}^{\text{ratio}}$ is the mean of O^{ratio}, f^{rr} is the MC multiplier on a reaction rate, and $\bar{f}^{rr}$ is the mean of f^{rr}.

Reactions with Pearson coefficients $|r_p| > 0.15$ relative to the $^{18}\text{O}/^{16}\text{O}$ and $^{17}\text{O}/^{16}\text{O}$ ratios were considered impactful, following the threshold adopted in (Denissenkov et al., 2017). The identification of key reactions proved to be robust against the exact choice of this limit. To further assess sensitivity to reaction rate uncertainties, the slope of a linear fit between the one-zone oxygen isotopic ratio and the reaction rate multiplication factor was also considered. The linear fit takes the form:

$$O^{ratio} = mf^{rr} + b, \tag{3.3}$$

where m is the slope of the fit and b is the intercept. This analysis was restricted to reactions with sufficiently high Pearson coefficients. A literature review was then conducted to compile state-of-the-art values and constraints for the reactions flagged by their Pearson coefficients and slopes. MESA simulations with these updated reaction rates, and their upper and lower bounds, were performed to evaluate the impact of nuclear physics uncertainties across the full stellar evolution.

Chapter 4

Results

4.1 Effect of Extra Mixing on Oxygen Isotopic Ratios

The evolution of a 1.2 $M_\odot$ star with $[Fe/H] = -0.3$ predicted by `MESA` with CBP included is represented in Figures 4.1 and 4.2 with key points in the evolution highlighted.

The secular diffusive parameterized model of CBP, with input parameters $\delta\mu = 1$ and $\epsilon_D = 0.2$, generated surface O isotopic abundances that match the Group 2 grain data. As shown in Figure 4.3, this CBP model generates surface isotopic abundance ratios during the TP-AGB period, which is O-rich and experiences significant mass loss, that overlap well with the Group 2 grain data. The model with CBP included demonstrates the depletion of the $^{18}O/^{16}O$ ratio characteristic of Group 2 oxide grains due to depletion during the RGB and AGB phases. The $^{17}O/^{16}O$ ratio is enriched throughout the RGB phase and to a lesser extent the AGB phase, until third dredge up, in the model with CBP included. Figure 4.3 also shows that without CBP the O isotopic abundances remain at their bump luminosity levels during the RGB phase and exhibit minimal change on the AGB. The surface O isotopic ratios of the model without CBP fail to reach those observed in Group 2 oxide grains and instead reproduce the abundance ratios characteristic of Group 1 oxide grains. However, the 1.2 $M_\odot$ model does not attain the highest $^{17}O/^{16}O$ ratios observed among Group 1 grains, which are understood to originate from more massive ($\sim$2.0–2.5 $M_\odot$) RGB and AGB stars that experience deeper first dredge-up (Boothroyd and Sackmann, 1999).

The surface $^{17}O/^{16}O$ ratio is enhanced by CBP because the μ-gradient that limits its depth lies at the top of the H-burning shell, where a bump in the radial abundance profile of ^{17}O occurs. CBP depletes the $^{18}O/^{16}O$ ratio because it reaches a decline in the radial abundance profile of ^{18}O level. The aforementioned features in the radial isotopic abundance

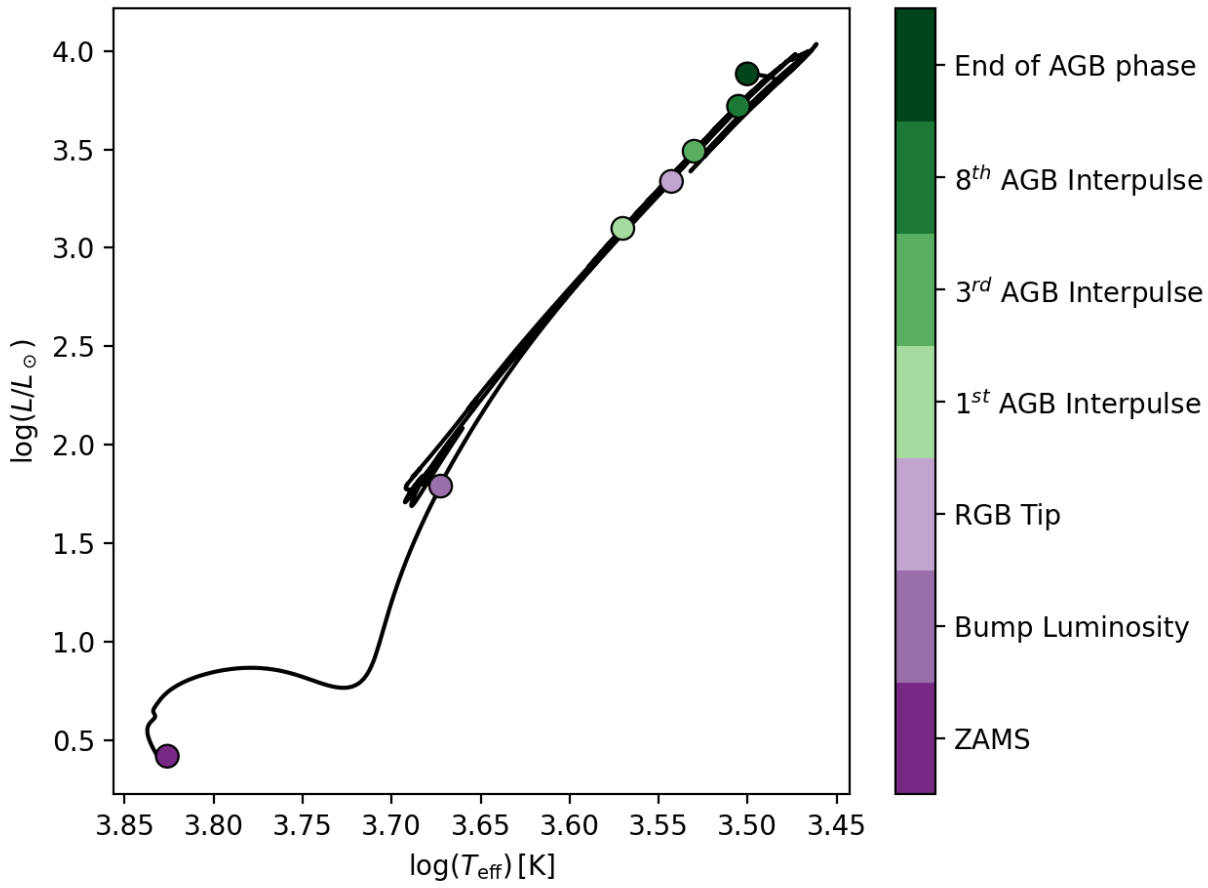

Figure 4.1: HRD of the stellar model of a 1.2 $M_\odot$ star with $[Fe/H] = -0.3$ with CBP included. Important evolutionary stages are marked.

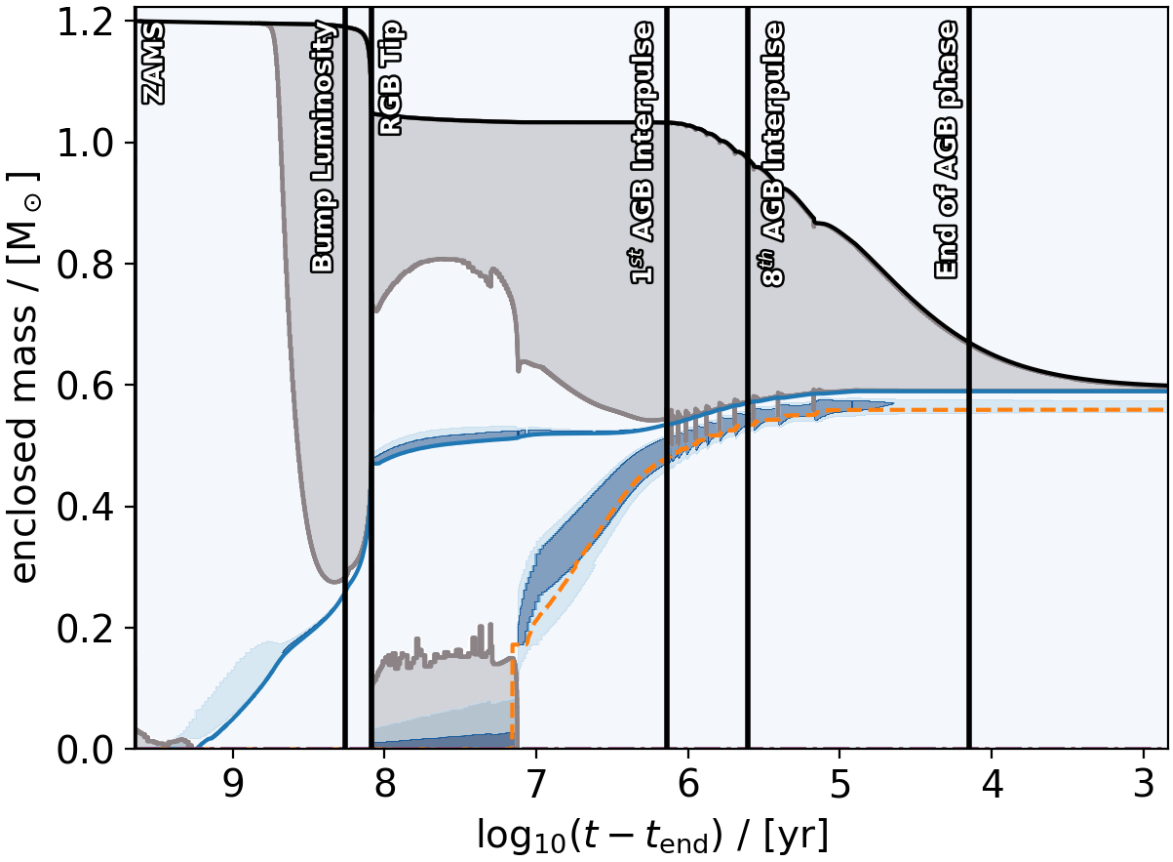

Figure 4.2: Kippenhahn diagram of the of the stellar model of a 1.2 $M_\odot$ star with $[Fe/H] = -0.3$ with CBP included. Lines mark the same evolutionary stages shown in Figure 4.1. The surface of the star (the outer edge of the convective envelope) is marked by a solid black line, the H-free core is marked by a solid blue line, the He-free core is marked by an orange dashed line, convective mixing is marked by grey shading, and energy generation is marked by dark blue shading.

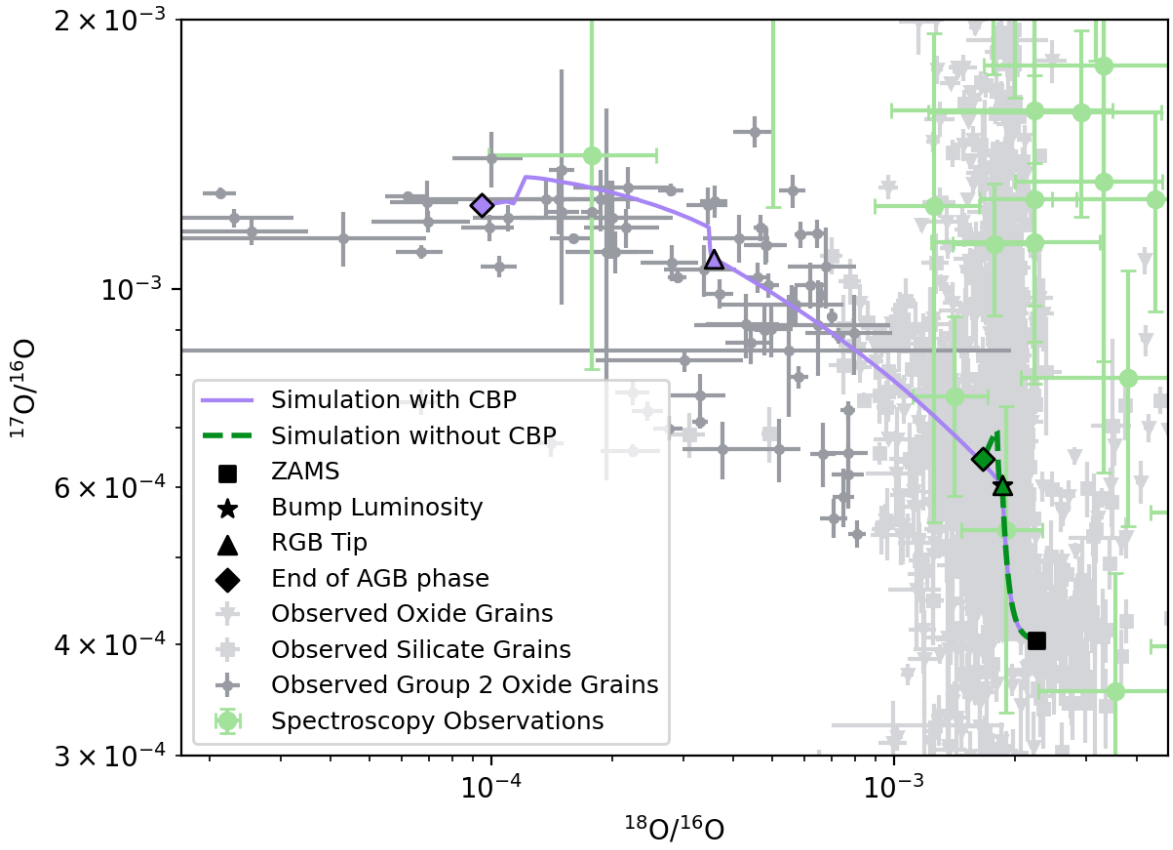

Figure 4.3: Plot of observed O isotopic ratios for Group 2 oxide grains (Hynes and Gyngard, 2009) and spectroscopic observations (Hinkle et al., 2016) from low mass AGB stars compared to simulated surface O abundances with and without extra mixing. The model of CBP uses input parameters $\mu_{inc} = 1$ and $\eta_D = 0.2$. Important evolutionary stages from Figures 4.1 and 4.2 are identified along both abundance trajectories in the trajectory's colour.

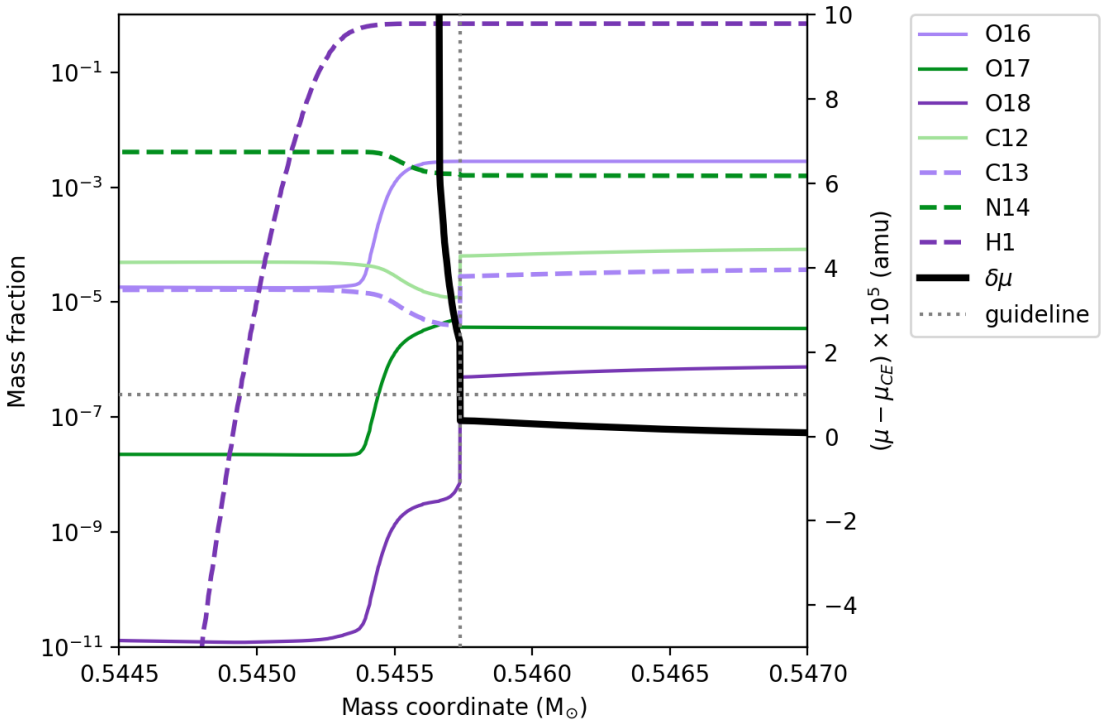

Figure 4.4: Abundance profiles from an early interpulse period of the stellar model with CBP included, focusing on the region around the μ-gradient at the top of the hydrogen-burning shell. The secondary axis shows the mean molecular weight gradient. The grey dotted guidelines show the increase in μ that limits CBP and the corresponding mixing depth.

profiles of O are shown in Figure 3.2. CBP diffuses these radial isotopic features upward into the convective envelope, where they are mixed throughout and expressed in the stellar surface abundances. Comparison of Figures 4.4 and 3.2 illustrates that CBP smoothes localized variations in the radial isotopic abundance profiles down to its mixing depth, redistributing them across the convective envelope. An abrupt change in the abundances of several isotopes is shown at the maximum depth reached by CBP in Figure 4.4.

The model input parameter $\delta\mu = 1$ corresponds to CBP being limited by an increase in μ of $\mu_{CE} * 10^{-5}$, where μ_{CE} is the convective envelope value of μ. Allowing modestly deeper extra mixing produces variations in the surface oxygen isotopic ratios that remain broadly compatible with Group 2 presolar grain data. However, sufficiently deep penetration into the H-burning region leads to excessive depletion of ^{18}O at the surface, placing the model predictions outside the observed grain range (see Section 4.4).

4.2 Effect of Extra Mixing on Aluminium Isotopic Ratios

Al isotopic ratios have been measured for some Group 2 oxide grains (Hynes and Gyngard, 2009). These ratios are compared to the simulated surface abundances in Figure 4.5. Figure 4.5 shows less complete agreement between the simulations and observations compared to Figure 4.3; however, the observed Al isotopic ratios are reached at the end of the AGB phase, when significant mass loss and therefore grain formation occurs. The spread in the $^{18}O/^{16}O$ ratios is captured by varying the model input parameters, as discussed later in Section 4.4.

Throughout the TP-AGB phase, ^{26}Al is generated in the hydrogen burning shell (as outlined in Section 1.5.2). ^{26}Al is introduced to the convective envelope by overshooting at its base when the envelope descends immediately following a thermal pulse (as shown in Figure 4.6). Figure 4.7 shows that, the inclusion of CBP in the stellar model has a minimal effect on the surface $^{26}Al/^{27}Al$ ratio during the TP-AGB phase.

Figure 4.8 shows that the increase in the radial ^{26}Al profile occurs deeper in the star than is reached by CBP. Instead, the surface ^{26}Al is enhanced during the TP-AGB phase by overshooting, when the convective envelope descends directly after a thermal pulse. Figures 4.9 and 4.10 compare the penetration depth of CBP and the descent of the convective envelope relative to the increase in the radial ^{26}Al profile. The descent of the convective envelope penetrates regions with ^{26}Al abundances an order of magnitude higher than those accessed by CBP. As a result, the contribution of CBP to the surface ^{26}Al approximately compensates for decay to ^{26}Mg during the interpulse but does not alter the overall evolutionary trend.

CBP does not affect the evolution of the surface $^{26}Al/^{27}Al$ ratio during the TP-AGB. However, as the star leaves the AGB phase and begins to heat up (due to the contraction of the carbon- and oxygen-rich core) CBP produces an increase in the surface $^{26}Al/^{27}Al$ ratio as demonstrated in Figure 4.8. Although this phase is characterized by significant mass loss and grain formation, it is not well captured by our simulations. In this phase of stellar evolution, the parameterized CBP model exhibits behavior similar to hot bottom burning, connecting the convective envelope to the hydrogen-burning shell.

4.3 Comparison to Spectroscopic Observations

The simulated surface C and O isotopic ratios were compared with spectroscopic measurements of 46 AGB stars with $\lesssim 2$ $M_\odot$ (Hinkle et al., 2016), with details of the observations provided in Section 2.2. The observed stars were classified as Group 1-like or Group 2-like based on a $^{18}O/^{16}O$ ratio greater or less than 10^{-3}, respectively. Figures 4.11 and 4.12 show

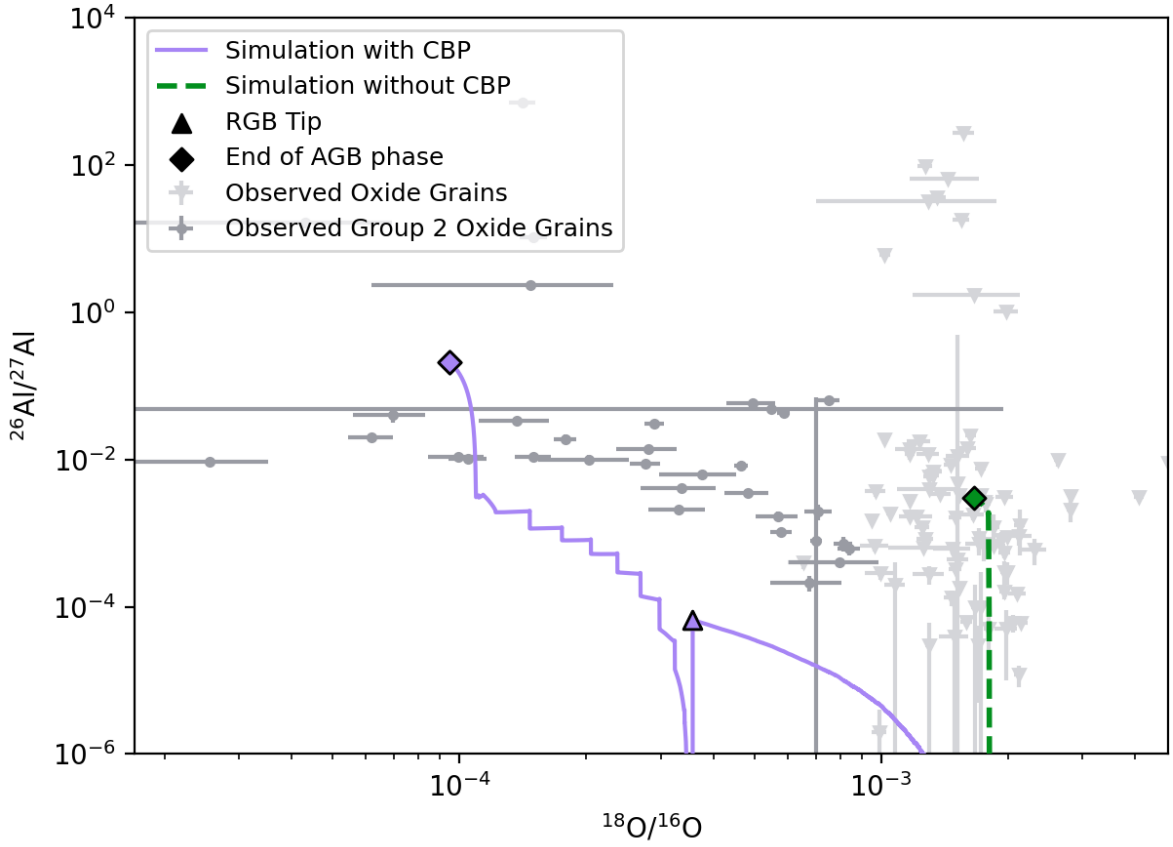

Figure 4.5: Plot of observed Al and O isotopic ratios for Group 2 oxide grains (Hynes and Gyngard, 2009) compared to simulated surface Al and O abundances with and without extra mixing. The model of CBP uses input parameters $\mu_{inc} = 1$ and $\eta_D = 0.2$. Important evolutionary stages from Figures 4.1 and 4.2 are identified along both abundance trajectories in the trajectory's colour. The surface Al abundance ratios of the simulations at the ZAMS and bump luminosity are very low and out of bounds of the plot.

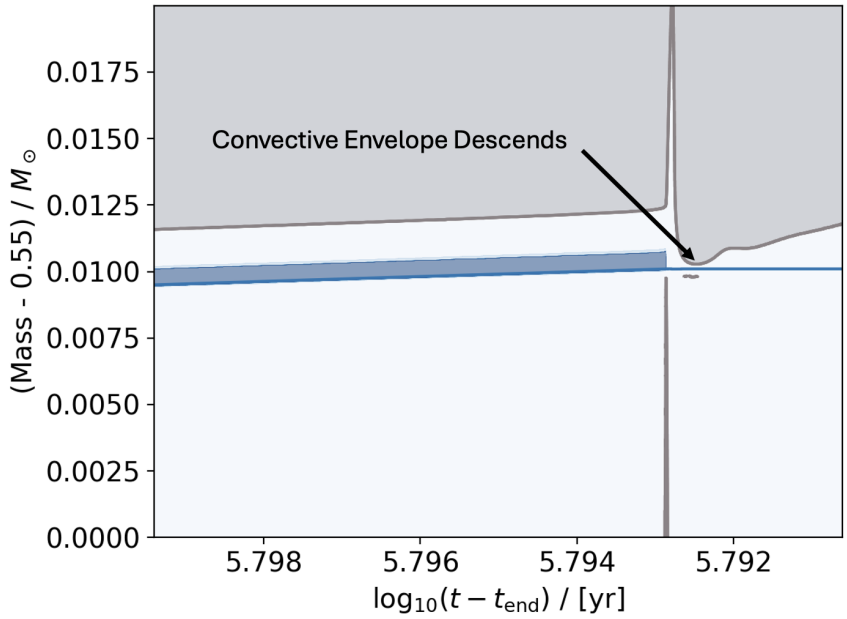

Figure 4.6: Zoomed-in Kippenhahn diagram of the TP-AGB phase showing the convective envelope descending toward the H-burning shell following a thermal pulse. This thermal pulse corresponds to point H. in Figure 1.7.

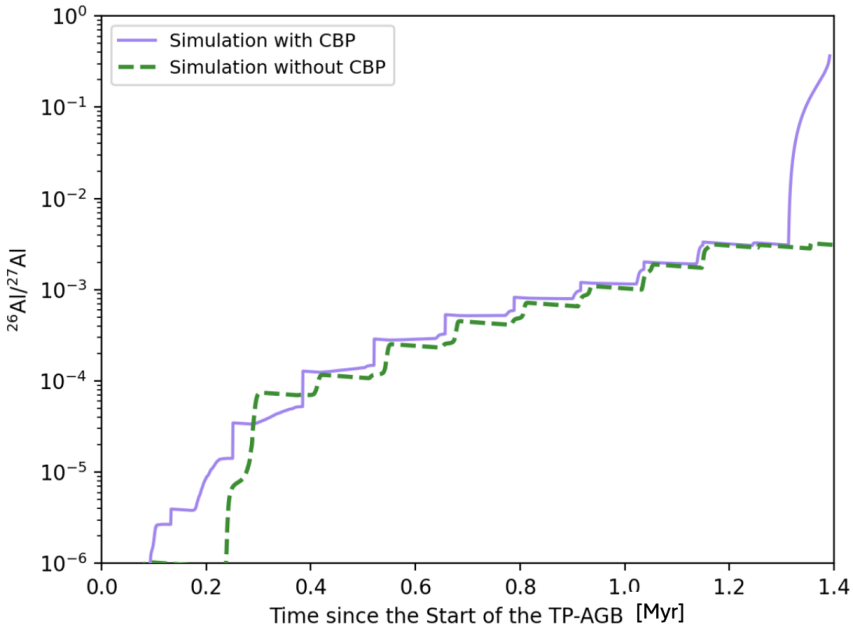

Figure 4.7: A comparison of the simulated surface ^{26}Al/^{27}Al ratio during the TP-AGB with and without CBP included. The model of CBP uses input parameters $\mu_{inc} = 1$ and $\eta_D = 0.2$.

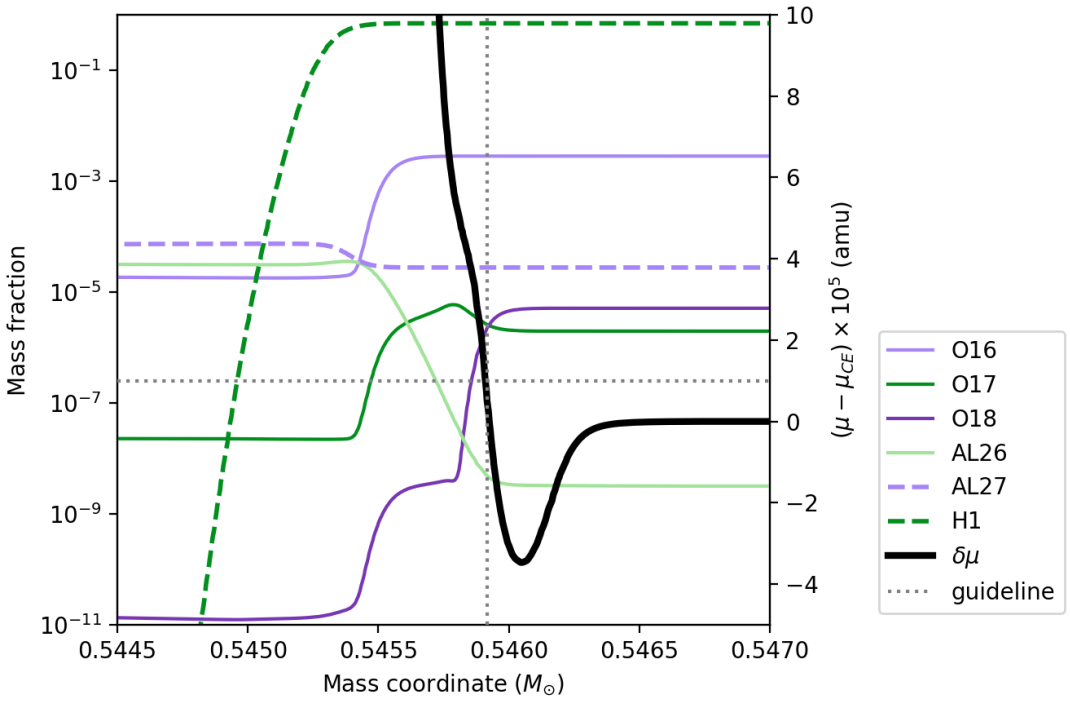

Figure 4.8: Abundance profiles from an early interpulse period of the stellar model without CBP (at the same stage and depth as Figure 3.2). The secondary axis on the right shows the mean molecular weight gradient. The grey dotted guidelines show the increase in μ that would limit CBP and the corresponding mixing depth.

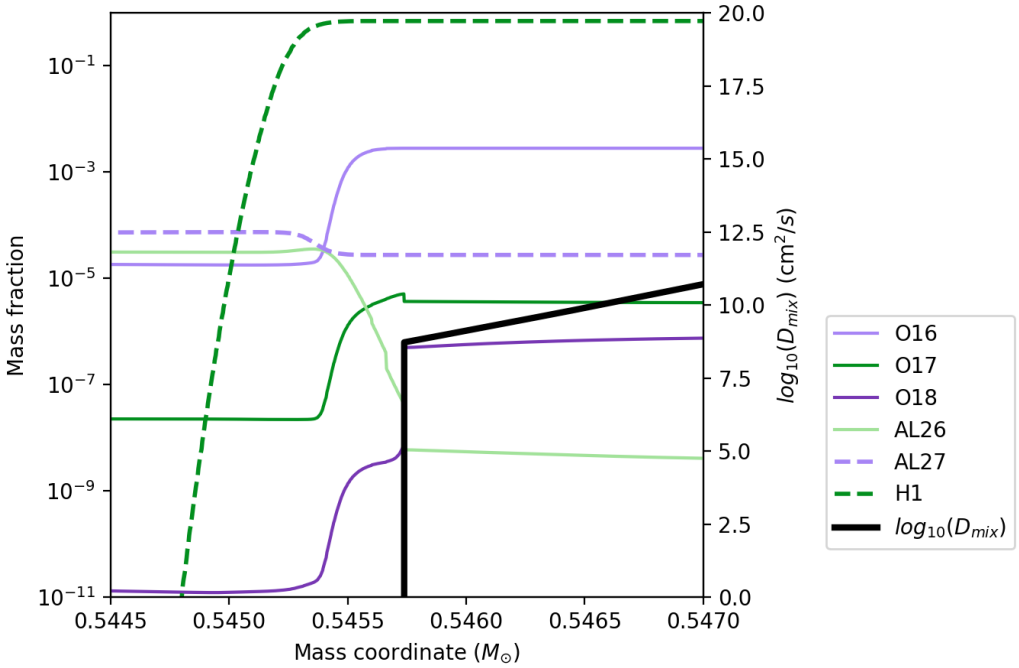

Figure 4.9: Abundance profiles from an early interpulse period of the stellar model with CBP (at the same stage and depth as Figure 4.8). The secondary axis on the right shows the diffusion coefficient.

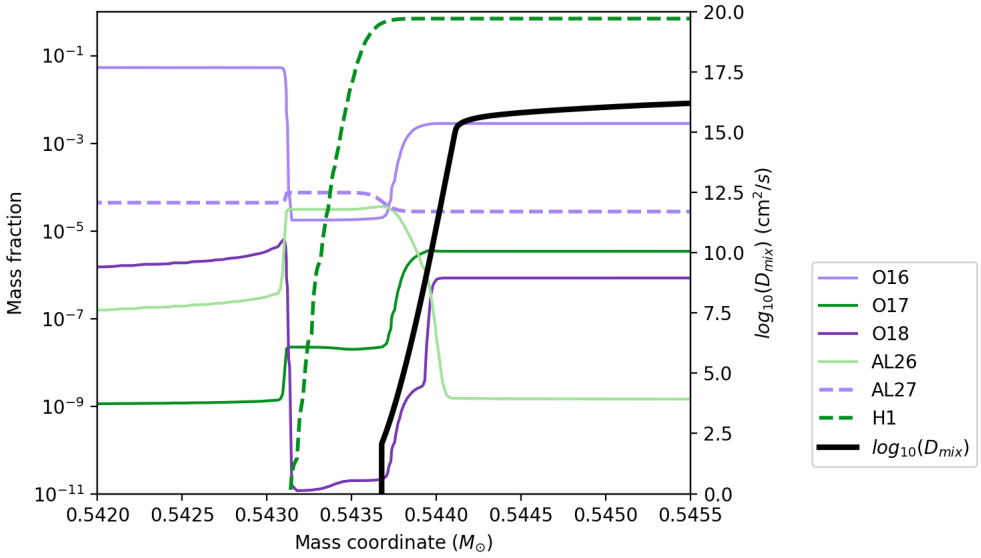

Figure 4.10: Abundance profiles from the same early interpulse period of the stellar model with CBP as Figures 3.2, 4.8, and 4.9. This profile is taken before CBP is triggered when the convective envelope descends after the thermal pulse. The secondary axis on the right shows the diffusion coefficient.

these spectroscopic ratios alongside the simulated surface abundances from stellar models with and without extra mixing presented in Section 4.1.

Figures 4.11 and 4.12 show that the simulation including CBP produces surface isotopic abundances consistent with at least one Group 2 like star. The agreement occurs during the late AGB phase, when most of the presolar grain formation occurs because of the significantly increased mass loss. The CBP model parameters control the level of $^{17}O/^{16}O$ enrichment and $^{18}O/^{16}O$ depletion before the AGB phase ends and the coinciding increase in $^{12}C/^{13}C$. Therefore, the isotopic abundances of the spectroscopically observed Group 2 like stars can be reproduced by varying the depth and efficiency of the extra mixing or the mass of the progenitor star. The stellar model without CBP yields surface abundances that coincide with several Group-1 like stars.

At the end of the AGB phase, CBP reaches a bump in the radial abundance profile of ^{13}C during the final interpulse periods that depletes the spike in $^{12}C/^{13}C$ caused by third dredge-up. CBP facilitates a larger return to the equilibrium ratio before envelope mass loss ends the TP-AGB phase.

The simulation with CBP best reproduces the Group 2-like spectroscopic observation with a $^{12}C/^{13}C$ ratio of 10:1, as shown in Figures 4.11 and 4.12. The simulation with CBP also shows a diminished surface $^{12}C/^{13}C$ ratio throughout the TP-AGB phase in Figures 4.11 and 4.12, because CBP lowers the surface $^{12}C/^{13}C$ ratio. Figure 3.2 shows that the μ-gradient limiting the depth of CBP coincides with a decline and a local increase in the radial abundance profiles of ^{13}C and ^{12}C respectively. CBP mixes reprocessed materials with these features into the convective envelope inducing a lower equilibrium surface $^{12}C/^{13}C$ ratio during both the RGB and AGB phases. At the end of the AGB phase, CBP extends to a region of enhanced ^{13}C during the final interpulse period, suppressing the spike in $^{12}C/^{13}C$ caused by third dredge-up. CBP also facilitates a stronger return to the equilibrium ratio $^{12}C/^{13}C$ after TDU before the significant loss of envelope material ends the TP-AGB phase. The spike in the surface $^{12}C/^{13}C$ ratio due to TDU for the simulation with CBP included is shown at a $^{18}O/^{16}O$ ratio of 10^{-4} and a $^{17}O/^{16}O$ ratio of 10^{-3} in Figures 4.11 and 4.12, respectively.

4.4 Model Parameter Dependence

Group 2 oxide grains show a spread of oxygen isotopic ratios which can be explained by different depths and efficiencies of CBP. Depth and efficiency are incorporated into the parameterized model of CBP using μ_{inc} and η_D respectively. Figure 4.13 shows that for a

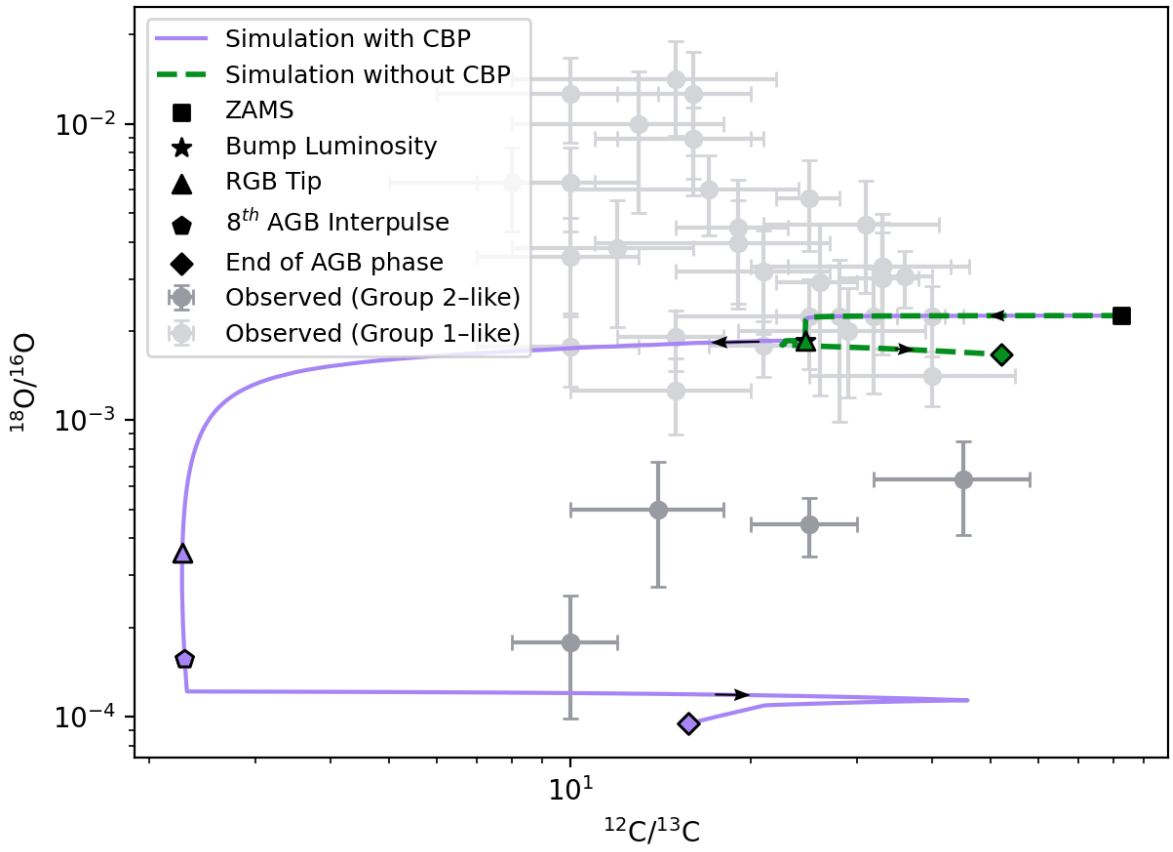

Figure 4.11: Plot of the simulated surface $^{18}O/^{16}O$ and $^{12}C/^{13}C$ ratios with and without extra mixing compared to observed abundances by (Hinkle et al., 2016). Spectroscopically observed stars are divided into Group 2-like and Group 1-like based on $^{18}O/^{16}O$ ratios less than or greater than 10^{-3}, respectively. The model of CBP uses input parameters $\mu_{inc} = 1$ and $\eta_D = 0.2$. Important evolutionary stages from Figures 4.1 and 4.2 are identified along both abundance trajectories in the trajectory's colour. Arrows along the trajectories identify the direction of time evolution.

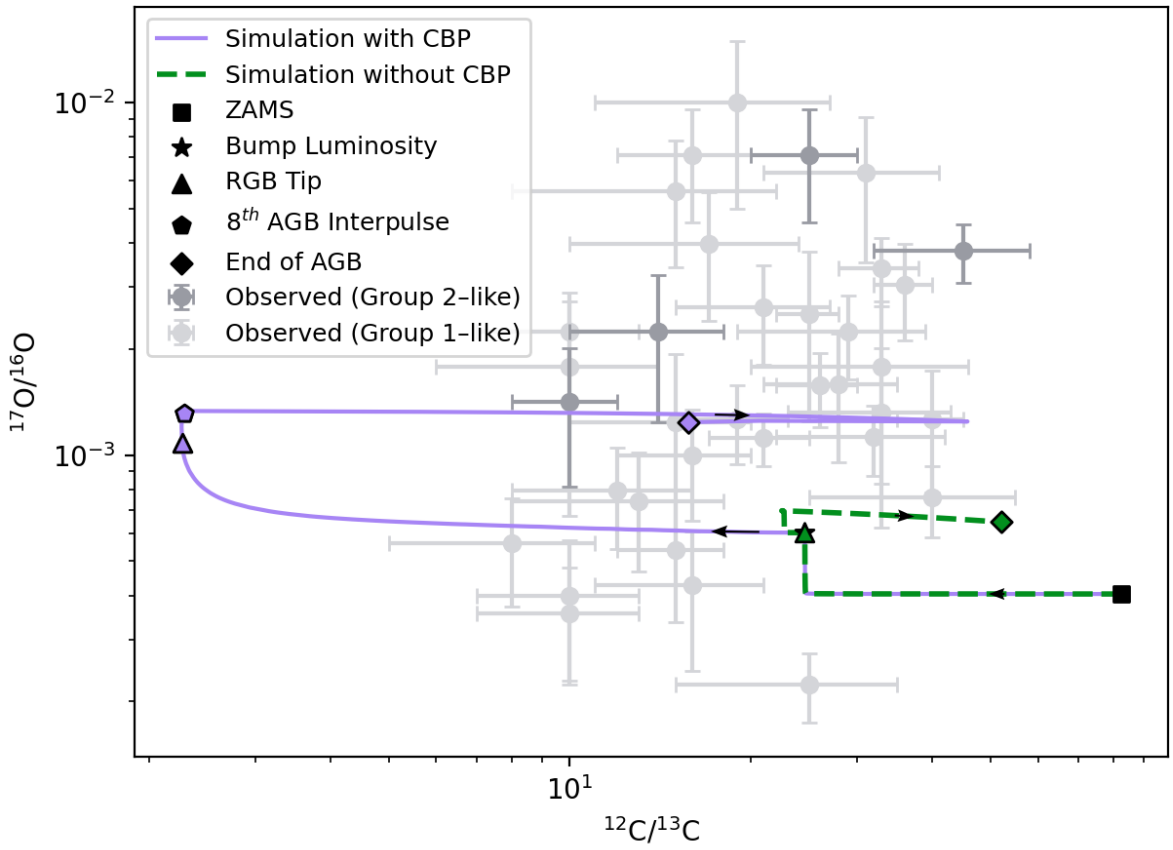

Figure 4.12: Same as Figure 4.11 but for the $^{17}O/^{16}O$ and $^{12}C/^{13}C$ abundance ratios (Hinkle et al., 2016).

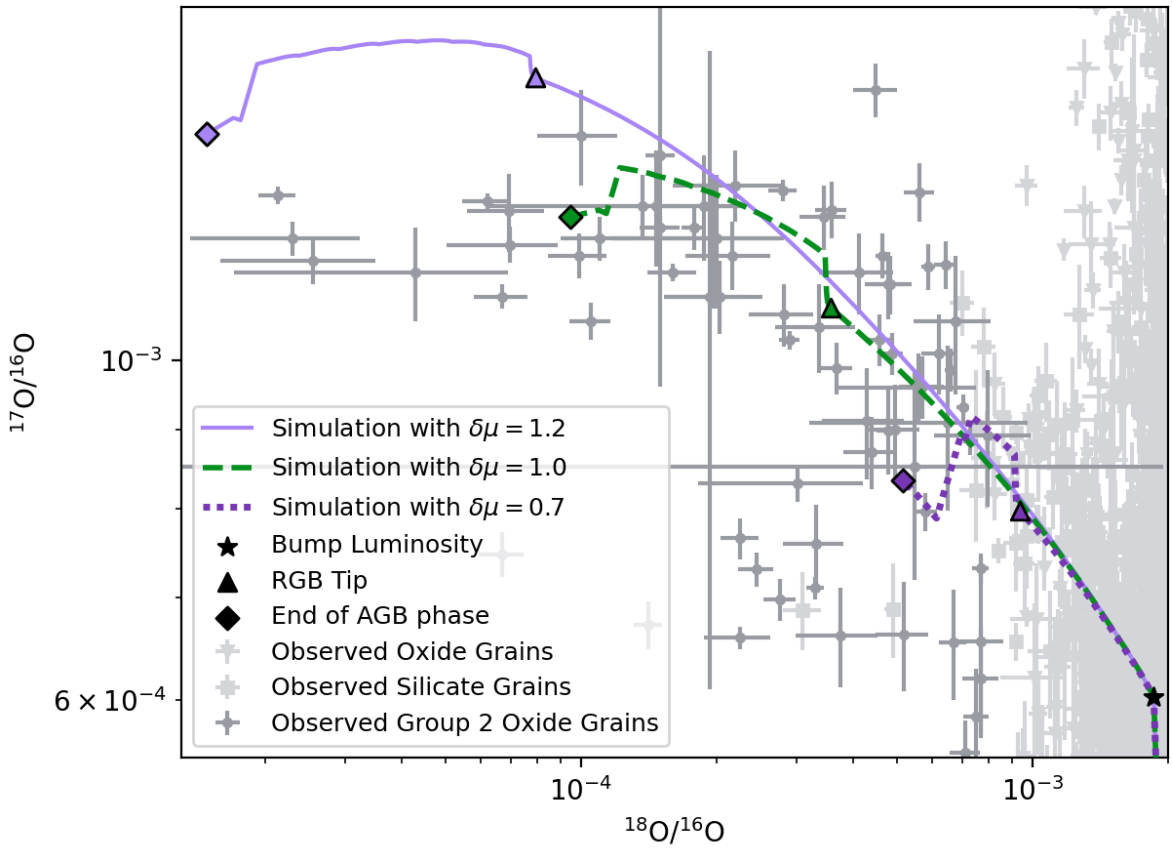

Figure 4.13: Spread of simulated surface O isotopic ratios across the stellar evolution due to varying the depth of extra mixing (as expressed by $\delta\mu$). The simulated abundances are compared to isotopic ratios observed in Group 2 oxide grains (Hynes and Gyngard, 2009). The three simulations use a diffusion coefficient of $\eta_D = 0.2$. Important evolutionary stages are identified along the simulated trajectories in the trajectory's colour.

given mixing efficiency, the range of observed oxygen isotopic ratios can be reproduced by a range of depths given by $\delta\mu^{max}/\delta\mu^{min} < 2$. Figure 4.13 also reinforces that for an efficiency of $\eta_D = 0.2$, the depth of CBP must be limited by an increase in the μ gradient on the order of $10^{-5} * \mu_{CE}$, where μ_{CE} is the mean molecular weight in the convective envelope.

Similarly, Figure 4.14 shows that for a given mixing depth, the range of observed oxygen isotopic ratios can be reproduced by a range of efficiencies given by ${\eta_D}^{max}/{\eta_D}^{min} < 2$.

The implications of lower extra mixing during the RGB phase compared to the AGB phase were explored. A model with lower extra mixing on the RGB is consistent with Denissenkov's proposition of luminosity dependent CBP (Denissenkov et al., 2024). Figure

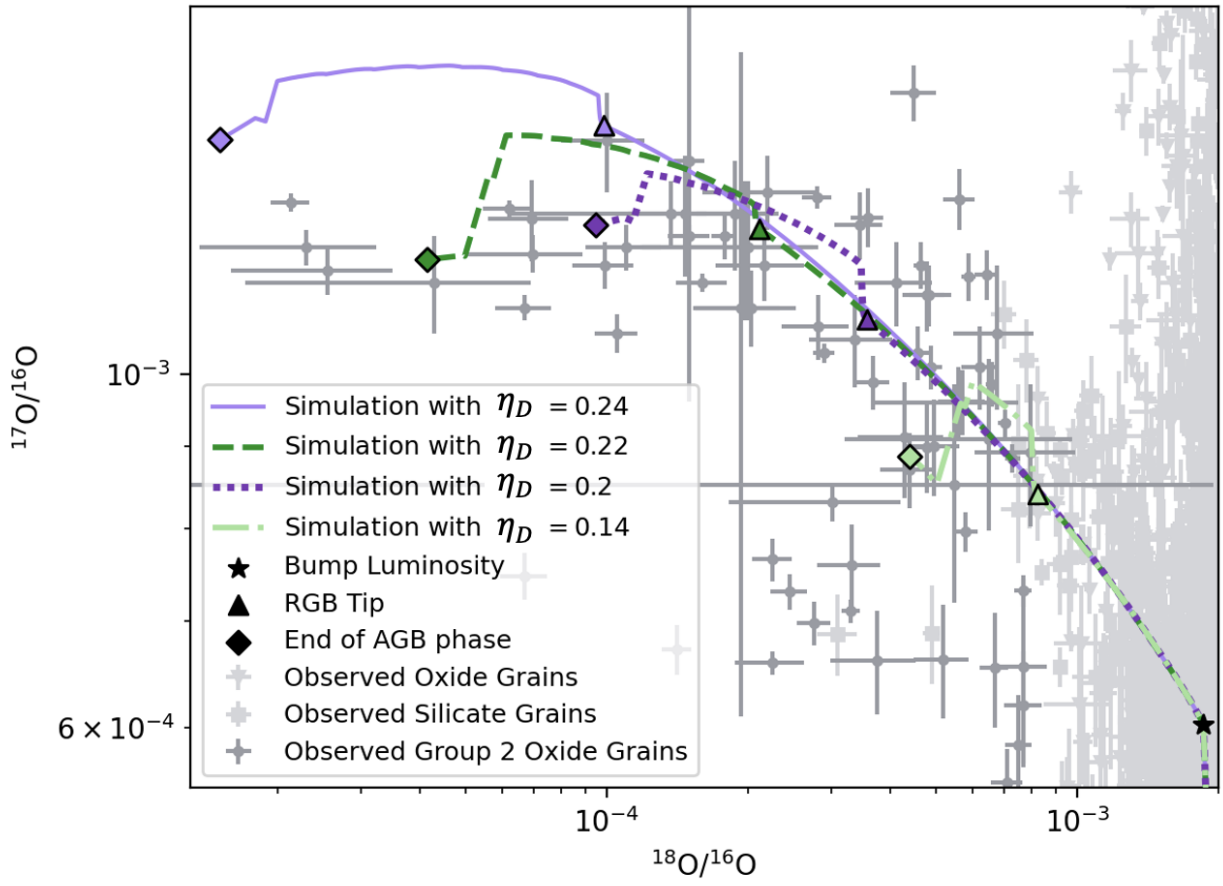

Figure 4.14: Spread of simulated surface O isotopic ratios across the stellar evolution due to varying the efficiency of extra mixing (as expressed by η_D). The simulated abundances are compared to isotopic ratios observed in Group 2 oxide grains (Hynes and Gyngard, 2009). The four simulations use a depth of $\delta\mu = 1$. Important evolutionary stages are identified along the simulated trajectories in the trajectory's colour.

4.15 shows that such a model can reproduce observations, provided extra mixing during the AGB phase is deeper or more efficient to offset the reduced RGB mixing.

Because CBP is not responsible for enriching the surface $^{26}Al/^{27}Al$ ratio changing the CBP model parameters does not have a significant effect on the $^{26}Al/^{27}Al$ ratio.

4.5 Nuclear Physics Impact Study

The input conditions for the one-zone Monte Carlo simulations, representing the deepest layers reached by CBP, are summarized in Table 4.1.

Table 4.1: Stellar input parameters for RGB and AGB one-zone simulations.

Phase	**Temperature (GK)**	**Density ($\mathbf{g\,cm^{-3}}$)**	**Evolution Time (yr)**
RGB	0.0314	6.30	130
AGB	0.0364	4.08	20

Figure 4.16 compares the results of the one-zone simulations to the grain-forming stages of the MESA stellar model. The figure also illustrates the spread in predicted oxygen isotopic abundances obtained from Monte Carlo variations of the nuclear reaction network.

The sensitivity of the isotopic ratios to individual reaction rates was quantified by computing the Pearson correlation coefficients between each reaction rate's multiplication factor and the resulting O isotopic ratios. The sign of the coefficient indicates whether increasing a reaction rate raises or lowers the isotope ratio, while its magnitude reflects the strength of the correlation. The *slope of the correlation*, defined as the change of an isotopic ratio per unit change in the rate multiplier obtained from a linear fit to the Monte Carlo points was extracted. The slope conveys the *scale* of the response: a steep slope indicates that even small rate changes produce large abundance variations, whereas a shallow slope implies weak sensitivity despite possible statistical correlation.

The reactions with the largest combined correlation strength and slope magnitude are listed in Table 4.2, and their relationships are shown in Figures 4.18 and 4.17. The $^{17}O(p,\alpha)^{14}N$ and $^{18}O(p,\alpha)^{15}N$ reactions display strong negative correlations with their respective isotopic ratios, reflecting their roles as the primary destruction channels for ^{17}O and ^{18}O. In contrast, the $^{16}O(p,\gamma)^{17}F$ reaction shows a strong positive correlation with $^{17}O/^{16}O$, as it controls the dominant production pathway for ^{17}O. For comparison, the $^{17}O(p,\gamma)^{18}F$ reaction exhibits only a weak correlation and an almost flat slope, indicating that variations in this rate have little effect on the modeled oxygen isotopic ratios under the conditions explored here and is therefore not considered further in this study.

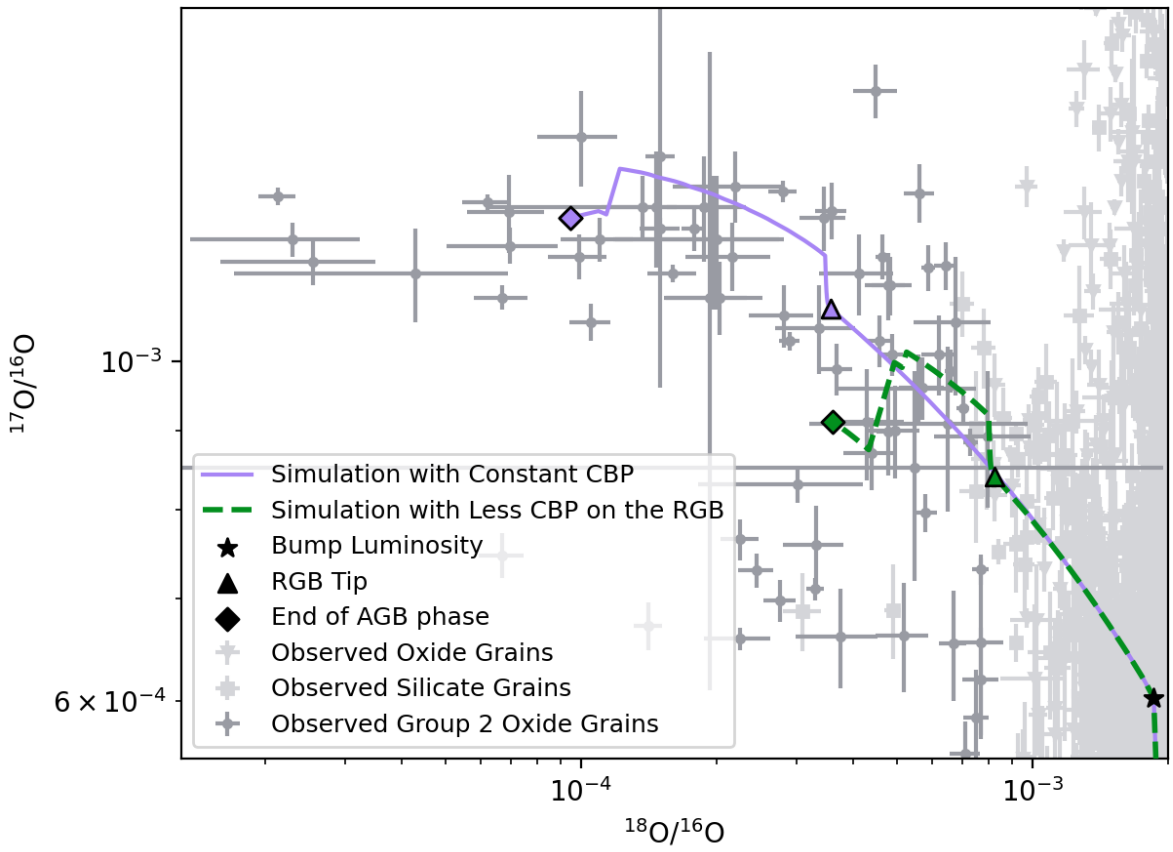

Figure 4.15: Simulated oxygen isotopic abundances are compared for a model with constant CBP throughout and a model with reduced CBP during the RGB phase. The simulated abundances are compared to isotopic ratios observed in Group 2 oxide grains (Hynes and Gyngard, 2009). The model with constant CBP has a diffusion coefficient of $\eta_D = 0.2$ during the RGB and AGB phases. The model with reduced CBP during the RGB phase has diffusion coefficients of $\eta_D = 0.14$ and $\eta_D = 0.2$ during the RGB and AGB phases respectively. The two simulations use a depth of $\delta\mu = 1$. Important evolutionary stages are identified along the simulated trajectories in the trajectory's colour.

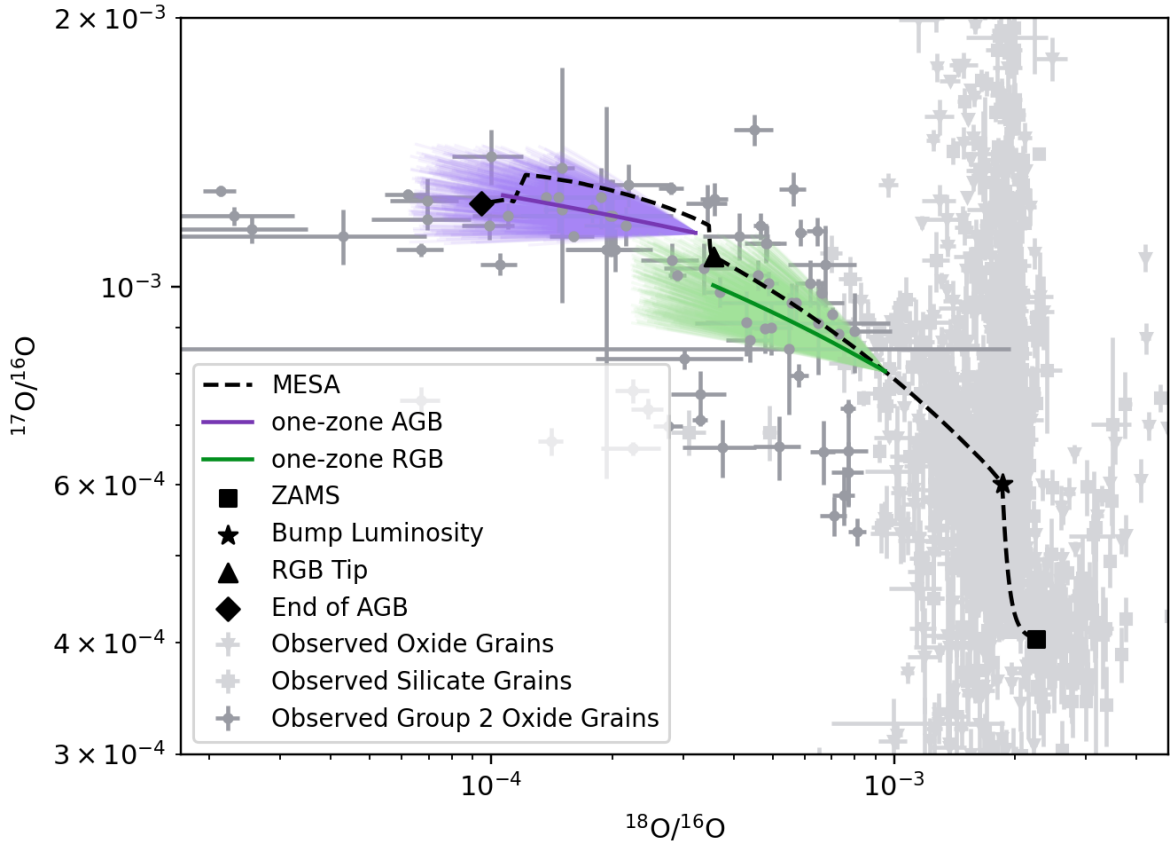

Figure 4.16: Spread of one-zone models relative to the MESA base case simulation and observed grain abundances (Hynes and Gyngard, 2009). The MESA model of CBP uses input parameters $\mu_{\rm inc} = 1$ and $D_{\rm mix} = 0.2$. Key evolutionary stages from Figures 4.1 and 4.2 are labeled along the MESA abundance trajectory.

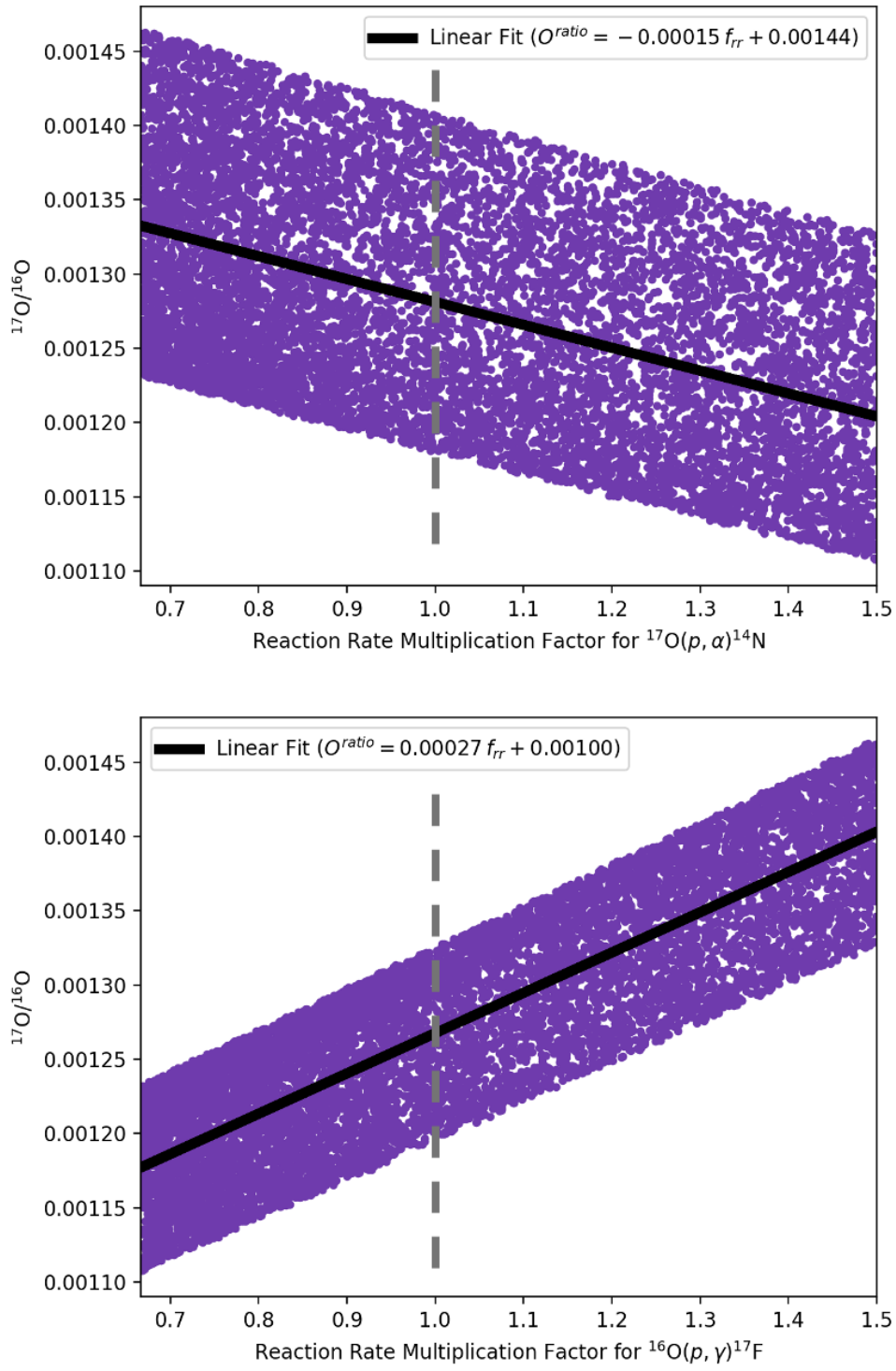

Figure 4.17: Dependence of the one-zone $^{17}O/^{16}O$ ratios on Monte Carlo rate multipliers of the reaction rates $^{17}O(p,\alpha)^{14}N$ (top) and $^{16}O(p,\gamma)^{17}F$(bottom).

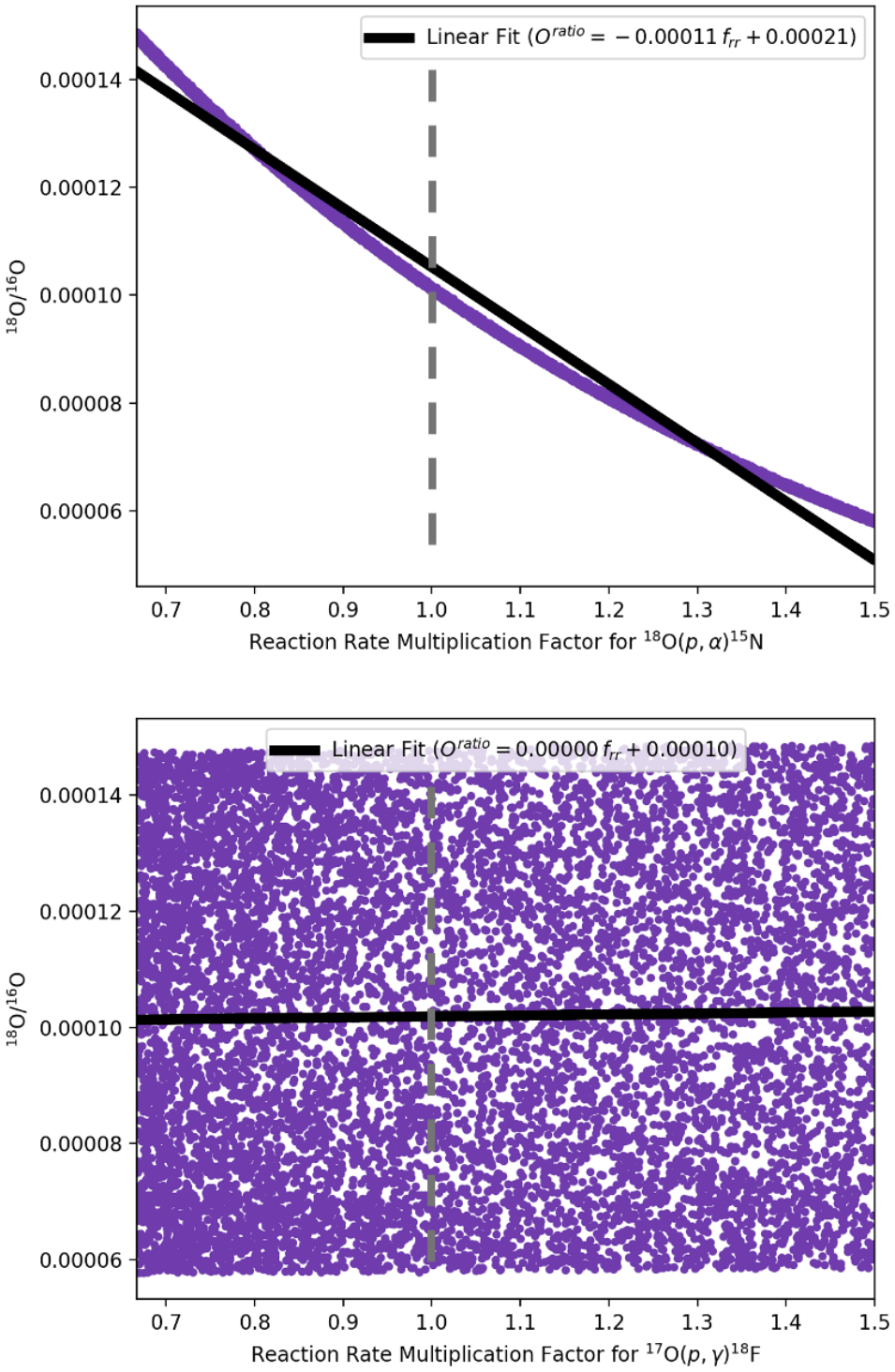

Figure 4.18: Dependence of the one-zone $^{18}O/^{16}O$ ratios on Monte Carlo rate multipliers of the reaction rates $^{18}O(p,\alpha)^{15}N$ (top) and $^{17}O(p,\gamma)^{18}F$ (bottom).

Table 4.2: Pearson coefficients and slopes of correlation for key proton-induced reactions.

Reaction	**Pearson Coefficient**	**Slope of Correlation**	**Isotopic Ratio**
^{17}O(p,α)^{14}N	-0.50	-1.5×10^{-4}	^{17}O/^{16}O
^{16}O(p,γ)^{17}F	0.86	2.7×10^{-3}	^{17}O/^{16}O
^{18}O(p,α)^{15}N	-0.99	-1.1×10^{-4}	^{18}O/^{16}O
^{17}O(p,γ)^{18}F	0.02	0.0	^{18}O/^{16}O

The nuclear uncertainties of ^{17}O(p,α)^{14}N, ^{18}O(p,α)^{15}N, and ^{16}O(p,γ)^{17}F have a significant impact on the oxygen isotopic ratios in the one zone model. A literature review was carried out to identify calculations and measurements of these reactions, focusing on the most recent studies that provide explicitly evaluated reaction rates with quantified uncertainties. For each reaction, a rate evaluation published since 2020 was identified, ensuring that the analysis incorporates the most up-to-date experimental and theoretical constraints available. The corresponding rates at the astrophysically relevant temperature of 0.03 GK are listed in Table 4.5, with more details in Section 2.3.

Table 4.3: Reaction rate bounds from Cyburt et al. (2010), ① Rapagnani et al. (2025), ② Sergi et al. (2020), ③ Iliadis et al. (2022), and ④ Rapagnani et al. (2025). at 30 MK. All reaction rates are given in units of cm^{3}mol^{-1}s^{-1}.

Reaction	**Lower-Upper bound**	**Adopted**	**JINA**	**Ratio**
	($\mathrm{cm^3\,mol^{-1}\,s^{-1}}$)			**Adopted/JINA**
^{17}O(p,α)^{14}N ①	$(1.79 - 8.55) \times 10^{-12}$	4.08×10^{-12}	1.78×10^{-12}	2.29
^{17}O(p,α)^{14}N ②	$(1.05 - 1.48) \times 10^{-12}$	1.24×10^{-12}	1.78×10^{-12}	0.70
^{16}O(p,γ)^{17}F ③	$(6.64 - 7.20) \times 10^{-15}$	6.92×10^{-15}	6.56×10^{-15}	1.05
^{18}O(p,α)^{15}N ④	$(2.31 - 2.86) \times 10^{-11}$	2.50×10^{-11}	2.43×10^{-11}	1.03

Our MESA simulations adopt reaction rates from the JINA Reaclib database (Cyburt et al., 2010). Updated rates listed in Table 4.5 were incorporated into MESA using constant multipliers of the JINA Reaclib rates. The best-fit stellar evolution CBP model ($\delta\mu = 1$, $\eta_D = 0.2$) was rerun using the adopted lower, and upper ^{16}O(p,γ), ^{17}O(p,α), and ^{18}O(p,α) rates. Figures 4.19 and 4.20 show that the updated ^{16}O(p,γ) and ^{18}O(p,α) rates from Iliadis et al. (2022) and Li et al. (2024), respectively, produce no significant deviation from the simulations using the JINA Reaclib rates. The nuclear uncertainties in these reactions likewise result in negligible variation in the simulated surface O isotopic abundances.

Figure 4.21 shows that using the recommended ^{17}O(p,α) rate from Cyburt et al. (2010), Sergi et al. (2020), or Rapagnani et al. (2025) causes a large change in the the simulated surface O isotopic abundances. Rapagnani et al. (2025) reports a higher ^{17}O(p,α) rate

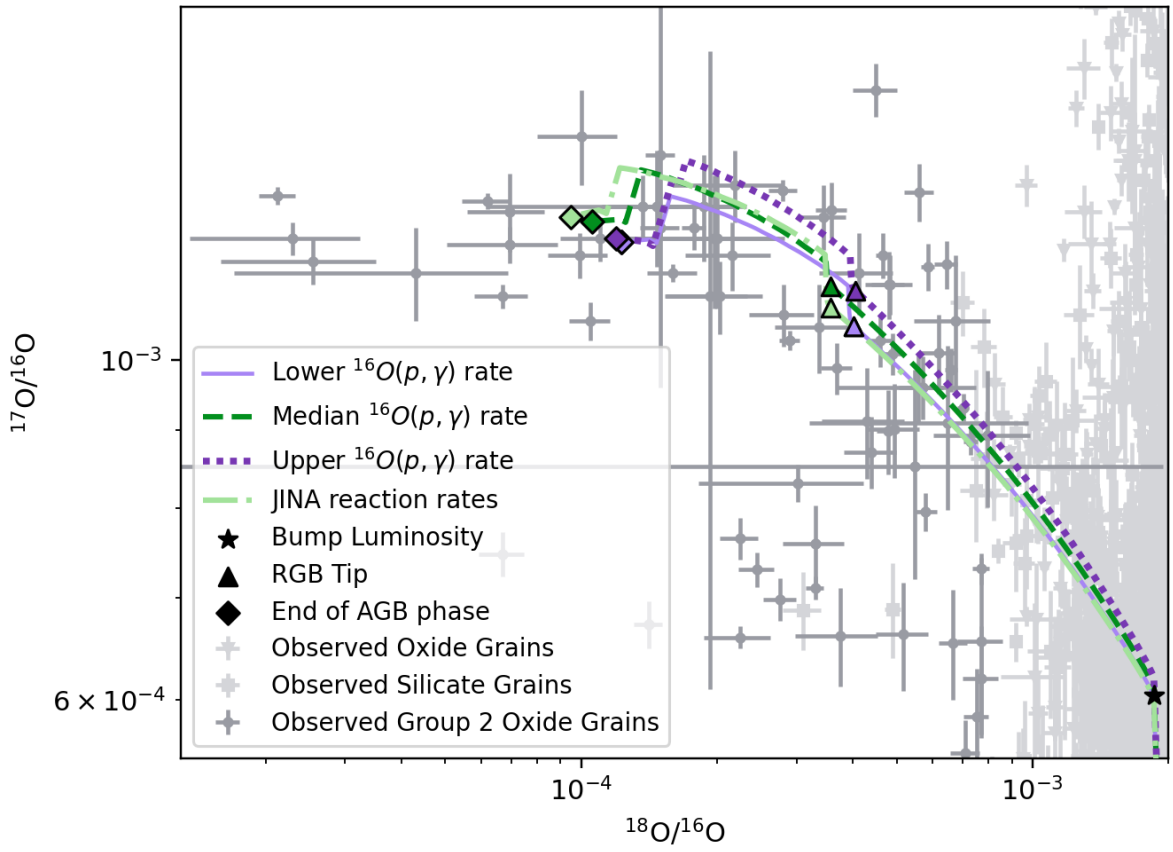

Figure 4.19: Spread in simulated surface O isotopic ratios throughout stellar evolution caused by varying the $^{16}\mathrm{O}(p,\gamma)$ rate at 0.03 GK between the lower, adopted, and upper limits from (Iliadis et al., 2022), relative to the JINA Reaclib rate (Cyburt et al., 2010). The four simulations use a depth of $\delta\mu = 1$ and an efficiency of $\eta_D = 0.2$. Important evolutionary stages are identified along the simulated trajectories in the trajectory's colour.

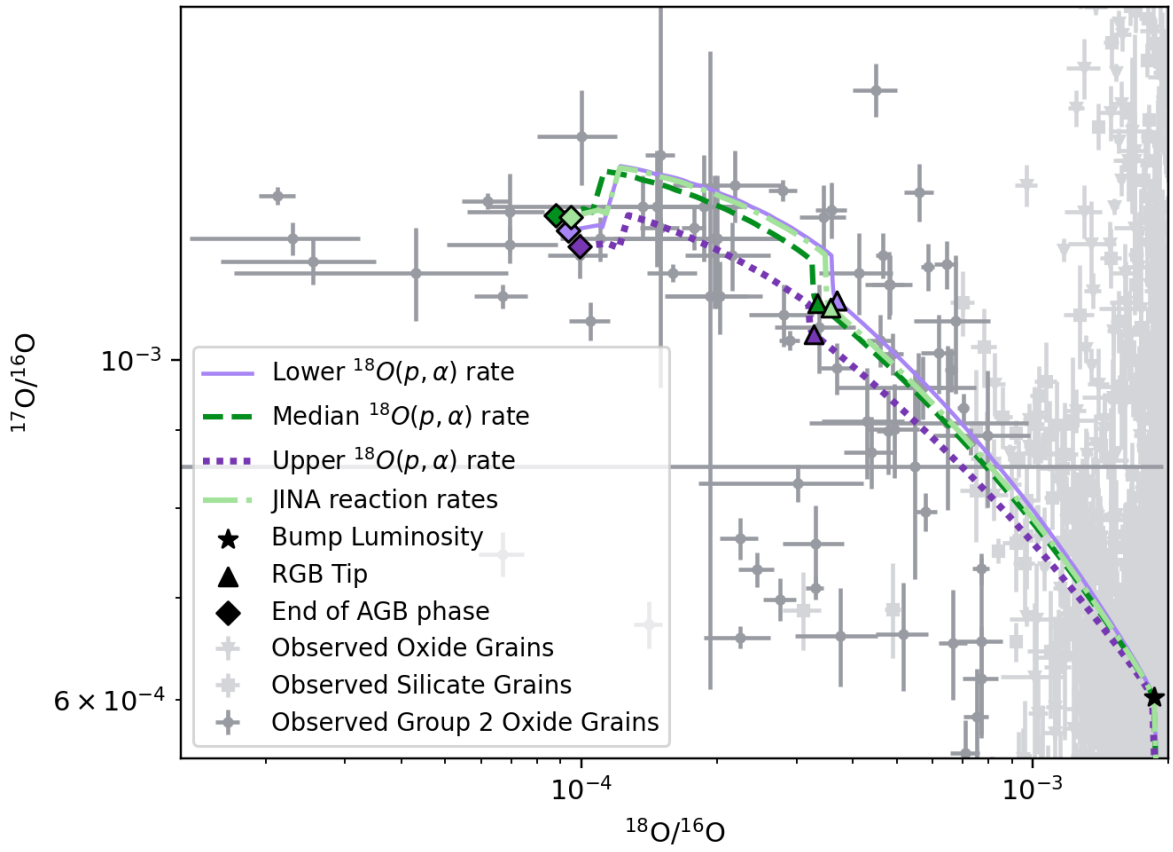

Figure 4.20: Spread in simulated surface O isotopic ratios throughout stellar evolution caused by varying the $^{18}\mathrm{O}(p,\alpha)$ rate at 0.03 GK between the lower, adopted, and upper limits from (Li et al., 2024), relative to the JINA Reaclib rate (Cyburt et al., 2010). The four simulations use a depth of $\delta\mu = 1$ and an efficiency of $\eta_D = 0.2$. Important evolutionary stages are identified along the simulated trajectories in the trajectory's colour.

compared to Cyburt et al. (2010) which results in faster destruction of ^{17}O and a smaller ^{17}O bump at the deepest points reached by CBP. Contrarily, Sergi et al. (2020) reports a 0.69 $\times$ smaller $^{17}\mathrm{O}(p,\alpha)$ rate compared to Cyburt et al. (2010) which results in the opposite effect. The observations from grains best agree with the Cyburt et al. (2010), Sergi et al. (2020), or the lower limit proposed by Rapagnani et al. (2025). The mixing parameters of the CBP model were varied with the $^{17}\mathrm{O}(p,\alpha)$ rate from Rapagnani et al. (2025), however, the enhanced $^{17}\mathrm{O}(p,\alpha)$ rate prevented the necessary $^{17}\mathrm{O}/^{16}\mathrm{O}$ enrichment from occurring. Figure 4.22 shows that the nuclear uncertainties proposed by Sergi et al. (2020) cause a negligible variation in the simulated surface O isotopic abundances. Figure 4.23 shows that the nuclear uncertainties proposed by Rapagnani et al. (2025) cause a significant spread in the simulated surface O isotopic abundances, this may be partially attributed to the fact that they report their upper and lower bounds to 3σ.

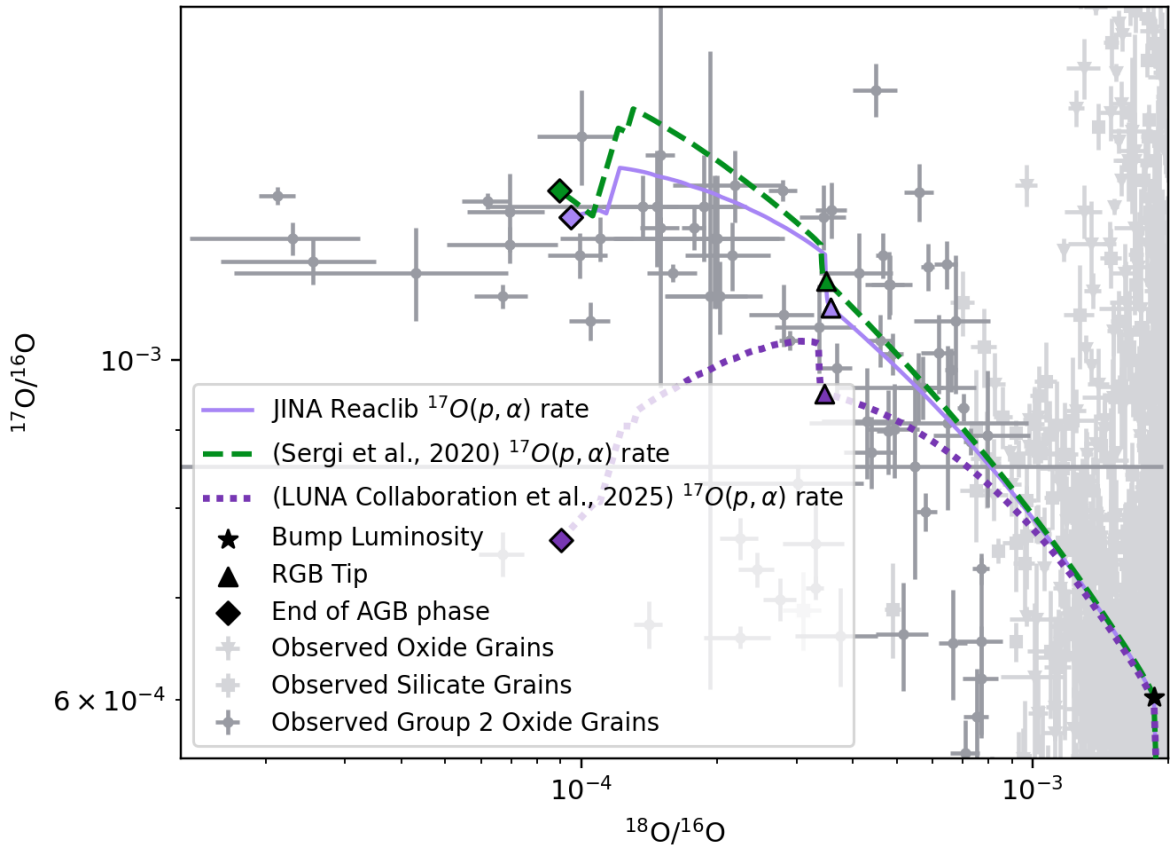

Figure 4.21: The simulated surface O isotopic ratios throughout stellar evolution using the adopted $^{17}\mathrm{O}(p,\alpha)$ rate at 0.03 GK from (Rapagnani et al., 2025), (Sergi et al., 2020), and (Cyburt et al., 2010). The three simulations use a depth of $\delta\mu = 1$ and an efficiency of $\eta_D = 0.2$. Important evolutionary stages are identified along the simulated trajectories in the trajectory's colour.

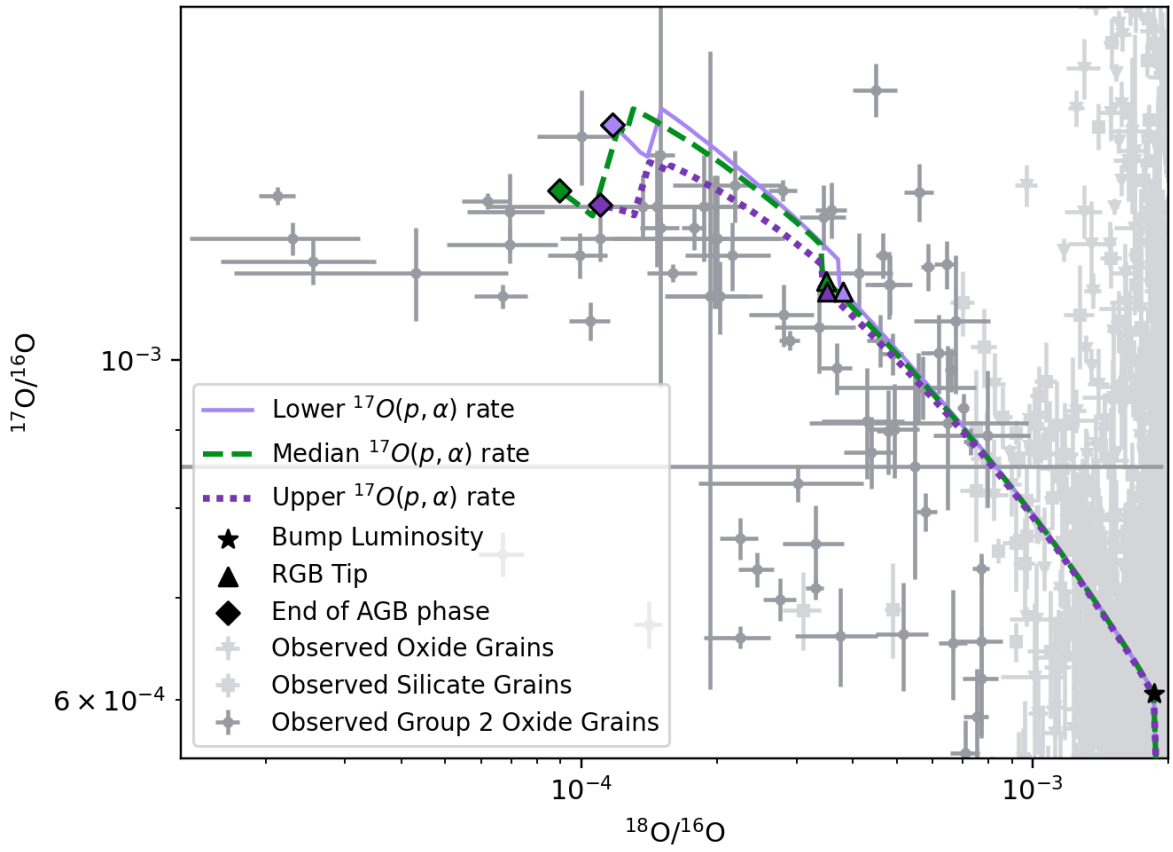

Figure 4.22: Spread in simulated surface O isotopic ratios throughout stellar evolution caused by varying the $^{17}O(p,\alpha)$ rate at 0.03 GK between the lower, adopted, and upper limits from (Sergi et al., 2020). The three simulations use a depth of $\delta\mu = 1$ and an efficiency of $\eta_D = 0.2$. Important evolutionary stages are identified along the simulated trajectories in the trajectory's colour.

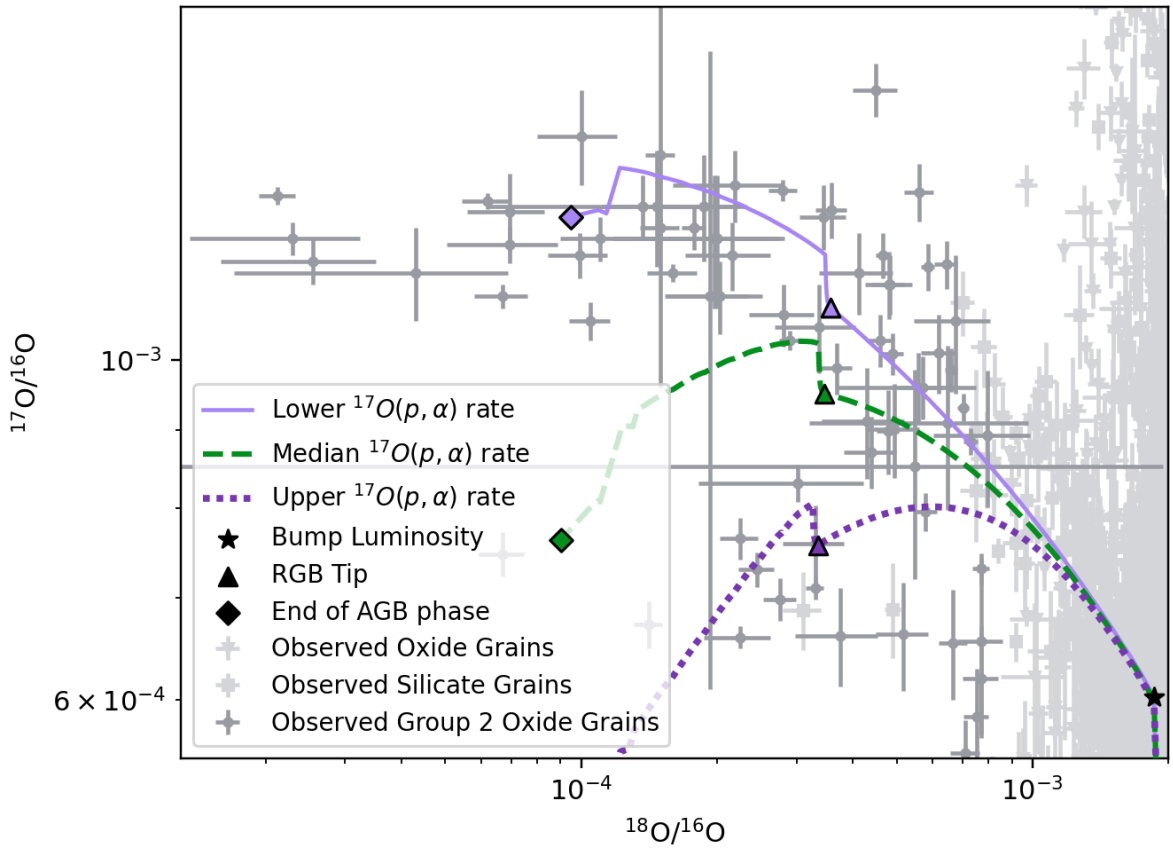

Figure 4.23: Spread in simulated surface O isotopic ratios throughout stellar evolution caused by varying the $^{17}O(p,\alpha)$ rate at 0.03 GK between the lower, adopted, and upper limits from (Rapagnani et al., 2025). The three simulations use a depth of $\delta\mu = 1$ and an efficiency of $\eta_D = 0.2$. Important evolutionary stages are identified along the simulated trajectories in the trajectory's colour.

Chapter 5

Discussion

5.1 Summary of Findings

Using self-consistent stellar evolution models of low-mass AGB stars, this work reproduces the observed oxygen isotopic ratios in Group 2 grains and matches surface abundances measured in similar-mass AGB stars. The models show that CBP is intrinsically self-limiting: a mean molecular weight contrast as small as $\Delta\mu \approx \mu_{\rm CE} \times 10^{-5}$ suppresses further mixing, stabilizing the stellar structure. Varying the depth and diffusion efficiency of CBP spans the full range of observed isotopic compositions, linking grain data and stellar observations within a unified framework. A reaction-rate sensitivity analysis identifies ^{17}O(p,α)^{14}N as the dominant nuclear uncertainty and supports the astrophysical rate proposed by (Sergi et al., 2020). Overall, the results demonstrate that modest, composition-driven circulation in low-mass AGB stars can quantitatively account for the oxygen isotopic patterns observed in Group 2 presolar grains.

5.2 Implications of Findings

Under conditions reproducing the observed oxygen isotopic ratios, CBP was halted by a small increase in the mean molecular weight gradient (on the order of $\mu_{CE} \times 10^{-5}$). This result implies that the mechanism driving CBP must operate at low energies and involve only gentle circulation. It reinforces the interpretation that Group 2 oxygen-rich presolar grains originated from a slow, non-disruptive process that did not significantly alter the stellar structure.

The aluminum isotopic ratios measured in Group 2 oxide grains, however, were only re-

produced near the end of the TP-AGB phase. This discrepancy may reflect an astrophysical process not fully captured by our stellar model, such as changes in envelope dynamics or mass loss as the TP-AGB phase ends, or it could point to remaining uncertainties in the underlying nuclear physics. Changing some reaction rates would allow CBP to simultaneously alter the O and Al isotopic compositions during the TP-AGB phase. To reproduce the observed ^{26}Al/^{27}Al ratios together with the O isotopic abundances, the ^{25}Mg(p,γ)^{26}Al reaction rate may need to be higher at temperatures near 0.03 GK. An enhanced rate under these conditions would lead to concurrent enrichment in ^{26}Al and ^{17}O and depletion of ^{18}O. Alternatively, this outcome could also be achieved through slightly deeper CBP combined with reduced ^{18}O destruction and ^{17}O production rates at temperatures around 0.03 GK.

The ability of small variations in the CBP depth and efficiency to reproduce the full range of observed grain compositions implies that the process operates near a stability threshold. Minor differences between otherwise similar AGB stars could therefore result in distinct isotopic signatures, pointing to CBP as a self-regulating and highly sensitive mixing phenomenon. Because changes in mixing depth and efficiency can produce similar isotopic results, it is difficult to pinpoint exactly how CBP operates inside the star.

The uncertainty in the ^{17}O(p,α)^{14}N reaction rate remains the dominant nuclear source of uncertainty in models of low-mass AGB stars that aim to reproduce the isotopic compositions of presolar grains through CBP. Grain observations are best matched by simulations adopting either the Cyburt et al. (2010) rate, the rate proposed by Sergi et al. (2020), or the lower bound of the ^{17}O(p,α)^{14}N rate recommended by Rapagnani et al. (2025). Palmerini et al. (2021) also found that adopting the higher ^{17}O(p,α)^{14}N rate proposed by Bruno et al. (2016) leads to reduced agreement between low-mass CBP models and Group 2 grain data. This may indicate a shortcoming in the CBP or dust-formation model, or it could imply that the true stellar rate is slightly lower than the value calculated by Rapagnani et al. (2025). HBB in intermediate-mass AGB stars, when combined with the ^{17}O(p,α)^{14}N rate proposed by Rapagnani et al. (2025) and modest dilution with near-solar material, provides an alternative explanation for the oxygen isotopic compositions of Group 2 grains (Lugaro et al., 2017).

5.3 Comparison to Other Works

This work builds on and extends the results of Nollett et al. (2003), addressing many of the open questions raised in their studies. In contrast to those earlier models, which applied CBP through post-processing nucleosynthesis calculations on fixed stellar structures, the present work incorporates CBP self-consistently within the stellar evolution simulation.

This approach allows the interaction between mixing and stellar structure, particularly the development of the mean molecular weight gradient, to emerge naturally rather than being imposed externally. A key finding is that even a minute increase in the molecular weight gradient, on the order of $\mu_{\rm CE} \times 10^{-5}$, limits the extent of CBP, effectively halting deep circulation. The absence of such a feature in the Nollett et al. (2003) models likely reflects the simplified stellar structures and computational constraints of the time, rather than a fundamental incompatibility of CBP with stellar interiors. Palmerini et al. (2021) also includes CBP through post-processing giving rise to the same issues.

The diffusive formulation adopted here identifies the extra mixing as a slow, secular process—consistent with the physical assumptions of Nollett et al. (2003) and Palmerini et al. (2021)—but implemented in a way that preserves the stellar stratification throughout the radiative zone. This ensures that CBP operates without artificially perturbing the star's thermal structure.

Palmerini's magnetic-buoyancy models reproduce many of the isotopic signatures of Group 2 presolar oxide grains, but they achieve the requisite ^{26}Al/^{27}Al ratios only when ^{18}O is already severely depleted. In the our model, comparable aluminum enrichments appear under the same conditions, either at the end of the TP-AGB or in cases where the mixing penetrates too deeply and over-depletes ^{18}O. This consistency reinforces the link between deep mixing processes in low-mass AGB stars and the isotopic compositions of Group 2 grains, while emphasizing that reproducing both oxygen and aluminum isotopic ratios simultaneously remains a stringent test for models of extra mixing (Palmerini et al., 2021).

Compared to Denissenkov et al. (2024) this study extends CBP into the TP-AGB phase and replaces a fixed mixing depth with one that is dynamically limited by the evolving mean molecular weight gradient, providing a more physically motivated boundary for the onset and cessation of extra mixing.

Figure 5.1 compares the radial dependence of the diffusion coefficient from our parametric CBP model with values extracted from 3D hydrodynamic simulations of rotation-enhanced, wave-driven mixing presented by Blouin et al. (2025). While the diffusion coefficients required by the CBP model to reproduce Group 2 grain data are systematically larger than those directly measured in the simulations, the 3D models do not probe the full depth reached by our model of CBP. In the 3D hydrodynamics simulations, "fast rotation" corresponds to solid-body rotation rates up to $\sim 7 \times 10^{-5}\,\mathrm{rad\,s^{-1}}$, while "large envelope" models capture a greater radial extent of the lower convective envelope, allowing larger convective structures and more efficient wave excitation. Extrapolation of trends observed in these fast-rotating, large-envelope cases suggests that diffusion coefficients of comparable magnitude may be

attainable near the lower boundary of the extra-mixing region. Although such extrapolation remains uncertain, this comparison indicates that wave-driven mixing enhanced by rapid rotation can plausibly approach the efficiency required by CBP, supporting it as a viable physical mechanism underlying the parameterized extra mixing.

Physically, this suggests that internal gravity waves excited at the base of the convective envelope can contribute to slow mixing below the envelope. In rapidly rotating stars with extended convective envelopes, stronger convective motions generate more energetic waves that propagate into the underlying radiative zone. The dissipation of these waves deposits angular momentum and drives weak circulations capable of transporting material across the radiative barrier, providing a plausible physical origin for the non-convective mixing represented by CBP. In a 1D framework, such wave-driven, rotation-enhanced mixing can be represented as a slow diffusive process confined to the region beneath the convective envelope, as in our CBP prescription. The extent to which this mixing can penetrate deeper layers remains uncertain and requires multidimensional simulations that extend further into the radiative interior.

5.4 Limitations

The present work employed a parameterized model of CBP that reproduces its observational effects without identifying or modeling the underlying physical mechanism. The extra mixing is represented through a diffusive prescription, but the astrophysical driver, whether rotational, magnetic, or wave-induced, remains unspecified. Moreover, the mixing depth and efficiency of CBP are treated as independent parameters, whereas both are fundamentally linked through the energy available to drive circulation and should ideally be coupled within a unified physical framework. The simulations in this work are restricted to a single stellar mass (1.2 $M_\odot$) and metallicity ($[Fe/H] = -0.3$), limiting the generality of the results, as the efficiency and extent of CBP are expected to depend on these properties.

The stellar model adopted in this work assumes an initial metallicity of [Fe/H] $= -0.3$, corresponding to approximately half the solar metal content. This value lies within the range of metallicities observed in Galactic disk stars, however, it is somewhat lower than the near-solar metallicities commonly inferred for the parent stars of most Group 1 and Group 2 presolar oxide grains (Boothroyd and Sackmann, 1999; Palmerini et al., 2021). Metallicity influences the initial oxygen isotopic composition through galactic chemical evolution, with lower metallicity models generally exhibiting lower initial $^{18}O/^{16}O$ and $^{17}O/^{16}O$ ratios (Prantzos et al., 1996). CBP modifies the abundance ratios through additional ^{18}O destruction and

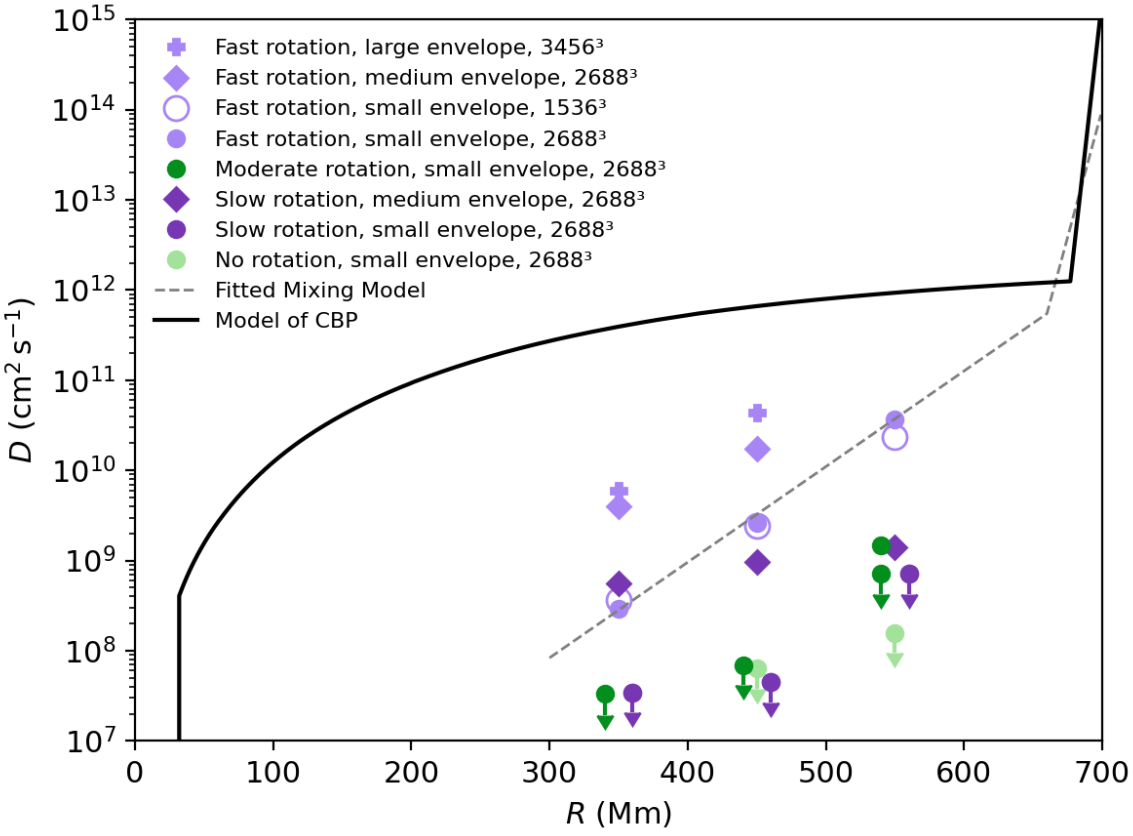

Figure 5.1: Radial profiles of the diffusion coefficient from our parametric CBP model are compared with values from 3D hydrodynamic simulations of rotation-enhanced, wave-driven mixing by Blouin et al. (2025). Both models correspond to a 1.2 $M_\odot$ star at the tip of the RGB. In the 3D simulations, diffusion coefficients were estimated by tracking the radial dispersion of passive tracer fluid within spherical shells over multiple runs. 3D simulation results are labeled by the imposed solid-body rotation rate, the radial extent of the modeled convective envelope, and numerical resolution. The dashed line indicates a parametric diffusion profile fitted to the 3D simulation data to facilitate direct comparison with the CBP prescription.

^{17}O enhancement through proton-driven reactions at fixed temperatures, independent of the starting composition. Consequently, changes in metallicity modestly shift the baseline ratios without altering the need for CBP to reproduce Group 2 grain signatures.

The stellar models are evolved only through the TP-AGB phase; thus, the behavior at the onset of the post-AGB and envelope ejection phases, where mass loss and hot bottom burning may alter surface abundances, remains uncertain. As with all 1D stellar models, inherently multidimensional processes such as turbulent entrainment, shear instabilities, and magnetic reconnection are approximated through a scalar diffusion coefficient, precluding the capture of time-dependent or asymmetric mixing behavior. Finally, the model does not include feedback between CBP and mass loss, although these processes may interact during the late AGB when dust formation and envelope erosion accelerate.

Chapter 6

Conclusion and Outlook

6.1 Conclusion

This work demonstrates that secular CBP operating in low-mass AGB stars can reproduce the isotopic compositions of Group 2 oxygen-rich presolar grains. The stellar evolution model incorporating CBP with parameters $\mu_{\rm inc} = 1$ and $\epsilon_D = 0.2$ successfully reproduces the observed oxygen isotopic ratios, while the aluminum isotopic ratios are only marginally consistent, only reproducing observed ^{26}Al/^{27} Al values at the end of the TP-AGB phase. Despite this limitation, the model captures the overall trends in both elements and remains consistent with isotopic patterns observed in presolar grains and in spectroscopic measurements of AGB stars of similar mass.

By implementing CBP self-consistently within the stellar evolution framework rather than through post-processing, this work captures the development of the mean molecular weight gradient that naturally limits the extent of extra mixing. The results confirm that even small increases in this gradient can suppress circulation entirely, providing a self-regulating mechanism that stabilizes the stellar structure against excessive mixing. This feedback supports the interpretation of CBP as a slow, low-energy process that operates within the radiative zone without disrupting hydrostatic or thermal equilibrium. The parameterized diffusion approach also reproduces the observed range of isotopic abundances through modest variations in mixing depth and efficiency, underscoring both the robustness and degeneracy of the CBP mechanism within this stabilizing framework.

The CBP model applied here aligns qualitatively with those proposed to explain lithium enrichment at the tip of the RGB, suggesting that similar mixing physics may operate in both evolutionary phases. The consistency between the required mixing parameters in RGB

and AGB stars strengthens the case for a unified physical origin, such as magnetically or rotationally-driven circulation.

Overall, these results reinforce the role of CBP in connecting stellar mixing processes to the isotopic record preserved in presolar grains, while highlighting the need for improved nuclear data and multidimensional stellar models to fully constrain the mechanism and its astrophysical driver.

6.2 Outlook

Future work should develop a unified parameterization of CBP that can simultaneously reproduce the oxygen isotopic compositions of Group 2 oxygen-rich presolar grains and the lithium enrichment observed at the tip of the RGB. A key objective is to determine whether both signatures can arise within a single stellar model and to quantify how luminosity-dependent diffusion coefficients influence the ability of simulations to match observed isotopic patterns. Extending this analysis across a grid of stellar masses and metallicities would clarify the mass dependence of CBP and identify the stellar populations most likely to contribute to Group 2 grains.

Further investigation of the relationship between mixing depth and efficiency is also warranted. The present study demonstrates that small variations in these parameters can span the full range of observed grain abundances, suggesting a strong degeneracy that complicates the identification of the physical mechanism driving CBP. Exploring how this degeneracy evolves when mixing and energy transport are treated self-consistently could help constrain the energetics and timescales of the underlying process. The role of the small mean molecular weight gradient capable of halting mixing should also be examined in detail to evaluate its potential impact in other stellar environments. Constraining the relationship between the depth, rate, and energetic requirements of CBP would provide critical insight into whether the process originates from rotation, magnetic buoyancy, internal gravity waves, or another mechanism. Such constraints would not only clarify the physical nature of CBP but also guide observational or asteroseismic diagnostics capable of distinguishing between these possible drivers in evolved stars.

The nuclear-physics sensitivity analysis highlights the continuing importance of the ^{17}O(p,α)^{14}N reaction as a dominant source of uncertainty. Improved low-energy measurements near the 65 keV resonance, including direct measurements with windowless gas targets or indirect studies using the Trojan Horse Method or asymptotic normalization coefficients, would help to resolve current discrepancies between experiments and reduce

model uncertainty. New data constraining the resonance strength and interference terms at temperatures between 0.02 and 0.07 GK would be particularly valuable for simulations of CBP and AGB nucleosynthesis.

Progress in these areas—both in nuclear data and in physically motivated stellar models—will be essential to determine whether the isotopic patterns observed in presolar grains primarily reflect the details of stellar mixing or residual uncertainties in nuclear reaction rates.

Bibliography

Amari, S., Hoppe, P., Zinner, E., and Lewis, R. S. (1995). Trace-element concentrations in single circumstellar silicon carbide grains from the Murchison meteorite. *Meteoritics*, 30(6):679–693.

Angulo, C., Arnould, M., Rayet, M., Descouvemont, P., Baye, D., Leclercq-Willain, C., Coc, A., Barhoumi, S., Aguer, P., Rolfs, C., Kunz, R., Hammer, J. W., Mayer, A., Paradellis, T., Kossionides, S., Chronidou, C., Spyrou, K., Degl'Innocenti, S., Fiorentini, G., Ricci, B., Zavatarelli, S., Providencia, C., Wolters, H., Soares, J., Grama, C., Rahighi, J., Shotter, A., and Lamehi Rachti, M. (1999). A compilation of charged-particle induced thermonuclear reaction rates. *Nuclear Physics A*, 656(1):3.

Arnett, W. D., Meakin, C., Viallet, M., Campbell, S. W., Lattanzio, J. C., and Mocák, M. (2015). Beyond Mixing-Length Theory: A Step Toward 321D. *The Astrophysical Journal*, 809(1):30.

Asplund, M., Grevesse, N., Sauval, A. J., and Scott, P. (2009). The Chemical Composition of the Sun. *Annual Review of Astronomy and Astrophysics*, 47:481.

Bethe, H. A. (1939). Energy Production in Stars. *Physical Review*, 55(5):434–456.

Bloecker, T. (1995). Stellar evolution of low- and intermediate-mass stars. II. Post-AGB evolution. *Astronomy and Astrophysics*, 299:755.

Blouin, S., Woodward, P. R., Denissenkov, P. A., Pathak, P., and Herwig, F. (2025). Wave-driven mixing enhanced by rotation in red giant branch stars. *Nature Astronomy*. Manuscript submitted for publication.

Boothroyd, A. I. and Sackmann, I.-J. (1999). The CNO Isotopes: Deep Circulation in Red Giants and First and Second Dredge-up. *The Astrophysical Journal*, 510(1):232.

Bruno, C. G., Aliotta, M., Descouvemont, P., Best, A., Davinson, T., Bemmerer, D., Boeltzig, A., Broggini, C., Caciolli, A., Cavanna, F., Chillery, T., Ciani, G. F., Corvisiero, P., Depalo, R., Di Leva, A., Elekes, Z., Ferraro, F., Formicola, A., Fülöp, Z., Gervino, G., Guglielmetti, A., Gustavino, C., Gyürky, G., Imbriani, G., Junker, M., Lugaro, M., Marigo, P., Menegazzo, R., Mossa, V., Pantaleo, F. R., Piatti, D., Prati, P., Stöckel, K., Straniero, O., Strieder, F., Szücs, T., Takács, M. P., and Trezzi, D. (2019). Improved astrophysical rate for the 18O(p,α)15N reaction by underground measurements. *Physics letters. B*, 790:237.

Bruno, C. G., Scott, D. A., Aliotta, M., Formicola, A., Best, A., Boeltzig, A., Bemmerer, D., Broggini, C., Caciolli, A., Cavanna, F., Ciani, G. F., Corvisiero, P., Davinson, T., Depalo, R., Di Leva, A., Elekes, Z., Ferraro, F., Fülöp, Zs., Gervino, G., Guglielmetti, A., Gustavino, C., Gyürky, Gy., Imbriani, G., Junker, M., Menegazzo, R., Mossa, V., Pantaleo, F. R., Piatti, D., Prati, P., Somorjai, E., Straniero, O., Strieder, F., Szücs, T., Takács, M. P., and Trezzi, D. (2016). Improved Direct Measurement of the 64.5 keV Resonance Strength in the $^{17}O(p,\alpha)^{14}N$ Reaction at LUNA. *Physical Review Letters*, 117(14):142502.

Burbidge, E. M., Burbidge, G. R., Fowler, W. A., and Hoyle, F. (1957). Synthesis of the Elements in Stars. *Reviews of Modern Physics*, 29:547–650.

Charbonnel, C. and Balachandran, S. (2000). The nature of the lithium rich giants. mixing episodes on the rgb and early-agb. *Astronomy and Astrophysics*.

Charbonnel, C. and Zahn, J.-P. (2007). Thermohaline mixing: A physical mechanism governing the photospheric composition of low-mass giants. *Astronomy & Astrophysics*, 467(1):L15.

Christensen, N. S., Jensen, F., Besenbacher, F., and Stensgaard, I. (1990). Absolute calibration of the 18O(p, α)15N nuclear reaction. *Nuclear Instruments and Methods in Physics Research Section B: Beam Interactions with Materials and Atoms*, 51(2):97.

Cognata, M. L., Spitaleri, C., and Mukhamedzhanov, A. M. (2010). Effect OF High-Energy Resonances on the 18O(p, α)15N Reaction Rate at AGB and Post-AGB Relevant Temperatures. *The Astrophysical Journal*, 723(2):1512.

Cowan, J. J. and Rose, W. K. (1977). Production of 14C and neutrons in red giants. *The Astrophysical Journal*, 212:149–158.

Cristini, A., Meakin, C., Hirschi, R., Arnett, D., Georgy, C., Viallet, M., and Walkington, I. (2017). 3D hydrodynamic simulations of carbon burning in massive stars. *Monthly Notices of the Royal Astronomical Society*, 471(1):279.

Cyburt, R. H., Amthor, A. M., Ferguson, R., Meisel, Z., Smith, K., Warren, S., Heger, A., Hoffman, R. D., Rauscher, T., Sakharuk, A., Schatz, H., Thielemann, F. K., and Wiescher, M. (2010). The JINA Reaclibe Database: Its Recent Updates and Impact on Type-I X-Ray Bursts. *The Astrophysical Journal Supplement Series*, 189(1):240.

Denissenkov, P. A., Blouin, S., Herwig, F., Stott, J., and Woodward, P. R. (2024). Enhanced extra mixing in low-mass stars approaching the RGB tip and the problem of Li-rich red-clump stars. *Monthly Notices of the Royal Astronomical Society*, 535(2):1243–1257.

Denissenkov, P. A., Pinsonneault, M., and MacGregor, K. B. (2009). Magneto-Thermohaline Mixing in Red Giants. *The Astrophysical Journal*, 696(2):1823.

Denissenkov, P. A., VandenBerg, D. A., Kopacki, G., and Ferguson, J. W. (2017). Constraints on the Distance Moduli, Helium, and Metal Abundances, and Ages of Globular Clusters from Their RR Lyrae and Non-variable Horizontal Branch Stars. II. Multiple Stellar Populations in 47 Tuc, M3, and M13. *The Astrophysical Journal*, 849:159.

Descouvemont, P. and Baye, D. (2010). The R-matrix theory. *Reports on Progress in Physics*, 73(3):036301.

Gesuè, R. M., Ciani, G. F., Piatti, D., Boeltzig, A., Rapagnani, D., Aliotta, M., Ananna, C., Barbieri, L., Barile, F., Bemmerer, D., Best, A., Broggini, C., Bruno, C. G., Caciolli, A., Campostrini, M., Casaburo, F., Cavanna, F., Colombetti, P., Compagnucci, A., Corvisiero, P., Csedreki, L., Davinson, T., De Gregorio, G. M., Dell'Aquila, D., Depalo, R., Di Leva, A., Elekes, Z., Ferraro, F., Formicola, A., Fülöp, Zs., Gervino, G., Guglielmetti, A., Gustavino, C., Gyürky, Gy., Imbriani, G., Junker, M., Lugaro, M., Marigo, P., Marsh, J., Masha, E., Menegazzo, R., Mercogliano, D., Paticchio, V., Perrino, R., Prati, P., Rigato, V., Robb, D., Schiavulli, L., Sidhu, R. S., Skowronski, J., Straniero, O., Szücs, T., and Zavatarelli, S. (2024). First Direct Measurement of the 64.5 keV Resonance Strength in the $^{17}\mathrm{O}(p,\gamma)^{18}\mathrm{F}$ Reaction. *Physical Review Letters*, 133(5):052701.

Gilroy, K. K. (1989). Carbon Isotope Ratios and Lithium Abundances in Open Cluster Giants. *The Astrophysical Journal*, 347:835.

Gilroy, K. K. and Brown, J. A. (1991). Carbon Isotope Ratios along the Giant Branch of M67. *The Astrophysical Journal*, 371:578.

Harris, M. J. and Lambert, D. L. (1984). Oxygen isotopic abundances in the atmospheres of seven red giant stars. *The Astrophysical Journal*, 285:674–682.

Herwig, F. (2000). The evolution of AGB stars with convective overshoot. *Astronomy & Astrophysics*, 360:952.

Herwig, F. (2013). Evolution of Solar and Intermediate-Mass Stars. In *Planets, Stars and Stellar Systems. Volume 4: Stellar Structure and Evolution*, volume 4, page 397.

Hinkle, K. H., Lebzelter, T., and Straniero, O. (2016). Carbon and Oxygen Isotopic Ratios for Nearby Miras. *The Astrophysical Journal*, 825:38.

Hoyle, F. (1954). On Nuclear Reactions Occuring in Very Hot STARS.I. the Synthesis of Elements from Carbon to Nickel. *The Astrophysical Journal Supplement Series*, 1:121.

Hynes, K. M. and Gyngard, F. (2009). The Presolar Grain Database: http://presolar.wustl.edu/~pgd. In *40th Annual Lunar and Planetary Science Conference*, page 1198.

Iliadis, C., Longland, R., Champagne, A. E., Coc, A., and Fitzgerald, R. (2010). Charged-particle thermonuclear reaction rates: II. Tables and graphs of reaction rates and probability density functions. *Nuclear Physics A*, 841(1):31.

Iliadis, C., Palanivelrajan, V., and De Souza, R. S. (2022). Bayesian estimation of the S factor and thermonuclear reaction rate for O 16 (p , γ) F 17. *Physical Review C*, 106(5):055802.

Kippenhahn, R., Weigert, A., and Weiss, A. (2012). *Stellar Structure and Evolution*. Astronomy and Astrophysics Library. Springer, Berlin, Heidelberg.

Kumar, Y. B., Reddy, B. E., Campbell, S. W., Maben, S., Zhao, G., and Ting, Y.-S. (2020). Discovery of ubiquitous lithium production in low-mass stars. *Nature Astronomy*, 4(11):1059–1063.

Kunz, R., Fey, M., Jaeger, M., Mayer, A., Hammer, J. W., Staudt, G., Harissopulos, S., and Paradellis, T. (2002). Astrophysical Reaction Rate of 12C(α, γ)16O. *The Astrophysical Journal*, 567(1):643.

La Cognata, M., Fisichella, M., Pietro Di, A., Figuera, P., Goldberg, V. Z., Cherubini, S., Garcia, J. P. F., Gulino, M., Lamia, L., Lattuada, D., Lattuada, M., Pizzone, R. G., Rapisarda, G. G., Romano, S., Spartá, R., Spitaleri, C., Torresi, D., Tumino, A., and Zadro, M. (2019). Observation of 15N+α resonant structures in 19F using the thick target in inverse kinematics scattering method. *Physical Review C*, 99:034301.

LeBlanc, F. (2010). *An Introduction to Stellar Astrophysics*. Wiley Series in Astronomy and Astrophysics. John Wiley & Sons, Ltd., Chichester, UK.

Lebzelter, T., Hinkle, K. H., Straniero, O., Lambert, D. L., Pilachowski, C. A., and Nault, K. A. (2019). Carbon and Oxygen Isotopic Ratios. II. Semiregular Variable M Giants. *The Astrophysical Journal*, 886(2):117.

Ledoux, P. (1947). Stellar Models with Convection and with Discontinuity of the Mean Molecular Weight. *The Astrophysical Journal*, 105:305.

Li, Y.-Y., Hu, J., Ru, L.-H., Tian, N., and Lv, J.-F. (2024). Revised Reaction Rate for the Astrophysical Reaction 18 O(p, α) 15 N via a Global R-matrix Analysis. *The Astrophysical Journal*, 973(2):93.

Liu, N. (2024). Presolar grains. In Holland, H. D. and Turekian, K. K., editors, *Treatise on Geochemistry*. Elsevier, Oxford, 3rd edition. Chapter in revised edition.

Liu, N., Dauphas, N., Cristallo, S., Palmerini, S., and Busso, M. (2022). Oxygen and aluminum-magnesium isotopic systematics of presolar nanospinel grains from CI chondrite Orgueil. *Geochimica et Cosmochimica Acta*, 319:296.

Lodders, K. and Amari, S. (2005). Presolar grains from meteorites: Remnants from the early times of the solar system. *Geochemistry*, 65(2):93.

Lorenz-Wirzba, H., Schmalbrock, P., Trautvetter, H. P., Wiescher, M., Rolfs, C., and Rodney, W. S. (1979). The 18O(p, α)15N Reaction at Stellar Energies. *Nuclear Physics A*, 313:346.

Lugaro, M., Karakas, A. I., Bruno, C. G., Aliotta, M., Nittler, L. R., Bemmerer, D., Best, A., Boeltzig, A., Broggini, C., Caciolli, A., Cavanna, F., Ciani, G. F., Corvisiero, P., Davinson, T., Depalo, R., di Leva, A., Elekes, Z., Ferraro, F., Formicola, A., Fülöp, Zs., Gervino, G., Guglielmetti, A., Gustavino, C., Gyürky, Gy., Imbriani, G., Junker, M., Menegazzo, R., Mossa, V., Pantaleo, F. R., Piatti, D., Prati, P., Scott, D. A., Straniero, O., Strieder,

F., Szücs, T., Takács, M. P., and Trezzi, D. (2017). Origin of meteoritic stardust unveiled by a revised proton-capture rate of 17O. *Nature Astronomy*, 1:0027.

Mak, H. B., Evans, H. C., Ewan, G. T., and Macarthur, J. D. (1978). The 18O(p, α)15N cross section at low energies. *Nuclear Physics A*, 304(1):210.

Meakin, C. A. and Arnett, D. (2007). Turbulent Convection in Stellar Interiors. I. Hydrodynamic Simulation. *The Astrophysical Journal*, 667(1):448.

National Nuclear Data Center (2023). Nudat 3.0: Nuclear structure and decay data. https://www.nndc.bnl.gov/nudat3/. Brookhaven National Laboratory.

Nittler, L. R. (1997). Presolar oxide grains in meteorites. In *Astrophysical Implications of the Laboratory Study of Presolar Materials*, volume 402, pages 59–82. AIP.

Nittler, L. R., Alexander, C. M. O., Gallino, R., Hoppe, P., Nguyen, A. N., Stadermann, F. J., and Zinner, E. K. (2008). Aluminum-, Calcium- and Titanium-rich Oxide Stardust in Ordinary Chondrite Meteorites. *The Astrophysical Journal*, 682(2):1450.

Nittler, L. R. and Ciesla, F. (2016). Astrophysics with Extraterrestrial Materials. *Annual Review of Astronomy and Astrophysics*, 54:53–93.

Nollett, K. M., Busso, M., and Wasserburg, G. J. (2003). Cool Bottom Processes on the Thermally Pulsing Asymptotic Giant Branch and the Isotopic Composition of Circumstellar Dust Grains. *The Astrophysical Journal*, 582:1036.

Palmerini, S., Cristallo, S., Piersanti, L., Vescovi, D., and Busso, M. (2021). Group II Oxide Grains: How Massive Are Their AGB Star Progenitors? *Universe*, 7(6):175.

Palmerini, S., La Cognata, M., Cristallo, S., and Busso, M. (2011). Deep Mixing in Evolved Stars. I. The Effect of Reaction Rate Revisions From C To Al. *The Astrophysical Journal*, 729(1):3.

Paxton, B., Bildsten, L., Dotter, A., Herwig, F., Lesaffre, P., and Timmes, F. (2010). Modules for Experiments in Stellar Astrophysics (MESA). *The Astrophysical Journal Supplement Series*, 192(1):3.

Paxton, B., Cantiello, M., Arras, P., Bildsten, L., Brown, E. F., Dotter, A., Mankovich, C., Montgomery, M. H., Stello, D., Timmes, F. X., and Townsend, R. (2013). Modules for Experiments in Stellar Astrophysics (MESA): Planets, Oscillations, Rotation, and Massive Stars. *The Astrophysical Journal Supplement Series*, 208(1):4.

Pignatari, M., Herwig, F., Hirschi, R., Bennett, M., Rockefeller, G., Fryer, C., Timmes, F. X., Ritter, C., Heger, A., Jones, S., Battino, U., Dotter, A., Trappitsch, R., Diehl, S., Frischknecht, U., Hungerford, A., Magkotsios, G., Travaglio, C., and Young, P. (2016). NuGrid Stellar Data Set. I. Stellar Yields from H to BI for Stars with Metalicities Z = 0.02 and Z = 0.01. *The Astrophysical Journal Supplement Series*, 225(2):24.

Prantzos, N., Aubert, O., and Audouze, J. (1996). Evolution of the carbon and oxygen isotopes in the Galaxy. *Astronomy and Astrophysics*, 309:760–774.

Rapagnani, D., Straniero, O., Imbriani, G., Aliotta, M., Ananna, C., Barile, F., Barbieri, L., Bemmerer, D., Best, A., Boeltzig, A., Broggini, C., Bruno, C. G., Caciolli, A., Campostrini, M., Casaburo, F., Cavanna, F., Ciani, G. F., Colombetti, P., Compagnucci, A., Corvisiero, P., Csedreki, L., Davinson, T., Depalo, R., Di Leva, A., Elekes, Z., Ferraro, F., Formicola, A., Fülöp, Zs., Gervino, G., Gesuè, R. M., Gyürky, Gy., Guglielmetti, A., Gustavino, C., Junker, M., Lugaro, M., Marigo, P., Marsh, J., Masha, E., Menegazzo, R., Mercogliano, D., Paticchio, V., Piatti, D., Prati, P., Rigato, V., Robb, D., Sidhu, R. S., Skowronski, J., Szücs, T., and Zavatarelli, S. (2025). Revision of the CNO cycle: Rate of ^{17}O Destruction in Stars. *Physical Review C*, 111(2):025805.

Reimers, D. (1977). On the absolute scale of mass-loss in red giants. I. Circumstellar absorption lines in the spectrum of the visual companion of alpha 1Her. *Astronomy and Astrophysics*, 61:217.

Ritter, C., Herwig, F., Jones, S., Pignatari, M., Fryer, C., and Hirschi, R. (2018). NuGrid stellar data set - II. Stellar yields from H to Bi for stellar models with MZAMS = 1-25 M$\odot$ and Z = 0.0001-0.02. *Monthly Notices of the Royal Astronomical Society*, 480:538.

Schröder, K. P. and Cuntz, M. (2007). A critical test of empirical mass loss formulas applied to individual giants and supergiants. *Astronomy and Astrophysics*, 465:593.

Sergi, M. L., Guardo, G. L., La Cognata, M., Gulino, M., Mrazek, J., Palmerini, S., Spitaleri, C., and Wiescher, M. (2020). Indirect Measurements of n- and p-Induced Reactions of Astrophysical Interest on Oxygen Isotopes. *Frontiers in Astronomy and Space Sciences*, 7.

Sergi, M. L., Spitaleri, C., La Cognata, M., Lamia, L., Pizzone, R. G., Rapisarda, G. G., Tang, X. D., Bucher, B., Couder, M., Davies, P., deBoer, R., Fang, X., Lamm, L., Ma, C., Notani, M., O'Brien, S., Roberson, D., Tan, W., Wiescher, M., Irgaziev, B.,

Mukhamedzhanov, A., Mrazek, J., and Kroha, V. (2015). Improvement of the high-accuracy O 17 (p , α) N 14 reaction-rate measurement via the Trojan Horse method for application to O 17 nucleosynthesis. *Physical Review C*, 91(6):065803.

Shaviv, G. and Salpeter, E. E. (1973). Convective Overshooting in Stellar Interior Models. *The Astrophysical Journal*, 184:191–200.

Straniero, O., Gallino, R., and Cristallo, S. (2006). S process in low-mass asymptotic giant branch stars. *Nuclear Physics A*, 777:311.

Tilley, D. R., Weller, H. R., and Cheves, C. M. (1993). Energy levels of light nuclei $A =$ 16–17. *Nuclear Physics A*, 564(1):1.

Tuli, J. K. (1996). Evaluated nuclear structure data file (ensdf). *Nuclear Instruments and Methods in Physics Research A*, 369:506–510.

VandenBerg, D. A., Denissenkov, P. A., and Catelan, M. (2016). Constraints on the Distance Moduli, Helium and Metal Abundances, and Ages of Globular Clusters from their RR Lyrae and Non-Variable Horizontal-Branch Stars. I. M3, M15, AND M92. *The Astrophysical Journal*, 827(1):2.

Vassiliadis, E. and Wood, P. R. (1993). Evolution of Low- and Intermediate-Mass Stars to the End of the Asymptotic Giant Branch with Mass Loss. *The Astrophysical Journal*, 413:641.

Zinner, E. (2014). Presolar Grains. In Holland, H. D. and Turekian, K. K., editors, *Treatise on Geochemistry (Second Edition)*, pages 181–213. Elsevier, Oxford.